

# **Constraining Dark Matter Through the Study of Merging Galaxy Clusters**

By

WILLIAM ANTHONY DAWSON

B.S. Maritime Systems Engineering (Texas A&M University, Galveston) 2002

M.S. Physics (University of California, Davis) 2008

## **DISSERTATION**

Submitted in partial satisfaction of the requirements for the degree of

**DOCTOR OF PHILOSOPHY**

in

**PHYSICS**

in the

**OFFICE OF GRADUATE STUDIES**

of the

**UNIVERSITY OF CALIFORNIA**

**DAVIS**

Approved:

Professor David M. Wittman (Chair)

---

Professor J. Anthony Tyson

---

Professor Maruša Bradač

---

Committee in Charge

2013

© William Anthony Dawson, 2013. All rights reserved.

For my wife Kerri.

# Contents

<b>Table of Contents</b>	<b>iv</b>
<b>List of Figures</b>	<b>vii</b>
<b>List of Tables</b>	<b>ix</b>
<b>Abstract</b>	<b>x</b>
<b>Acknowledgments</b>	<b>xiii</b>
<b>1 Introduction</b>	<b>1</b>
1.1 Composition of the Universe . . . . .	1
1.2 Dark Matter . . . . .	2
1.2.1 Historical Review . . . . .	2
1.2.2 General Properties of Dark Matter . . . . .	3
1.3 Motivation for Studying Self-interacting Dark Matter and Existing Constraints	4
1.3.1 Early Motivation . . . . .	4
1.3.2 Early SIDM Constraints . . . . .	5
1.3.3 Recent Motivation . . . . .	7
1.4 Probes of SIDM . . . . .	8
1.5 Merging Galaxy Clusters as Probes of Self-Interacting Dark Matter . . . . .	9
1.5.1 Merging Galaxy Clusters . . . . .	9
1.5.2 Constraining Self-Interacting Dark Matter with Merging Galaxy Clusters	11
1.5.3 Advantages of Merging Clusters Over other Probes of Self-interacting Dark Matter . . . . .	18
1.6 Work Presented in this Dissertation . . . . .	18
<b>2 Musket Ball Cluster: Observed Properties</b>	<b>19</b>
2.1 Introduction . . . . .	19
2.2 Photometric . . . . .	20
2.3 Spectroscopic . . . . .	23
2.4 Weak Lensing . . . . .	24
2.5 Sunyaev–Zel’dovich Effect . . . . .	28
2.6 X-ray . . . . .	28
2.7 Radio . . . . .	32
2.8 Cluster Merger Scenario . . . . .	33

2.9	Discussion . . . . .	35
2.10	Conclusions . . . . .	36
<b>3</b>	<b>Dynamics of Merging Clusters</b>	<b>37</b>
3.1	Introduction . . . . .	38
3.2	Method . . . . .	43
3.2.1	Model . . . . .	44
3.2.2	Monte Carlo Analysis . . . . .	46
3.2.3	Comparison with Hydrodynamic Simulations . . . . .	49
3.3	Bullet Cluster Dynamics . . . . .	51
3.3.1	Bullet Cluster Observed System Properties . . . . .	52
3.3.2	Bullet Cluster System Dynamics Results . . . . .	52
3.4	Musket Ball Cluster Dynamics . . . . .	60
3.4.1	Musket Ball Observed System Properties . . . . .	61
3.4.2	Musket Ball System Dynamics Results . . . . .	64
3.5	Summary and Discussion . . . . .	68
3.5.1	Suggested Uses of Method . . . . .	69
3.5.2	Extensions to the Method . . . . .	70
<b>4</b>	<b>Musket Ball Cluster: Dark Matter Implications</b>	<b>73</b>
4.1	Introduction . . . . .	73
4.2	Location Estimation . . . . .	73
4.2.1	Galaxies . . . . .	74
4.2.2	Gas . . . . .	74
4.2.3	Weak Lensing . . . . .	74
4.3	Gas–Weak Lensing Offset . . . . .	74
4.4	Galaxy–Weak Lensing Offset . . . . .	75
4.5	Discussion . . . . .	77
4.5.1	Subsection title . . . . .	77
4.6	Conclusions . . . . .	77
<b>5</b>	<b>Perspective: Summary &amp; Discussion</b>	<b>79</b>
5.1	Dissertation Summary . . . . .	79
5.2	Discussion on the Path Forward . . . . .	79
5.2.1	Bridging the Gap Between Observations and Simulations . . . . .	79
5.2.2	Theoretical model of the behavior of SIDM during mergers . . . . .	80
5.2.3	Simulating mergers with SIDM . . . . .	81
5.2.4	Find and study more dissociative mergers . . . . .	81
5.3	Current Progress along this Path . . . . .	82
<b>A</b>	<b>Dynamics of Merging Clusters Appendix</b>	<b>83</b>
A.1	Potential Energy of Two Truncated NFW Halos . . . . .	83
A.1.1	Truncated NFW Gravitational Potential . . . . .	84
A.1.2	Mass Elements of a Truncated NFW Halo . . . . .	85
A.2	Musket Ball Cluster Redshift Catalog . . . . .	86

A.3	Bullet Cluster Result Plots . . . . .	88
A.4	Musket Ball Cluster Result Plots . . . . .	96

# List of Figures

1.1	A basic time series leading to a dissociative galaxy cluster merger. . . . .	12
1.2	The four means of constraining $\sigma_{\text{SIDM}}$ with merging clusters. . . . .	13
2.1	Merging cluster DLSCL J0916.2+2951 and its three matter components. . . .	21
2.2	Color image of DLSCL J0916.2+2951 and its galaxy number density with a histogram of the spectroscopic redshifts in the area. . . . .	22
2.3	Musket Ball Cluster color-magnitude diagram based on HST photometry, along with galaxy location based on DLS photometric redshifts. . . . .	26
2.4	Comparison of the Musket Ball Cluster, HUDF and GOODS North & South source galaxy densities. . . . .	27
2.5	Comparison of the Subaru $i'$ -band ground-based and HST space-based WL mass signal-to-noise maps of DLSCL J0916.2+2951 with the X-ray distribution and galaxy number density. . . . .	29
2.6	DLS optical image with SZE and galaxy number density maps. . . . .	30
2.7	Radio survey of the Musket Ball Cluster and surrounding area. . . . .	34
3.1	Parameters involved in a generic two-halo merger configuration. . . . .	41
3.2	Comparison of the analytic model results with hydrodynamic simulation results of the Bullet Cluster. . . . .	51
3.3	The posterior of the Bullet Cluster's time-since-collision and three-dimensional collision velocity parameters. . . . .	55
3.4	The posterior of the Bullet Cluster's $TSC_0$ and $v_{3D}(t_{\text{col}})$ parameters after application of an additional temporal prior based on X-ray observations of the Bullet Cluster. . . . .	59
3.5	Weak lensing mass PDF's of the Musket Ball subclusters (Dawson et al., 2012). . . . .	61
3.6	Relative radial subcluster velocity PDF's inferred from spectroscopic redshifts the Musket Ball Cluster galaxies (Dawson et al., 2012). . . . .	62
3.7	Projected separation PDF of the Musket Ball subcluster galaxy density centroids (Dawson et al., 2012). . . . .	63
3.8	The posterior of the Musket Ball Cluster's $TSC_0$ and $v_{3D}(t_{\text{col}})$ parameters. . . . .	65
3.9	Comparison of the Musket Ball Cluster's and Bullet Cluster's time-since-collision. . . . .	66
4.1	Comparison of the Subaru $i'$ -band ground-based and HST space-based WL mass signal-to-noise maps of DLSCL J0916.2+2951 with the X-ray distribution and galaxy number density. . . . .	76

4.2	Musket Ball Cluster galaxy-weak lensing offset.	78
A.1	Dynamics results array configuration.	89
A.2	Bullet Cluster marginalized <i>Input vs. Input</i> parameters result plots.	90
A.3	Bullet Cluster marginalized <i>Input vs. Geometry</i> parameters result plots.	91
A.4	Bullet Cluster marginalized <i>Input vs. Velocity &amp; Time</i> parameters result plots.	92
A.5	Bullet Cluster marginalized <i>Geometry vs. Geometry</i> parameters result plots.	93
A.6	Bullet Cluster marginalized <i>Geometry vs. Velocity &amp; Time</i> parameters result plots.	94
A.7	Bullet Cluster marginalized <i>Velocity &amp; Time vs. Velocity &amp; Time</i> parameters result plots.	95
A.8	Musket Ball Cluster marginalized <i>Input vs. Input</i> parameters result plots.	97
A.9	Musket Ball Cluster marginalized <i>Input vs. Geometry</i> parameters result plots.	98
A.10	Musket Ball Cluster marginalized <i>Input vs. Velocity &amp; Time</i> parameters result plots.	99
A.11	Musket Ball Cluster marginalized <i>Geometry vs. Geometry</i> parameters result plots.	100
A.12	Musket Ball Cluster marginalized <i>Geometry vs. Velocity &amp; Time</i> parameters result plots.	101
A.13	Musket Ball Cluster marginalized <i>Velocity &amp; Time vs. Velocity &amp; Time</i> parameters result plots.	102

# List of Tables

2.1	Observed subcluster and X-ray concentration properties . . . . .	24
3.1	Bullet Cluster parameter input . . . . .	53
3.2	Bullet Cluster parameter estimates . . . . .	57
3.3	Musket Ball Cluster parameter estimates . . . . .	67
A.1	Musket Ball Cluster Redshift Catalog . . . . .	87

# Abstract

**Context:** The majority ( $\sim 85\%$ ) of the matter in the universe is composed of dark matter, a mysterious particle that does not interact via the electromagnetic force yet does interact with all other matter via the gravitational force. Many direct detection experiments have been devoted to finding interactions of dark matter with baryonic matter via the weak force. To date only tentative and highly controversial evidence for such interactions has been found. While such direct detection experiments have ruled out the possibility that dark matter interacts with baryonic matter via a strong scale force, it is still possible that dark matter interacts with itself via a strong scale force and has a self-scattering cross-section of  $\sim 0.5 \text{ cm}^2/\text{g}^{-1}$ . In fact such a strong scale scattering force could resolve several outstanding astronomical mysteries: a discrepancy between the cuspy density profiles seen in  $\Lambda\text{CDM}$  simulations and the cored density profiles observed in low surface brightness galaxies, dwarf spheroidal galaxies, and galaxy clusters, as well as the discrepancy between the significant number of massive Milky Way dwarf spheroidal halos predicted by  $\Lambda\text{CDM}$  and the dearth of observed Milky Way dwarf spheroidal halos.

**Need:** While such probes are in conflict with  $\Lambda\text{CDM}$  and suggest that dark matter may self-scatter, each suffers from a *baryonic degeneracy*, where the observations might be explained by various baryonic processes (e.g., AGN or supernova feedback, XXX etc.) rather than self-interacting dark matter (SIDM). In fact the important scales of these observations often coincide with baryonic scales (e.g., the core size in clusters is approximately the size of the brightest cluster galaxy). What is needed is a probe of SIDM where the expected effect cannot be replicated by the same processes responsible for the baryonic degeneracy in the aforementioned probes. Merging galaxy clusters are such a probe. During the merging process the effectively collisionless galaxies ( $\sim 2\%$  of the cluster mass) become dissociated from the collisional intracluster gas ( $\sim 15\%$  of the cluster mass). The gas strongly interacts during the merger and becomes pancaked at the point of collision. If dark matter lags behind the effectively collisionless galaxies then this is clear evidence that dark matter self-interacts.

The expected galaxy-dark matter offset is typically  $\gtrsim 25$  kpc (for cross-sections that would explain the other aforementioned mysteries), this is considerably larger than the scales of that are plagued by the baryonic degeneracies.

**Task:** To test whether dark matter self-interacts we have carried out a comprehensive survey of the dissociative merging galaxy cluster DLSCL J0916.2+2951 (also known as the Musket Ball Cluster). This survey includes photometric and spectroscopic observations to quantify the position and velocity of the cluster galaxies, weak gravitational lensing observations to map and weigh the mass (i.e. dark matter) of the cluster, Sunyaev-Zel'dovich effect and X-ray observations to map and quantify the intracluster gas, and finally radio observations to search for associated radio relics that could help constrain the properties of the merger. Using this information in conjunction with a Monte Carlo analysis model I quantify the dynamic properties of the merger, necessary to properly interpret constraints on the SIDM cross-section. I compare the locations of the galaxies, dark matter and gas to constrain the SIDM cross-section. This dissertation presents this work.

**Findings:** We find that the Musket Ball is a modest merger with total mass of  $4.8^{+3.2}_{-1.5} \times 10^{14} M_{\odot}$ . However, my dynamic analysis shows that the Musket Ball is being observed  $1.1^{+1.3}_{-0.4}$  Gyr after first pass through and is much further progressed in its merger process than previously identified dissociative mergers ( $3.4^{+3.8}_{-1.4}$  times further progressed than the Bullet Cluster). By observing that the dark matter is significantly offset from the gas we are able to place an upper limit on the dark matter cross-section of  $\sigma_{\text{SIDM}} m_{\text{DM}}^{-1} < 8 \text{ cm}^2 \text{ g}^{-1}$ . We find an offset of XXX between the galaxies and dark matter in the southern subcluster.

**Conclusion:** This offset suggests that dark matter self-interacts with XXX% confidence, and appears to be consistent with existing SIDM constraints. While this offset is significant, it is not significant enough to claim that dark matter self-interacts.

**Perspectives:** The galaxy-dark matter offset measurement is a Poisson noise dominated measurement. Thus measuring this offset in other dissociative mergers holds the promise of reducing our uncertainty and enabling us to: 1) state confidently that dark matter self-

interacts via a new dark sector force, or 2) constrain the dark matter cross-section to such a degree that SIDM cannot explain the aforementioned mysteries. To this end we have established the merging cluster collaboration to observe and simulate an ensemble of dissociative merging cluster. We are currently in the process of analyzing six dissociative mergers with existing data, and carrying out multi-wavelength observations of a new sample of 15 radio relic identified dissociative mergers.

## Acknowledgments

Add text here

# Chapter 1

## An Introduction to Self-interacting Dark Matter and Merging Galaxy Clusters

### 1.1 Composition of the Universe

Over the past one-hundred years there has been a revolution in our understanding of the universe. From believing that the Milky Way was the extent of the Universe, that the age of Universe was infinite, and that the Universe was composed entirely of atomic matter and photons (cite Hoyle 1950 book), to now having evidence that the Universe at least extends as far as light can travel in the finite age of the universe ( $13.817 \pm 0.048$ ; Planck Collaboration et al., 2013), and is dominated by mysterious dark energy and dark matter rather than atomic matter. Our studies of the universe have improved to such a degree that we are now able to quantify the composition of the universe to percent level accuracy. We find that atomic matter (which is dominated by baryonic particles, i.e. particles of the atomic nuclei) only accounts for  $\sim 5\%$  of the universe's total matter-energy budget. The universe appears to largely be composed of dark matter (DM;  $\sim 26\%$ ) and dark energy ( $\sim 69\%$ ; see Planck

Collaboration et al., 2013, for more accurate values). Very little is known about each of these components. In very basic terms, dark energy appears to be a particle or field that acts to make the universe expand, while DM appears to be a particle that currently has only been observed to interact via the gravitational force (also known as cold dark matter; CDM). This has come to be known as the concordance cosmological model ( $\Lambda$ CDM). This dissertation will focus on our efforts to further our understanding of DM, in particular to ascertain whether DM interacts with itself other than through the gravitational force or if it really is just CDM.

## 1.2 Dark Matter

### 1.2.1 Historical Review

“Dunkle (kalte) Materie” (or “Dark (cold) Matter”) was first proposed by Zwicky (1933). Zwicky had measured the velocities of the galaxies in the Coma galaxy cluster, via their spectroscopic redshifts, and found that given the large velocities the galaxies should not be gravitationally bound if galaxies/stars make up the entirety of the cluster mass. According to his calculations the total CDM mass must be about 400 times that of the mass of the visible galaxies. As van den Bergh (1999) notes in his review article, had Zwicky used the correct value for the Hubble constant (rather than the generally accepted value of his day,  $H_0=558\text{ km s}^{-1}\text{ Mpc}^{-1}$ ) he would have found that the CDM mass must be about 50 times that of the mass of the luminous matter, very close to the actual value of  $\sim 20$  (disregarding the mass of the X-ray emitting intracluster gas that was unbeknownst to astronomers at the time). Despite Zwicky’s pioneering and shocking findings, the idea of DM did not garner much attention until the work of Rubin & Ford (1970) on the rotation velocities of stars and gas in spiral galaxies (e.g. the Andromeda galaxy). This work was very much in the same vein as Zwicky’s work on the Coma galaxy cluster.

Zwicky also introduced another, completely independent, method of measuring the mass of galaxy clusters and coined the term “gravitational lens effect” (Zwicky, 1937). Zwicky

argued that if his mass estimates of the Coma cluster were correct, then the cluster should be massive enough to distort space-time to such a degree that as light from distant background galaxies travels through the gravitational potential well of the cluster the light will be deflected and the galaxy images will be distorted in a coherent fashion. Thus by measuring the distortion of galaxies behind a galaxy cluster one could estimate the mass of the galaxy cluster (see Chapter 2 of Courbin & Minniti, 2002, for an introduction to weak gravitational lensing). Tyson et al. (1990) were the first to successfully measure the gravitational lens effect of a galaxy cluster. They too found that a mass of the luminous matter alone was insufficient to produce the observed effect.

While the aforementioned work, and subsequent work, found that the amount of luminous mass in galaxies and clusters was not enough to gravitationally bind the stars and galaxies in those structures, there was still a debate about the solution to this problem. Two possible solutions dominated the debate: Zwicky was correct and there existed DM particles, or our understanding of the gravitational force needed to be modified (see Sanders & McGaugh, 2002, for a review). This debate remained one of the largest unsettled debates in physics and astronomy until Clowe et al. (2004) published their studies of the Bullet Cluster (1E 0657-558). The Bullet Cluster was the first discovered *dissociative merger* (see Figure 1.1 for a diagram of a dissociative merger). During the merging process the effectively collisionless galaxies become dissociated from the collisional intracluster gas, which strongly interacts during the merger and becomes pancaked at the point of collision. In total the cluster gas is about seven times as massive as the galaxies. When Clowe et al. (2004) measured where the total cluster mass was with the gravitational lens effect they found that the majority of the mass was located with the galaxies rather than with the gas. They then inferred that this was only possible if there was a DM particle that was nearly collisionless like the galaxies; modified gravity could not easily explain such an observation.

## 1.2.2 General Properties of Dark Matter

Peter (2012) provides a review of our current understanding of DM I recommend; I summarize a few relevant points here. In addition to the abundance of DM (see §1.1) there are a few things we know about the properties of DM. Most notably DM is electromagnetically neutral. DM does not interact with photons, either through absorption or emission. Baryons cannot make up a large portion of DM. This is known from observations of the cosmic microwave background, large-scale structure of the universe, and abundance of light elements created during big-bang nucleosynthesis. Nor can DM consist solely of light (sub-keV-mass) particles (e.g. neutrinos). Light particles move too fast in the early universe to form the initial density concentrations necessary to seed the cosmic structures observed at later times. DM is completely outside the realm our Standard Model of Particle Physics. Thus there is no reason to expect that it only interacts via the known forces. It is entirely possible that DM interacts with itself via some new dark gauge bosons. Such DM has been termed self-interacting dark matter (SIDM).

## 1.3 Motivation for Studying Self-interacting Dark Matter and Existing Constraints

### 1.3.1 Early Motivation

The earliest motivation for studying SIMD came from the *missing satellites problem* (see Bullock, 2010, for a thorough review). Moore et al. (1999) and Klypin et al. (1999) were the first to note that the number of Milky Way satellites predicted by  $\Lambda$ CDM simulations significantly exceeded the number of observed satellites. In an attempt to resolve this problem Spergel & Steinhardt (2000) revived a SIDM model with a large scattering cross-section but with negligible annihilation or dissipation<sup>1</sup>. They found that if the SIDM scattering cross-section

---

<sup>1</sup>Such a SIDM model was first proposed by Carlson et al. (1992) and Machacek (1994) to suppress small scale power of CDM dominated cosmologies. de Laix et al. (1995) found that while SIDM suppressed the

$(\sigma_{\text{SIDM}}/m_{\text{DM}})$  is between  $0.45\text{--}450 \text{ cm}^2 \text{ g}^{-1}$  then the expected number of Milky Way satellites could be brought inline with the number of observed satellites. More recently the Sloan Digital Sky Survey (SDSS) and Sloan Extension for Galactic Understanding and Exploration (SEGUE) have enabled the discovery of a number of new dwarf satellites (see Willman, 2010, for a review), effectively doubling the number of known satellites. This in combination with simulations that better quantified the selection function of these surveys has helped to reduce the tension between  $\Lambda$ CDM and the number of observed satellites. While the missing satellites problem is not resolved it is not nearly as significant as originally believed. On a final note, recent simulations (Rocha et al., 2013) show that for  $\sigma_{\text{SIDM}}/m_{\text{DM}} \sim 1 \text{ cm}^2 \text{ g}^{-1}$  the effects of DM halo evaporation are less than originally estimated by Spergel & Steinhardt (2000)'s analytic estimates, especially in the outer radii of parent DM halos where the majority of satellites reside.

### 1.3.2 Early SIDM Constraints

Following the revival of SIDM by Spergel & Steinhardt (2000), a number of researchers began to constrain  $\sigma_{\text{SIDM}} m_{\text{DM}}^{-1}$  through several independent observations, in what Peter et al. (2013) has termed the “Y2K-era constraints”. The Y2K-era constraints fall into five categories:

- (i) Those that compare the central density of simulated SIDM halos with those observed across a range of halo mass-scales from dwarf spheroids to galaxy clusters (Hogan & Dalcanton, 2000; Kochanek & White, 2000; Yoshida et al., 2000a,b; Davé et al., 2001; Dalcanton & Hogan, 2001; Meneghetti et al., 2001; Colín et al., 2002). Some finding that SIDM created central density cores (i.e. flattened density profile) that were too large and others finding that SIDM with large cross-sections actually exacerbates the formation of cusps (i.e. sharply peaked density profile).

- (ii) Those that compare the shape (i.e. spherical or elliptical) of simulated SIDM halos

---

small scale power spectrum in a desirable way it resulted in inconsistencies with the observed properties of galaxies. The de Laix et al. (1995) objections are no longer valid as they only applied to CDM dominated cosmologies, not  $\Lambda$ CDM cosmologies.

with the shapes of observed DM halos (Yoshida et al., 2000a; Davé et al., 2001; Miralda-Escudé, 2002). They found that as the SIDM cross-section is increase DM halos become more spherically symmetric and at a certain point elliptical halos, such as those observed in some galaxy clusters, can no longer be formed.

(iii) Those that compared the amount of substructure in simulated SIDM halos with the amount observed in galaxies and galaxy clusters (Hogan & Dalcanton, 2000; Yoshida et al., 2000a; Gnedin & Ostriker, 2001; Colín et al., 2002). As the SIDM cross-section increases subhalos begin to evaporate in their parent DM halo.

(iv) Those that estimated the formation of super massive black holes (SMBH) as a function of varying SIDM cross-section (Hennawi & Ostriker, 2002). As the SIDM cross-section is increased the initial seeds of SMBH's can form earlier and more efficiently. At some point the expected number and mass of SMBH's exceeds the observed number and mass.

(v) Those that compared and contrasted the observed behavior of DM with collisionless galaxies and collisional gas during the merging process of two galaxy clusters (Markevitch et al., 2004). This method will be the focus of this dissertation and is discussed in great detail in §1.5.2.

Of these early works four constrained the velocity independent  $\sigma_{\text{SIDM}} m_{\text{DM}}^{-1}$  to such a degree that it became astrophysically uninteresting. Gnedin & Ostriker (2001) obtained a constraint of  $\sigma_{\text{SIDM}} m_{\text{DM}}^{-1} \lesssim 0.3 \text{ cm}^2 \text{ g}^{-1}$  with their study of subhalo evaporation in galaxy clusters. Yoshida et al. (2000b) and Meneghetti et al. (2001) obtained a constraint of  $\sigma_{\text{SIDM}} m_{\text{DM}}^{-1} \lesssim 0.1 \text{ cm}^2 \text{ g}^{-1}$  with their study of the central densities of galaxy cluster. Finally Miralda-Escudé (2002) obtained tightest constraint,  $\sigma_{\text{SIDM}} m_{\text{DM}}^{-1} \lesssim 0.02 \text{ cm}^2 \text{ g}^{-1}$ , with their study of galaxy cluster halo shapes. However recent SIDM simulations (Peter et al., 2013; Rocha et al., 2013) have cast serious doubts on each of these previous constraints. Rocha et al. (2013) find that the previous subhalo evaporation and central density constraints are likely overestimated, and Peter et al. (2013) points out several weaknesses of the Miralda-Escudé (2002) work as

well as presents contradictory results. In summary Peter et al. (2013) and Rocha et al. (2013) find that the previous constraints need to be loosened to  $\sigma_{\text{SIDM}} m_{\text{DM}}^{-1} \lesssim 1.0 \text{ cm}^2 \text{ g}^{-1}$ . As will be discussed in §1.3.3,  $\sigma_{\text{SIDM}} m_{\text{DM}}^{-1}$  between  $\sim 0.3$ – $1.0 \text{ cm}^2 \text{ g}^{-1}$  has potentially interesting and desirable astrophysical implications.

### 1.3.3 Recent Motivation

After the burst of Y2K-era work, the field of SIDM essentially died, with only a few new constraints trickling in (Randall et al., 2008; Dawson et al., 2012; Merten et al., 2011). However, the field has recently entered a renaissance with extensive theoretical work (Arkani-Hamed et al., 2009; Feng et al., 2010; Tulin et al., 2012, 2013; Ackerman et al., 2009; Pospelov et al., 2008) and simulation work (Peter et al., 2013; Rocha et al., 2013; Vogelsberger et al., 2012; Vogelsberger & Zavala, 2013; Zavala et al., 2013). This renaissance can largely be attributed to three apparent conflicts between astrophysical observations and  $\Lambda$ CDM:

(i) Studies of the stellar kinematics in low surface brightness (LSBs) and dwarf spheroidal galaxies (dSphs; Simon et al., 2005; Kuzio de Naray et al., 2008; Oh et al., 2011) have shown that the radial velocity profiles of the stars in many halos are better fit by an isothermal density profile (i.e. cored profile) rather than an Navarro-Frenk-White (NFW; Navarro et al., 1996) density profile predicted by  $\Lambda$ CDM. In other words  $\Lambda$ CDM produces DM halos that are too cuspy in the central density profile, while an isothermal density profile suggests that there is energy exchange occurring in the centers of these galaxies which produced cored (or flattened) central density halo. Using SIDM simulations, Rocha et al. (2013) found that if  $\sigma_{\text{SIDM}} m_{\text{DM}}^{-1} \sim 0.5 \text{ cm}^2 \text{ g}^{-1}$  then there is enough thermal exchange between the DM to produce cores of the size observed in the LSBs and dSphs.

(ii) All observed dSphs of the Milky Way have  $12 \leq V_{\text{circ}}(r_{1/2}) \leq 20 \text{ km s}^{-1}$ , where  $V_{\text{circ}}(r_{1/2})$  is the circular velocity of particles at the half-light radius. The more mass there is within  $r_{1/2}$  the larger  $V_{\text{circ}}(r_{1/2})$ . Recent  $\Lambda$ CDM simulations of Milky Way-like halos predict that at least 10 dSphs should have  $V_{\text{circ}}(r_{1/2}) > 20 \text{ km s}^{-1}$  (Boylan-Kolchin et al., 2012). If the  $\Lambda$ CDM

simulations are correct then this would suggest that Milky Way is missing a significant number of large dSphs, or these large dSphs DM halos are devoid of stars which is entirely implausible. SIDM of allowable cross-section results in a nearly identical power spectrum at these scales and above (Rocha et al., 2013), thus these large dSphs will still exist in SIDM cosmologies. While this appears to be an entirely separate problem than the dSphs cusp/core problem previously mentioned, it may just be another perspective of exactly the same problem. Perhaps it is not that these massive dSphs are missing, but rather that their central densities are lower than predicted by  $\Lambda$ CDM (i.e. they are cored). If they are cored then some of the halo mass is diffused from the central  $r_{1/2}$  outwards. Thus the halo's mass could remain the same but  $V_{\text{circ}}(r_{1/2})$  would decrease. Again the work of Rocha et al. (2013) suggests that if DM self-interacts with  $\sigma_{\text{SIDM}} m_{\text{DM}}^{-1} \sim 0.5 \text{ cm}^2 \text{ g}^{-1}$  then the resulting central densities of the dSphs would be cored to such a degree to ameliorate this apparent discrepancy.

(iii) Finally on the much larger galaxy cluster scales, recent observations of their density profiles (Newman et al., 2013b,a) suggest that clusters have central cores at odds with  $\Lambda$ CDM. Comparison of the observed core size with simulations (Peter et al., 2013; Rocha et al., 2013) shows that  $\sigma_{\text{SIDM}} m_{\text{DM}}^{-1} = 1.0 \text{ cm}^2 \text{ g}^{-1}$  will produce cores larger than what is observed. However, SIDM with  $\sigma_{\text{SIDM}} m_{\text{DM}}^{-1} \sim 0.1-0.5 \text{ cm}^2 \text{ g}^{-1}$  is capable of producing the observed cores.

These observations all highlight inconsistencies with  $\Lambda$ CDM and simultaneously suggest SIDM with  $\sigma_{\text{SIDM}} m_{\text{DM}}^{-1} \sim 0.1-0.5 \text{ cm}^2 \text{ g}^{-1}$ . If  $\sigma_{\text{SIDM}} m_{\text{DM}}^{-1} \lesssim 0.1 \text{ cm}^2 \text{ g}^{-1}$  then SIDM is not capable of resolving any of these observed inconsistencies. Given the modified existing constraints of  $\sigma_{\text{SIDM}} m_{\text{DM}}^{-1} \lesssim 1.0 \text{ cm}^2 \text{ g}^{-1}$  this leaves a very narrow window of parameter space to explore.

## 1.4 Probes of SIDM

While laboratory experiments have placed tight constraints on the baryon-dark matter interaction cross-section ( $\sim 21$  orders of magnitude tighter than the current  $\sigma_{\text{SIDM}}$  constraints), these experiments are insensitive to DM-DM interactions. The only way to investigate whether DM self-interacts is through astrophysical observations (§1.3.2 summarized the various astrophysical methods for constraining SIDM).

As discussed in the previous section the greatest tensions with  $\Lambda$ CDM come from studies of the central densities of DM halos. This is true over a range of halo scales from LSBs to galaxy clusters. While such probes suggest that DM may self-scatter, each suffers from a *baryonic degeneracy*, where the observations might be explained by various baryonic processes/assumptions (e.g. AGN or supernova feedback, or the assumed initial mass function). In fact the important scales of these observations often coincide with baryonic scales (e.g. the core size in clusters is approximately the size of the brightest cluster galaxy; Newman et al., 2013b,a). What is needed is a probe of self-interacting dark matter (SIDM) where the expected effect is independent of these baryonic degeneracies. Merging galaxy cluster are such a probe.

## 1.5 Merging Galaxy Clusters as Probes of Self-Interacting Dark Matter

### 1.5.1 Merging Galaxy Clusters

According to the generally accepted model of structure formation, small structures (e.g. galaxies) form first, then through gravitational attraction they begin to merge and form larger structures (e.g. galaxy clusters). This process constantly repeats throughout the history of the universe and is known as the hierarchical structure formation model. When small structures merge with larger structures (e.g. dSphs merging with a galaxy or a galaxies

merging with a galaxy cluster) the smaller structures are often dramatically altered (often having some of their stars, gas and DM stripped from them), yet the larger structures remain mostly unaffected and there is little net change in the system. Occasionally structures of nearly the same size (e.g. two galaxies or two galaxy clusters) will merge. In these cases the system is often dramatically disturbed and will remain in such a disturbed state until dissipative processes (e.g. dynamic friction, and thermal radiation) cause the two structures to combine and the system to enter a relaxed state. It is the disturbed phase of merging galaxy clusters that provides the best means of testing whether DM self-interacts.

Merging galaxy clusters are the most energetic example of hierarchical structure formation. Figure 1.1 shows the generic time-series picture of a merging galaxy cluster leading to a *dissociative merger*, a highly disturbed system where the intracluster gas has become dissociated from the galaxies and DM. In the case of a dissociative merger two subclusters<sup>2</sup> begin with some physical separation, often significantly larger than the size of the individual subclusters. The mass of each subcluster is composed of  $\sim 2\%$  galaxies,  $\sim 15\%$  intracluster gas, and  $\sim 85\%$  DM. Through gravitational attraction the two subcluster accelerate towards one another with the relative velocity of each approaching free-fall velocity. Eventually the two subclusters collide<sup>3</sup> Because there is so much space between the galaxies, a strong interaction between any two galaxies is extremely unlikely and they can be treated as effectively collisionless particles. And since the galaxies of each subcluster have built up momentum they will pass through and begin to separate (this time on the opposite side; see  $t_5$  of Figure 1.1). The gas however is more evenly distributed, thus an interaction between the gas particles of each subcluster is more likely. These interactions will convert some of the infall kinetic energy into thermal energy (i.e. the gas of each subcluster will experience ram pressure), the net effect being that the gas halo of each subcluster is slowed with respect to the galaxies and much of it becomes dissociated remains centered between the galaxies of the two subclusters

---

<sup>2</sup>While they are both technically galaxy clusters they are termed subclusters to distinguish them from the galaxy cluster system they will eventually form when the merger is complete.

<sup>3</sup>The time of collision is defined to be the time of the first pericentric passage ( $t_4$  of Figure 1.1).

(‘C’ in  $t_6$  of Figure 1.1). Given that  $\sigma_{\text{SIDM}} m_{\text{DM}}^{-1} \lesssim 1.0 \text{ cm}^2 \text{ g}^{-1}$ , if the DM interacts it will be significantly less than the gas and behave more like the effectively collisionless galaxies. Thus the DM will predominately be located with the galaxies. It is during this disturbed phase of the merger ( $t_6$  of Figure 1.1) that it is termed dissociative and can provide the best constraints on  $\sigma_{\text{SIDM}} m_{\text{DM}}^{-1}$ .

### 1.5.2 Constraining Self-Interacting Dark Matter with Merging Galaxy Clusters

Markevitch et al. (2004) originally introduced (and applied to the Bullet Cluster) three methods for constraining  $\sigma_{\text{SIDM}}$  with observations of dissociative mergers. This was followed by Randall et al. (2008) who introduced (and also applied to the Bullet Cluster) an additional method of constraint by combining observations and simulations of dissociative mergers. These four methods are shown in Figure 1.2 and are discussed below.

#### 1.5.2.1 Dark Matter - Gas Offset

The first method that Markevitch et al. (2004) introduced used the fact that in the case of the Bullet Cluster the DM was observed to be significantly offset from the gas. According to the generic merger picture discussed in §1.5.1 this is because the collisional gas has a significantly larger scattering depth than the DM and thus is likely to self-interact and become dissociated from the DM. Thus Markevitch et al. (2004) setup the following inequality relating the scattering depth of the gas,  $\tau_{\text{gas}} \approx 1$ , to the scattering depth of SIDM,  $\tau_{\text{SIDM}} = \sigma_{\text{SIDM}} m_{\text{DM}}^{-1} \Sigma_{\text{DM}}$ .  $\Sigma_{\text{DM}}$  is the surface mass density of the DM particles. Markevitch et al. (2004) assumed that  $\Sigma_{\text{DM}}$  is approximately the WL measured surface mass density,  $\Sigma$ , since the majority of a typical cluster’s mass is DM.

$$\tau_{\text{gas}} \gtrsim \tau_{\text{SIDM}}$$

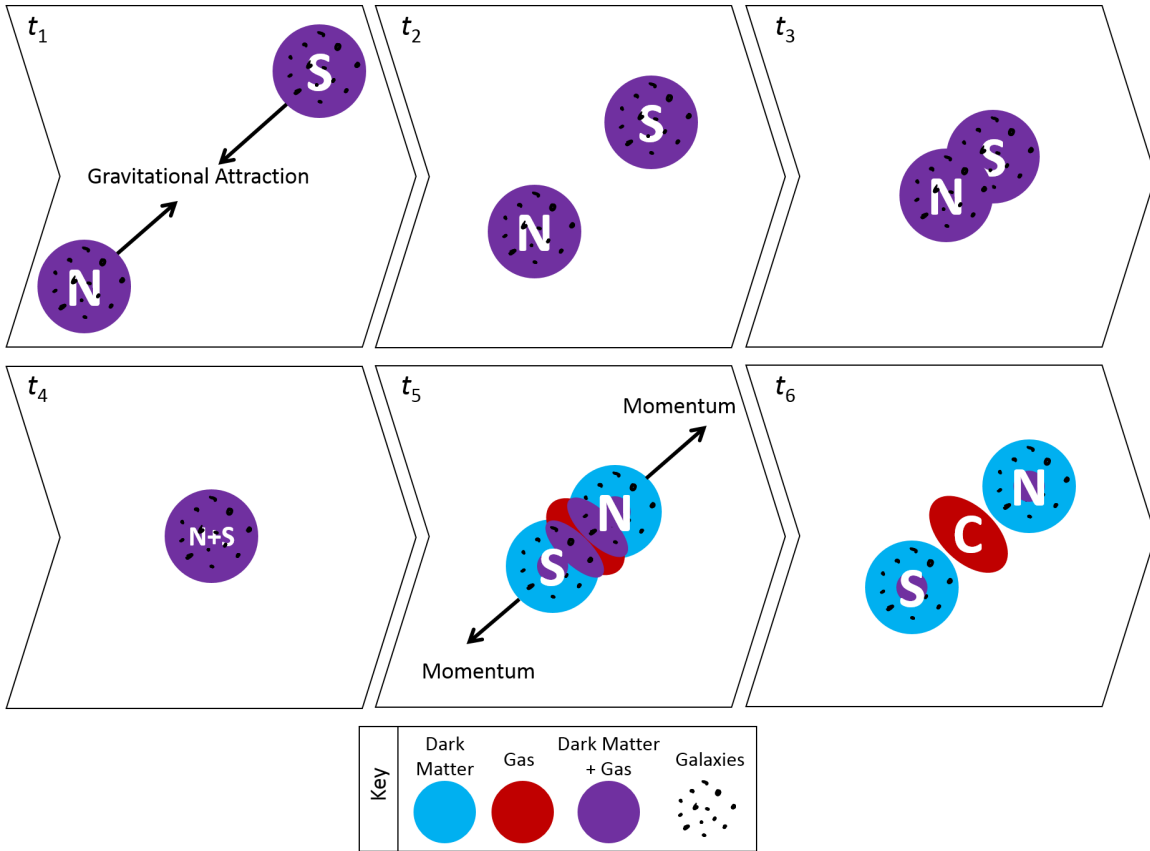


Figure 1.1 A basic time series leading to a dissociative galaxy cluster merger (assuming the Standard Model of Cosmology). Two galaxy clusters (N & S), each consisting of overlapping halos of DM and gas as well as sparsely populated galaxies, begin with an initial physical separation ( $t_1$ ). Due to the mass of each galaxy cluster they experience a gravitational attraction and accelerate towards one another until eventually they collide ( $t_1-t_4$ ). By convention time  $t_4$  is defined as the “collision”. The momentum of the effectively collisionless galaxies will cause them to pass through the impact,  $t_5$ , only slowed slightly by dynamic friction. The collisional gas will strongly self-interact, slowing significantly, and remain in the center ( $t_6$  C). Much like the galaxies the DM behaves in a nearly collisionless manner and appears largely coincident with the galaxies. Much like the galaxies the DM behaves in a nearly collisionless manner and appears largely coincident with the galaxies. At  $t_6$  the galaxy cluster merger is classed as *dissociative merger*. At later times dissipative processes (e.g. dynamic friction, and thermal radiation) will have caused the two structures to combine into a single relaxed galaxy cluster.

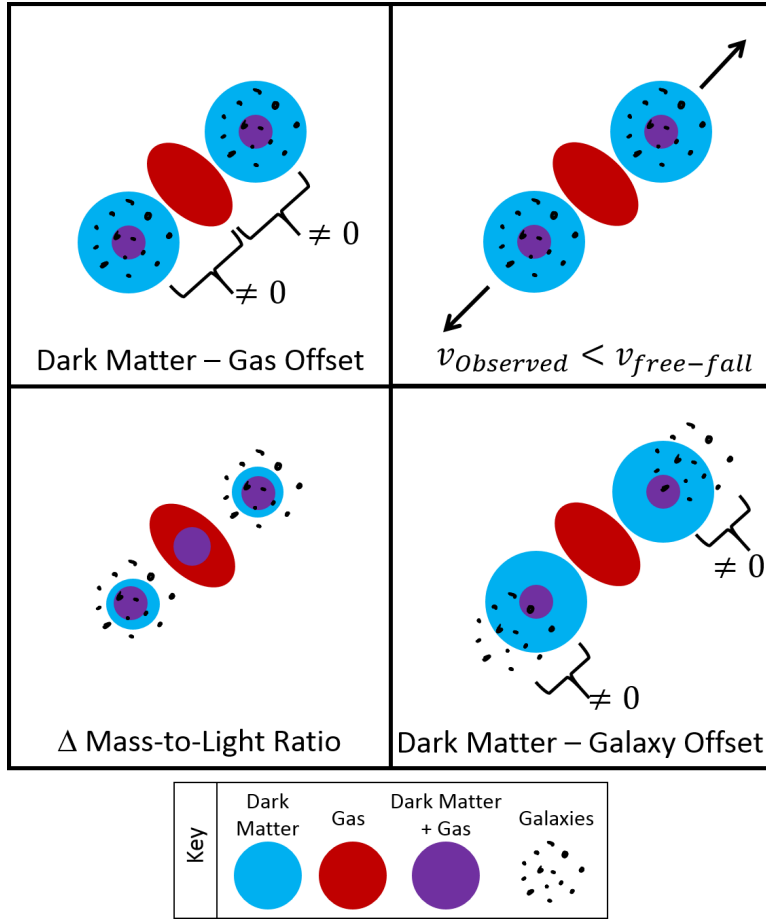


Figure 1.2 The four means of constraining  $\sigma_{\text{SIDM}}$  with merging clusters, originally outlined by Markevitch et al. (2004) and Randall et al. (2008). *Upper Left:* If the DM is significantly offset from the gas then the scattering depth of the dark matter ( $\tau_{\text{DM}}$ ) must be less than the scattering depth of the gas ( $\tau_{\text{gas}}$ ) and an upper limit can be placed on  $\sigma_{\text{SIDM}}$ . *Upper Right:* If DM self-interacts during the merger, then the velocity of each subcluster will be slowed to some degree. Thus if the observed velocity ( $v_{\text{obs}}$ ) is found to be consistent with the free-fall velocity ( $v_{\text{free-fall}}$ ) an upper limit can be placed on  $\sigma_{\text{SIDM}}$ . If however  $v_{\text{obs}}$  is significantly less than  $v_{\text{free-fall}}$ , an upper limit could be potentially placed on  $\sigma_{\text{SIDM}}$ . *Lower Left:* If DM self-interacts during the merger, then some fraction of the DM particles will scatter and become unbound from each subcluster. Thus the mass-to-light ratio of each subcluster can be compared with the mass-to-light ratio of similar non-merging clusters, and depending on whether the mass-to-light ratio of the merger is the same or less than the non-merging clusters' mass-to-light ratio, then respectively an upper limit or lower limit can be placed on  $\sigma_{\text{SIDM}}$ . *Lower Right:* If the DM self-interacts during the merger, then the DM component of each subcluster will experience an additional drag force and will travel at a slower velocity than the respective subcluster galaxies. Thus depending on whether a significant offset between the galaxies and DM is or is not observed, then respectively a lower limit or upper limit can be placed on  $\sigma_{\text{SIDM}}$ .

$$1 \gtrsim \frac{\sigma_{\text{SIDM}}}{m_{\text{DM}}} \Sigma_{\text{DM}}$$

$$\frac{\sigma_{\text{SIDM}}}{m_{\text{DM}}} \lesssim \Sigma_{\text{DM}}^{-1} \quad (1.1)$$

This method has been applied to a number of dissociative mergers (Markevitch et al., 2004; Dawson et al., 2012; Merten et al., 2011), with constraints ranging from  $\sigma_{\text{SIDM}} m_{\text{DM}}^{-1} < 3\text{-}8 \text{ cm}^2 \text{ g}^{-1}$ . This method has two notable disadvantages that are apparent from Equation 1.1: the constraint can only be improved by finding clusters with larger  $\Sigma_{\text{DM}}$  and that the constraint is directly proportional to the inverse surface mass density. Two of the existing constraints (Markevitch et al., 2004; Merten et al., 2011) come from extremely dense clusters. To better the existing  $\sigma_{\text{SIDM}} m_{\text{DM}}^{-1}$  by the necessary order of magnitude would require clusters with surface mass densities an order of magnitude higher than both the Bullet Cluster and Abell 2744. Such clusters are highly unlikely to exist, thus this method has little value for future constraints of SIDM.

### 1.5.2.2 Velocities of the Subclusters

Markevitch et al. (2004) noted that the Bullet Cluster merger velocity inferred from the X-ray gas shock feature “is in good agreement with the expected free-fall velocity”. They then argued that if DM self-interacts then each subcluster will decelerate, resulting in a velocity difference between the observed velocity,  $v_{\text{obs}}$ , and the free-fall velocity,  $v_{\text{free-fall}}$ :

$$v_{\text{obs}} - v_{\text{free-fall}} = \frac{\bar{p}}{m_{\text{DM}}} \frac{\sigma_{\text{SIDM}}}{m_{\text{DM}}} \Sigma_{\text{DM}},$$

where  $\bar{p}$  is the average momentum lost by the subcluster in each particle collision.

This method has only been applied to the Bullet Cluster (Markevitch et al., 2004), and resulted in a constraint of  $\sigma_{\text{SIDM}} m_{\text{DM}}^{-1} \lesssim 7 \text{ cm}^2 \text{ g}^{-1}$ . The predominant reason this method has not been applied to more mergers is that it is very difficult to constrain the three-dimensional

velocity of the merger (Dawson, 2013), which is necessary to estimate  $\bar{p}$ . Often times the only direct observation of the merger velocity comes from spectroscopic redshifts of the subcluster galaxies, and these only provide information about the line-of-sight velocity component of the merger. In the case of the Bullet Cluster however, the X-ray gas has been shocked due to the merger velocity being greater than the sound speed of the gas. From this shock Markevitch et al. (2002) were able to estimate the Mach number of the merger, which in turn provided them with an estimate of the three-dimensional merger velocity. Most clusters do not have such a well defined shock feature.

While it was originally believed that the three-dimensional merger velocity could be inferred from the X-ray shock feature, Springel & Farrar (2007) showed that the X-ray shock inferred velocity significantly overestimates the true three-dimensional merger velocity. This coupled with the fact that  $v_{\text{obs}}$  is expected to vary throughout the merger and always be less than  $v_{\text{free-fall}}$  suggests that the existing constraints from this method should be questioned. Further more it seems unlikely that the constraints will ever improve upon existing SIDM constraints.

### 1.5.2.3 Mass-to-Light Ratio

Markevitch et al. (2004) noted that if DM self-interacts during the merger, then some fraction of the DM particles will scatter and become unbound from each subcluster. Thus the mass-to-light ratio ( $M/L$ ) of each subcluster can be compared with the  $M/L$  of similar non-merging clusters, and depending on whether the  $M/L$  of the merger is the same or less than the non-merging clusters'  $M/L$ , then respectively an upper limit or lower limit can be placed on  $\sigma_{\text{SIDM}}$ . Clowe et al. (2004) claim that the  $M/L$  of the Bullet Cluster are in “good agreement with the universal cluster values from the lensing analyses (e.g., Mellier, 1999; Dahle, 2000).” This enabled Markevitch et al. (2004) to place a constraint of  $\sigma_{\text{SIDM}} m_{\text{DM}}^{-1} \lesssim 1 \text{ cm}^2 \text{ g}^{-1}$ . Randall et al. (2008) were able to improve upon this constraint by simulating the Bullet Cluster with collisionless “galaxy” particle and collisional SIDM particles. And by varying  $\sigma_{\text{SIDM}}$  between

collisions. They found that for  $\sigma_{\text{SIDM}} m_{\text{DM}}^{-1} < 0.7 \text{ cm}^2 \text{ g}^{-1}$ , otherwise the M/L decreased by more than  $\sim 23\%$  in their simulation, which they claimed was not reasonable given the measured M/L of the subclusters.

While this method has provided the tightest  $\sigma_{\text{SIDM}} m_{\text{DM}}^{-1}$  constraints there are a number of assumptions and possible systematic errors to consider more seriously. First and foremost the method assumes that all clusters have close to the same ( $\lesssim 40\%$  difference) M/L. However as Dahle (2000) shows there is significant variance in the M/L of galaxy clusters with  $100 \lesssim h(M/L_B) \lesssim 1000$ . Secondly, it is well established that galaxy clusters play an important role in the evolution of their member galaxies, but it is still unclear whether cluster mergers trigger star formation (e.g. Miller & Owen, 2003; Owen et al., 2005; Ferrari et al., 2005; Hwang & Lee, 2009), quench it (Poggianti et al., 2004), or have no immediate effect (Chung et al., 2010). Thus it is unclear what affects the cluster merger will have on the luminosities of the subclusters. Finally there are a number of biases (see e.g. Noh & Cohn, 2011) and systematic errors (Randall et al., 2008, discuss several) that can affect the gravitational lensing estimated mass. Because of these issues caution should be used when applying this method to constrain SIDM.

#### 1.5.2.4 Dark Matter - Galaxy Offset

The method introduced by Randall et al. (2008) is based upon the fact that if DM self-interacts during the merger, then the DM component of each subcluster will experience an additional drag force and will decelerate with respect to the respective subcluster galaxies. Initially this velocity difference will result in a DM-galaxy offset that increases with time. Thus depending on whether a significant offset between the galaxies and DM is or is not observed, then respectively a lower limit or upper limit can be placed on  $\sigma_{\text{SIDM}}$ .

Using the same galaxy-DM simulations referenced in §1.5.2.3 Randall et al. (2008) found, as expected, that as they increased  $\sigma_{\text{SIDM}}$  the offset between their collisionless “galaxy” particles and there SIDM particles increased. Then given the observed galaxy and lensing cen-

troids and the uncertainty on these centroids they claimed they could rule out any scenarios where SIDM resulted in an offset greater than  $\sim 50$  kpc. This corresponded to a constraint of  $\sigma_{\text{SIDM}} m_{\text{DM}}^{-1} < 1.25 \text{ cm}^2 \text{ g}^{-1}$ . Interestingly Randall et al. (2008) note that the observed galaxy centroid is leading the lensing mass centroid by  $5.7'' \pm 6.6''$  ( $25 \pm 29$  kpc), yet rather than try to estimate the value of  $\sigma_{\text{SIDM}} m_{\text{DM}}^{-1}$  based on this offset they only took the extreme and fit an upper limit. According to their simulations an offset of  $\sim 25$  kpc is seen in their simulation with  $\sigma_{\text{SIDM}} m_{\text{DM}}^{-1} \approx 0.7 \text{ cm}^2 \text{ g}^{-1}$  Granted that with offset uncertainties of order the measured offset there is little confidence in this estimate

This method has the advantage that the scales of interest are typically  $\gtrsim 25$  kpc. Thus this method is immune to the baryonic degeneracies that weaken the constraining power of other SIDM constraining methods (e.g. central halo density). The method does have number of sources of noise and systematic error that need to be considered, in addition to the Poisson noise of the centroid measurements. The important offset for this method is the three-dimensional offset between the galaxies and the DM. What can be measured is the projected offset between the galaxies and the lensing centroid. As will be discussed in Chapter 4 there is considerable uncertainty when converting between projected and three-dimensional distances of merging cluster systems. While this uncertainty is not important for determining if there is a significant offset between the galaxies and dark matter (that would suggest  $\sigma_{\text{SIDM}} > 0$ ) it is important if we wish to quantify  $\sigma_{\text{SIDM}} m_{\text{DM}}^{-1}$ . The other key limitation is that we cannot directly measure the DM centroid, we are only able to measure the total projected mass with gravitational lensing. The lensing centroid can then diverge from the DM centroid for a number of reasons. The fact that these are dissociative mergers means that  $\sim 10\%$  of the cluster mass is in between the two subclusters. This gas mass will act to pull the lensing centroid away from the DM centroid towards the center of the cluster. This systematic effect will exactly mimic the effect expected if DM self-interacts. Similarly the mass of one subcluster will pull the lensing centroid of the other subcluster away from the DM centroid and towards the center. This effect may be countered to some degree since the

galaxy centroid will experience a similar effect. Without simulations it is unclear if these two effects will completely null one another. Finally, lensing is sensitive to all mass along the line of sight. Thus foreground or background large scale structures could cause a random offset in the lensing centroid from the DM centroid of the subcluster. Dietrich et al. (2012) found that projected large scale structure results in a  $\sim 4''$  random offset of the lensing centroid from the true DM centroid. As will be discussed in Chapter 4 these sources of noise and systematic error can be mitigated. Thus it seems as though this method holds the most promise for constraining  $\sigma_{\text{SIDM}} m_{\text{DM}}^{-1}$ .

Problems with the (Randall et al., 2008) approach and possible means of improvement? This could be covered to some degree in Chapter 5.

### 1.5.3 Advantages of Merging Clusters Over other Probes of Self-interacting Dark Matter

*This section is optional*

A disadvantage is that a wide range of observations are necessary to study merging clusters.

## 1.6 Work Presented in this Dissertation

Briefly summarize each chapter. *This section is optional*

## Chapter 2

# Musket Ball Cluster: Observed Properties

This chapter is an expanded version of the article titled *Discovery of a Dissociative Galaxy Cluster Merger with Large Physics Separation* which was published in the March 2012 issue of the Astrophysical Journal Letters (Volume 747, pp. L42).

We present DLSCL J0916.2+2951 ( $z=0.53$ ), a major cluster merger in which the collisional cluster gas has become dissociated from the collisionless galaxies and dark matter. We identified the cluster using optical and weak lensing observations as part of the Deep Lens Survey. Our follow-up observations with *Keck*, *Subaru*, *Hubble Space Telescope*, and *Chandra* show that the cluster is a dissociative merger.

### 2.1 Introduction

We have identified a new dissociative merger, DLSCL J0916.2+2951, that probes an unexplored area of merger phase-space. We originally detected the cluster in the Deep Lens Survey (DLS; Wittman et al., 2002) via its weak lensing (WL) shear signal. It consists of two main subclusters spectroscopically confirmed to be at the same redshift (0.53). This

cluster was also observed in the Sunyaev-Zel'dovich Array Survey (Muchovej et al., 2011) which provided evidence that the cluster gas is dissociated from the bulk of the mass and galaxies (Figure 2.6). Follow-up optical observations with *Subaru* and *HST* enable higher resolution mass maps and follow-up X-ray observations with *Chandra* ACIS-I confirm that the majority of the gas is offset between the North and South subclusters, the signature of a dissociative merger (Figure 2.1).

In this letter we introduce DLSCL J0916.2+2951 and summarize our survey of its three dominant components (galaxies, DM, and gas) and the cluster's astrophysical implications. A more thorough exposition of the survey and analysis will be presented in Dawson et al. (in preparation). Throughout this paper we assume  $\Omega_\Lambda = 0.7$ ,  $\Omega_m = 0.3$ , and  $H = 70 \text{ km s}^{-1} \text{ Mpc}^{-1}$ .

## 2.2 Photometric

We obtained  $B$ ,  $V$ ,  $R$ , and  $z'$  photometric data (12, 12, 18, and 12 ksec, respectively) with Mosaic 1 on the KPNO 4-m *Mayall* telescope as part of the DLS. To improve the accuracy of our photometric redshifts we also observed the cluster in three medium-width optical bands ( $g$ ,  $h$ , and  $i$  from the BATC filter set), bracketing the redshifted 4000 Å feature, using the upgraded Mosaic 1.1 imager on the KPNO *Mayall* with exposure times of 6 ks per filter (2011 April 22–24). We estimate colors using *ColorPro* (Coe et al., 2006) and redshifts using *BPZ* (Benítez, 2000). We replace the standard templates with a set “tweaked” in a method similar to that described in Ilbert et al. (2006), using spectroscopic samples from SHELS (Geller et al., 2005) and the PRIMUS survey (Coil et al., 2011) which overlap the DLS. Figure 4.2 shows the density isopleths of galaxies with  $0.43 < z_{\text{phot}} < 0.63$  (roughly the cluster redshift  $\pm \sigma_{z_{\text{phot}}}$ ). This map agrees well with the distribution of spectroscopically confirmed cluster members.

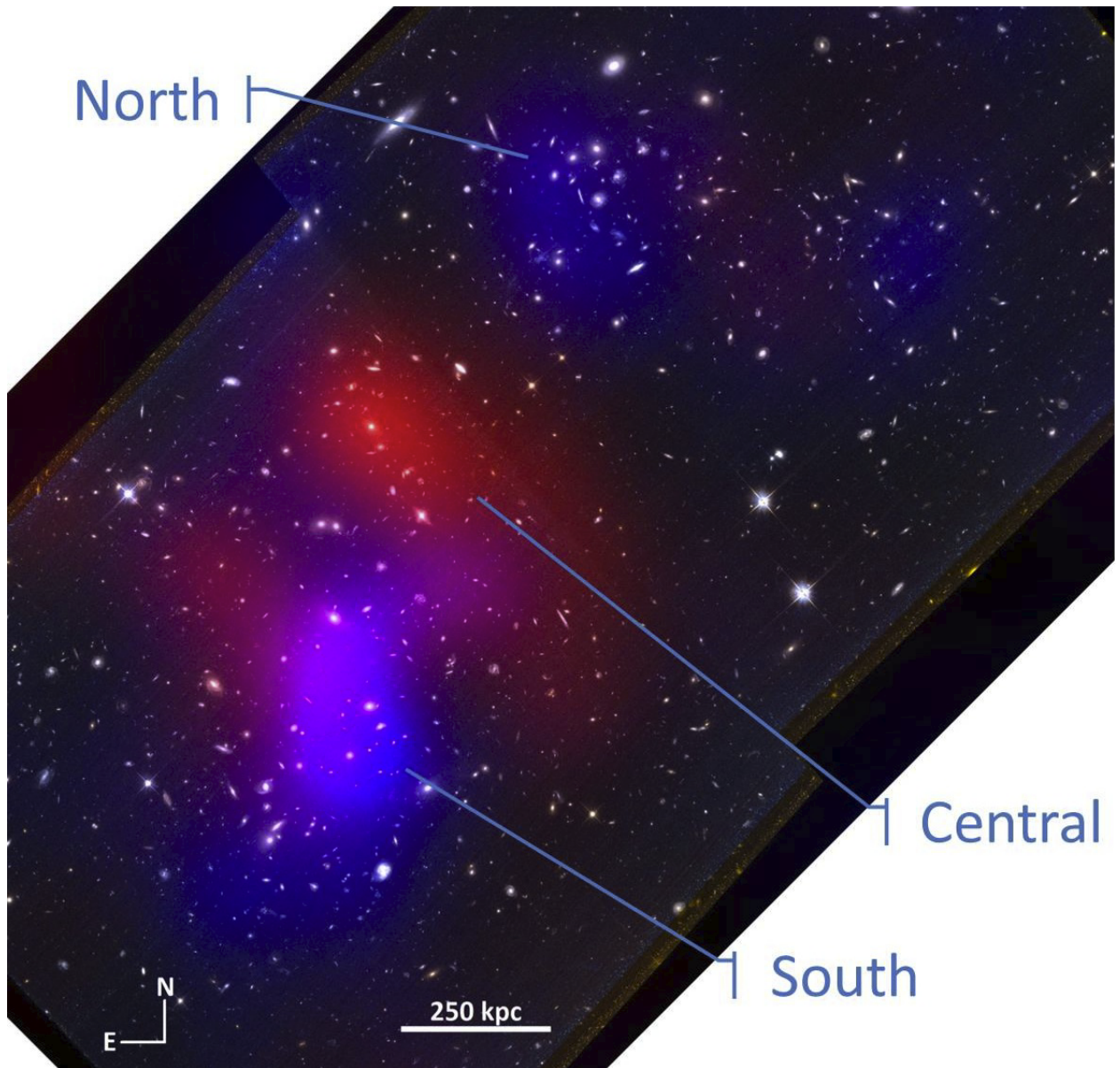


Figure 2.1 Merging cluster DLSCL J0916.2+2951 and its three matter components. Overlaid on the HST color image of the galaxies is the total mass distribution (blue) based on WL analysis of the HST images and the cluster gas distribution (red) based on Chandra X-ray observations. The bulk of the collisional gas is located between the two collisionless galaxy and mass concentrations, indicative of a dissociative merger. The image is  $5' \times 5'$  ( $\sim 1.9 \times 1.9 \text{ Mpc}^2$  at  $z = 0.53$ ).

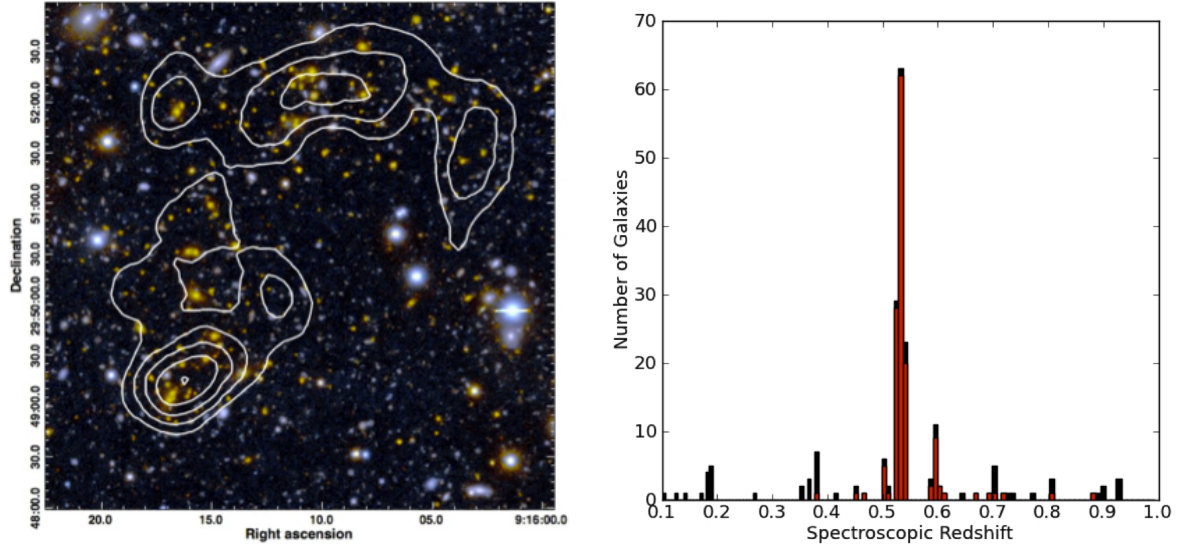


Figure 2.2 *Left:* DLS composite  $BVR$  color image of DLSCL J0916.2+2951 showing the galaxies of the two subclusters. The white contours represent the number density of galaxies with  $z_{\text{phot}} = 0.53 \pm 0.1$ , the cluster redshift  $\pm \sigma_{z_{\text{phot}}}$ . The contours begin at 200 galaxies  $\text{Mpc}^{-2}$  with increments of 50 galaxies  $\text{Mpc}^{-2}$ . The image field-of-view is the same as Figure 2.1. *Right:* Histogram of the 200 observed spectroscopic redshifts within the field of view of the *left* figure. The red portion is the subsample that passes the  $z_{\text{phot}} = 0.53 \pm 0.1$  criteria. The galaxies at  $z \sim 0.6$  had equal probability of selection as the cluster members and show no sign of clustering.

## 2.3 Spectroscopic

We obtained spectroscopic redshifts for 20 cluster members with *Keck* LRIS (2007 January 16) and 634 unique spectroscopic redshifts ( $0 < z < 1.2$ ) in a  $\sim 15' \times 15'$  area centered on the cluster with *Keck* DEIMOS (2011 March 2–3), including 132 members at the cluster redshift. We reduced the LRIS spectra using a scripted sequence of standard IRAF reduction tasks, and the DEIMOS spectra using a modified version of the DEEP2 *spec2d* package (Davis et al., 2003; Gal et al., 2008; Lemaux et al., 2009).

We use our full sample of 654 spectroscopic redshifts as well as photometric redshifts to identify potential line-of-sight structures which may confuse our results. We find no evidence for significant line-of-sight structure (Figure 4.2).

We estimate each subcluster’s redshift and velocity dispersion (Table 2.1) using the biweight-statistic and bias-corrected 68% confidence limit (Beers et al., 1990) applied to 100,000 bootstrap samples of each subcluster’s spectroscopic redshifts. Our redshift estimates indicate a line-of-sight velocity difference of  $v_{\text{los}} = 670^{+270}_{-330} \text{ km s}^{-1}$  between the North and South subclusters, using the galaxies within a 0.5 Mpc radius centered on the *HST* WL mass peaks and within a velocity range of  $\pm 3000 \text{ km s}^{-1}$  of  $z=0.53$  ( $\sim 3 \times$  the expected velocity dispersion); corresponding to 38 and 35 galaxies for the North and South subcusters, respectively. These results are robust against varying the velocity range  $\pm 1000 \text{ km s}^{-1}$  and using the Subaru WL or galaxy number density peaks as the apertures’ centers, provided the aperture radius is  $\lesssim 0.5 \text{ Mpc}$ : larger radii lead to significant subcluster membership confusion. Additionally, we report the velocity dispersion mass estimates based on the scaling relation of Evrard et al. (2008) in Table 2.1. We note that the velocity dispersions should be interpreted with caution since this is a disturbed system.

Table 2.1. Observed subcluster and X-ray concentration properties

Subcluster	Redshift	$\sigma_v$ (km s $^{-1}$ )	$\sigma_v M_{200}$ ( $10^{14} M_\odot$ )	WL $M_{200}$ ( $10^{14} M_\odot$ )	$L_{X_{0.5-2\text{keV}}}$ ( $10^{43} \text{erg s}^{-1}$ )	$T_X$ (keV)	X-ray S/N	Joint WL S/N
North	$0.53074^{+0.00068}_{-0.00064}$	$740^{+130}_{-190}$	$3.7 \pm 2.3$	$1.7^{+2.0}_{-0.72}$	0.63	...	3.2	3.0
South	$0.53414^{+0.00065}_{-0.00064}$	$770^{+110}_{-92}$	$4.1 \pm 1.6$	$3.1^{+1.2}_{-0.79}$	2.1	$2.7^{+1.2}_{-0.7}$	7.0	6.7
Central	...	...	...	...	2.8	$2.2^{+1.4}_{-0.6}$	9.1	-3.3 <sup>a</sup>

<sup>a</sup>The negative WL S/N indicates a projected surface mass local under-density.

## 2.4 Weak Lensing

To map the total mass distribution we use a version of the Fischer & Tyson (1997) method modified to include a novel tomographic signal-matched filter. The cluster's WL shear signal,  $\gamma$ , depends not only on the projected surface mass over-density of the cluster,  $\Delta\Sigma$ , but on the relative distances of the observer, the mass, and the background galaxies:

$$\gamma = \frac{\Delta\Sigma}{\Sigma_{cr}} = \frac{\Delta\Sigma 4\pi G}{c^2} \frac{D_{ls}(z_l, z_s) D_l(z_l)}{D_s(z_s)} \mathcal{H}\left(\frac{z_s}{z_l} - 1\right),$$

where  $\Sigma_{cr}$  is the critical surface density,  $\mathcal{H}$  is the Heaviside step function, and  $D_l$ ,  $D_s$ , &  $D_{ls}$  are the angular diameter distances to the lens, source, and between the lens and source, respectively. Since we do not have exact redshift measurements of the source galaxies we use each galaxy's photometric redshift probability distribution function,  $p(z)$ , to estimate a respective  $\Sigma_{cr}$  for a given lens redshift,

$$\Sigma_{cr}(z_l) \approx \langle \Sigma_{cr}(z_l) \rangle = \int \Sigma_{cr}(z_l, z_s) p(z_s) dz_s.$$

In addition to weights based on shape measurement errors, we also weight the shear of each galaxy based on its  $p(z)$ ,

$$w_\gamma(z_l) = \frac{1}{\int [\Sigma_{cr}(z_l, z_s) - \langle \Sigma_{cr}(z_l) \rangle]^2 p(z_s) dz_s}.$$

This method increases the signal-to-noise of the measurement (see e.g. Hennawi & Spergel, 2005), and more accurately accounts for the errors inherent in the photometric redshift estimates, compared to single-point estimates. We estimate uncertainties using 100 bootstrap resamplings.

Encouraged by the DLS mass and galaxy maps we obtained higher-resolution ground and space based observations. *Subaru* Suprime-Cam  $i'$ -band coverage of the cluster was provided by engineering-time observations of DLS Field 2 (2008 January 8). We use the Suprime-Cam data reduction software *SDFRED* (Yagi et al., 2002; Ouchi et al., 2004) followed by *SCAMP* & *SWARP* (Bertin et al., 2002; Bertin, 2006) to refine the astrometry and make the final mosaic. DLSCL J0916.2+2951 was also observed with *HST* ACS/WFC using F606W and F814W filters (GO-12377, PI-W. Dawson) in a  $2 \times 1$  pointing mosaic that covers the subclusters (Figure 2.1). The exposure times for F606W and F814W are 2520s and 4947s per pointing, respectively. We reduce this data following a method similar to that presented in Jee & Tyson (2009). We measure the PSF of both datasets using the PCA method presented in Jee et al. (2007).

We perform our WL analysis independently on both the Subaru and HST F814W data. The Subaru data has  $0.72''$  seeing and 49 WL-quality source galaxies (i.e. background galaxies with measured ellipticity error  $< 0.3$ ) per arcmin $^2$ . For the mass map we use an apodizing kernel radius of  $0.5'$ , which can be interpreted as the effective resolution of the WL mass map. We are able to cross-match most of the detected objects with the DLS and use the  $p(z)$ 's discussed in the previous section.

Cross-matching is more problematic with the higher-resolution HST data, so we use a color-magnitude cut ( $F606W - F814W < 0.8$  and  $24 < F814W < 28.5$ ) to select source galaxies and exclude cluster red-sequence and bright foreground galaxies, see Figure 2.3. For the WL analysis of the HST F814W image, which has a  $0.1''$  PSF and 136 WL-quality source galaxies per arcmin $^2$ , we use an apodizing kernel radius of  $3.6''$ . We find no significant spatial correlation between source density and subcluster position, suggesting that our source galaxy

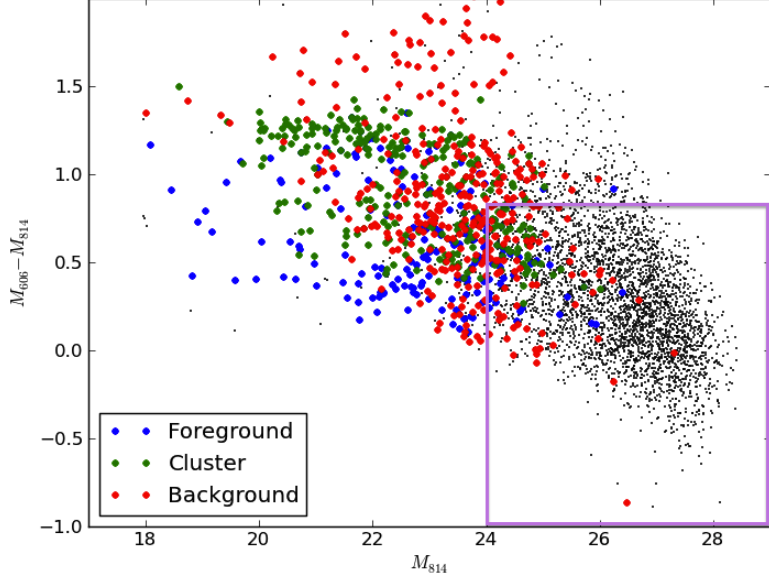


Figure 2.3 Muskett Ball Cluster color-magnitude diagram based on HST photometry. The larger color points are cross-matched DLS objects which have been divided into *Foreground* (blue;  $z_{\text{phot}} < 0.43$ ), *Cluster* (green;  $z_{\text{phot}} = 0.53 \pm 0.1$ ), and *Background* (red;  $z_{\text{phot}} > 0.63$ ) samples. Note that the photometric redshifts become relatively unreliable for  $M_{814} > 24$ . The purple box indicates the HST source galaxy sample.

population is not significantly contaminated with cluster galaxies. Furthermore, we find a comparable number distribution of sources as a function of magnitude when we make similar cuts to the HUDF (Coe et al., 2006) and GOODS North & South (Giavalisco et al., 2004) galaxy catalogs, indicating negligible cluster contamination, see Figure 2.4. We estimate the  $p(z)$  of our HST source galaxy sample by assuming the photometric redshift distribution of the Coe et al. (2006) HUDF catalog after applying our color-magnitude cut. Figure 4.1 shows excellent agreement between the Subaru and HST WL mass, and galaxy density maps.

We construct a joint catalog from the HST and Subaru data, using the HST data where available and Subaru for the surrounding area. Using a tomography-based MCMC analysis we simultaneously fit NFW halos centered on the North and South HST WL peaks, and use the Gelman & Rubin (1992) convergence test applied to eight independent chains. In order to reduce the number of free parameters we use the Duffy et al. (2008) empirical relation between  $M_{200}$  and concentration. We present the most likely masses for each halo along with the bias-corrected 68% confidence limits in Table 2.1. We also compare the integrated

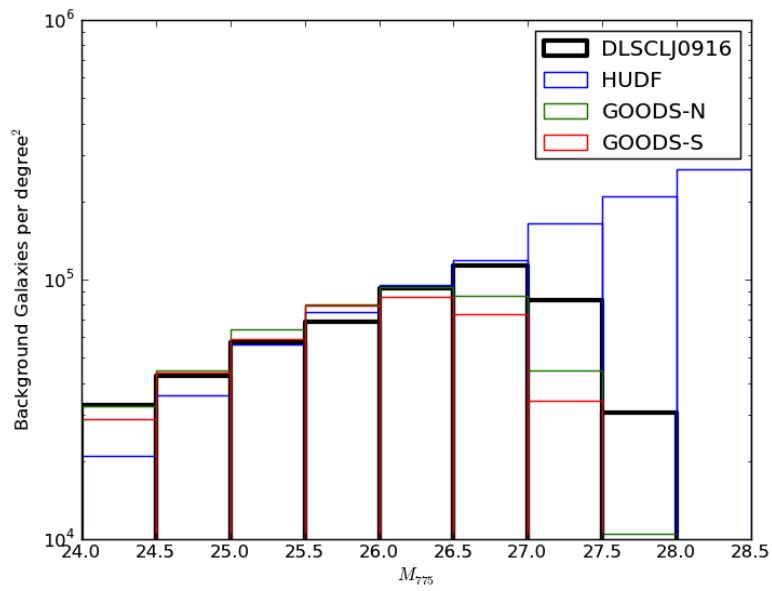


Figure 2.4 Comparison of the Musket Ball Cluster, HUDF (Coe et al., 2006) and GOODS North & South (Giavalisco et al., 2004) source galaxy densities. The HUDF field has a depth of 288 F775W orbits, the GOODS survey has a depth of one F775W orbit, and the Musket Ball Cluster has a depth of 2 F814W orbits (the F814W filter is comparable to the F775W filter). Up to the completeness of each survey we find a comparable number distribution of sources as a function of magnitude when we make similar cuts to each galaxy catalog, indicating negligible cluster contamination.

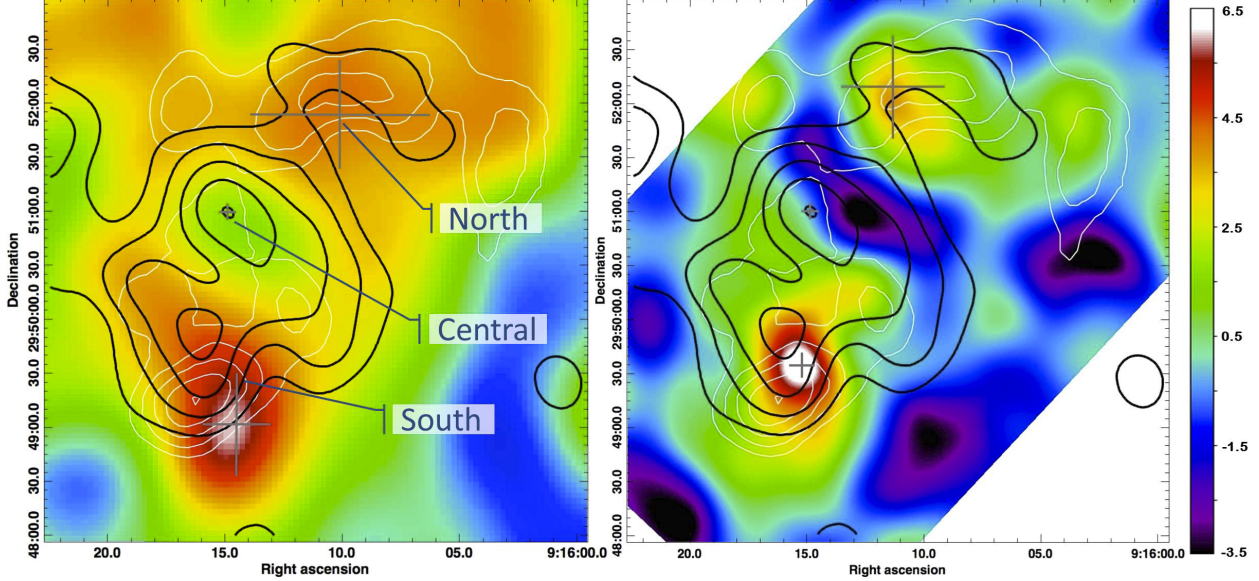


Figure 2.5 Comparison of the Subaru  $i'$ -band ground-based (left) and HST space-based (right) WL mass signal-to-noise maps (color) of DLSCL J0916.2+2951 with the X-ray distribution (bold black contours) and galaxy number density (white contours, same as Figure 4.2). The peak centers and corresponding one sigma errors are denoted by the gray cross-hairs. In both analyses there is agreement between the location and relative magnitude of galaxies and WL yet the majority of the cluster gas is centered  $\sim 1.4'$  between the North and South subclusters in a local mass underdensity, providing evidence that the North and South subclusters have undergone the first pass-through of a major merger. The scale of each map is equivalent and the image field-of-view is the same as Figures 2.1 & 4.2. The map created from the joint Subaru/HST catalog looks nearly identical to the HST map, with only slight variations in the scale (see Table 2.1).

projected surface mass density of the NFW halos with the measured WL aperture mass (Fahlman et al., 1994) of each subcluster and find agreement within a radius of 0.5 Mpc of each subcluster.

## 2.5 Sunyaev–Zel'dovich Effect

This cluster was also observed in the Sunyaev-Zel'dovich Array Survey (Muchovej et al., 2011). They found a  $4\sigma$  SZE signal roughly consistent with that expected for clusters of this mass. The signal is offset  $\sim 1'$  ( $\sim 0.4$  Mpc) from the southern subcluster and  $\sim 3'$  ( $\sim 1$  Mpc) from the northern subcluster. The SZE traces the cluster ICM and can be used to

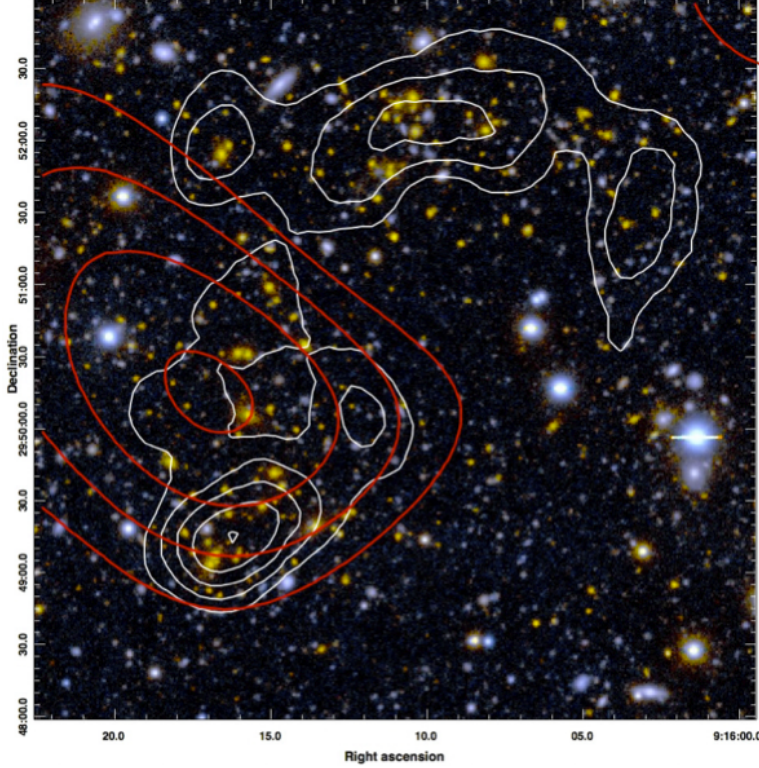


Figure 2.6 DLS composite  $BVR$  color image of DLSCL J0916.2+2951 showing evidence that the cluster gas, represented by the solid red SZE decrement significance contours ( $1, 2, 3, 4\sigma$ ), is offset  $\sim 1'$  ( $\sim 0.4$  Mpc) and  $\sim 3'$  ( $\sim 1$  Mpc) from the two subclusters, represented by the white galaxy number density contours for galaxies with  $z_{\text{phot}} = 0.53 \pm 0.1$  (beginning at  $200$  galaxies  $\text{Mpc}^{-2}$  with increments of  $50$ ). The image field-of-view is the same as Figure 2.1. The beam of the SZ observation has a radius of  $\sim 1'$ .

identify an offset of the ICM relative to the galaxies and dark matter (as in the case of the Bullet Cluster Halverson et al., 2009). This shift provided the first evidence that the cluster gas is dissociated from the bulk of the mass and galaxies (Figure 2.6).

## 2.6 X-ray

We acquired X-ray spectral-imaging of the cluster with 40ks of *Chandra* ACIS-I time (GO-12800854), and reduce it using *CIAO* version 4.2 and *CALDB* version 4.4.1. We manually identify X-ray point sources and mask them before adaptively smoothing the diffuse emission, we present the resulting map in Figure 4.1. We estimate source counts and their error

using the *dmextract* function of *CIAO*. We use an  $8'$  radius background region which encloses the subcluster regions and rests  $\sim 90\%$  on ACIS-I3 (on which the subclusters are observed). In the estimate of the background counts each subcluster region, chip gap, and point source are excluded. The subcluster exclusion regions were defined such that they encompassed the source emission and were extended out to approximately the  $\text{SNR} = 1$  level based on the smoothed map. In total we there were  $1800 \pm 40$  background counts in  $620,000 \text{ pixel}^2$  area within the energy range of  $0.5\text{-}2 \text{ keV}$ . For the South and Central X-ray concentrations ( $120 \pm 17$  and  $170 \pm 19$  detected  $0.5\text{-}2 \text{ keV}$  photons, respectively) we use the *Xspec* X-ray spectral fitting tool (Arnaud, 1996) to fit a Mewe-Kaastra-Liedahl plus photoelectric absorption model (fixed to the Leiden/Argentine/Bonn value; Kalberla et al., 2005) to the X-ray spectrum of each X-ray concentration. For the North concentration there are not enough detected X-ray photons ( $38 \pm 12$ ) to fit a meaningful spectrum. We report the results of this analysis in Table 2.1. We define the subcluster exclusion regions such that they encompass the source emission and extend out to approximately the  $1\sigma$  level based on the smoothed map. In total there are  $1800 \pm 40$  background counts in the  $620,000 \text{ pixel}^2$  area and  $0.5\text{-}2 \text{ keV}$  energy range. For the North, South, and Central X-ray concentrations we find  $38 \pm 12$ ,  $120 \pm 17$  and  $170 \pm 19$  detected  $0.5\text{-}2 \text{ keV}$  photons, respectively.

To estimate the temperatures of the South and Central concentrations we use the *Xspec* X-ray spectral fitting tool (Arnaud, 1996) to fit a Mewe-Kaastra-Liedahl plus photoelectric absorption model (fixed to the Leiden/Argentine/Bonn value; Kalberla et al., 2005) to the X-ray spectrum of each X-ray concentration. For the North concentration there are not enough detected X-ray photons to fit a meaningful spectrum. Due to the low count regime and our use of the  $\chi^2$  statistic we rebin the data so that each spectral channel used in the fit contains at least 20 counts. The binning is carried out on the spectra before background subtraction; these raw spectra contained 843 (1070) counts in the South (Central) subcluster. Since the background spectrum contains 7725 counts, each spectral bin in the background is far above the 20 count threshold. Binning data in this manner does reduce the spectral

resolution, however for hot clusters like those in our study the number of final spectral bins we have (31 for the southern and 39 for the central subcluster, which include cuts on the highest energy channels) are sufficient to determine the temperature, since the spectrum is dominated by bremsstrahlung emission which has few sharp spectral features. We report the results of this analysis in Table 2.1.

## 2.7 Radio

Since the Musket Ball cluster is a strong merger with an X-ray inferred Mach number of  $\gtrsim 3$  whose axis is likely to be close to the plane of the sky (Dawson, 2013), it is a prime candidate for a double radio relic. Radio relics are irregularly shaped radio sources, located at the outskirts of galaxy clusters, characterized by steep radio spectrum<sup>1</sup> with  $\alpha \leq -1.2$ . Radio relics are thought to be produced by relativistic particles that have been accelerated by shock waves in the ICM. Double relics show relics on opposite sides from the cluster center and form a subset of relics for which the merger geometry can be constrained particularly well (see e.g. Bonafede et al., 2012).

Since the Musket Ball Cluster is at a later stage than all other dissociative mergers (Dawson et al., 2012) and is thought to have shocks with  $M > 3$ , the detection of radio relics would provide constraints on the merger geometry. This has direct implications for the measurement of the dark matter cross-section with the Musket Ball since observed projected offsets must be translated into meaningful physical offsets (see e.g. Dawson, 2013). The degree of polarization provides important information on the angle of the shock surface and the line of sight and together with the location of the relics with respect to the X-ray position we can constrain the geometry of the merger axis to within 10 degrees (van Weeren et al., 2011a). Furthermore, the cluster makes an ideal target to study the evolution of radio relics, due to its superior temporal lever arm, with ramifications for the theory of particle acceleration.

---

<sup>1</sup>The spectrum is defined as  $S(/nu) \propto \nu^\alpha$ .

The Musket Ball Cluster is located at  $z = 0.53$  and at this redshift a typical moderate luminosity radio relic has a flux density of 0.3 mJy at  $z = 0.53$  and 1.4 GHz (Nuza et al., 2012; van Weeren et al., 2011a). This is well below both the NRAO VLA Sky Survey (NVSS) and Westerbork Northern Sky Survey (WENNS) sensitivities, thus an existing non-detection in these surveys is not surprising.

We observed the Musket Ball Cluster with the Westerbork Synthesis Radio Telescope (WSRT) in 2013 January 23-28 for a total of 24 hours. We used the standard 21 cm L-band as it is the most sensitive system at the WSRT. The observations have a resolution of about 15x30 arcsec, corresponding to a physical size of 100x200kpc at  $z = 0.53$ , enough to resolve a 1 Mpc relic (relic sizes range between 0.5 and 2 Mpc). With two full synthesis runs we achieved a noise level of  $20 \mu\text{Jy}/\text{beam}$  in the continuum, and about  $10 \mu\text{Jy}/\text{beam}$  in Stokes Q and U. This should enable us to detect a 0.3 mJy relic, covering 5 beam areas, with an SNR of 10.

While there are a number of compact sources associated with the merging cluster (see the  $X$ 's in Figure 2.7), we find no evidence for diffuse radio emission associated with the merging cluster. In other words, no radio halos or relics are detected in the Musket Ball Cluster merger. All previously discovered radio relics have been in clusters with X-ray luminosities in the range of  $10^{44}\text{-}10^{45} \text{ erg s}^{-1}$ . The Musket Ball Cluster has an X-ray luminosity of  $\sim 10^{43} \text{ erg s}^{-1}$  (see Table 2.1). This null detection is in line with the current trend that radio relics are only found in very massive cluster mergers.

## 2.8 Cluster Merger Scenario

The peak of the gas distribution ( $09^{\text{h}}16^{\text{m}}15^{\text{s}} \pm 5.5^{\text{s}}, 29^{\circ}50'59'' \pm 5.0''$ ) derived from X-rays is offset  $1.4' \pm 0.49$  from the North HST WL mass peak ( $09^{\text{h}}16^{\text{m}}10^{\text{s}} \pm 30^{\text{s}}, 29^{\circ}52'10'' \pm 30''$ ), and  $1.4' \pm 0.14$  from the South HST WL mass peak ( $09^{\text{h}}16^{\text{m}}15^{\text{s}} \pm 8.0^{\text{s}}, 29^{\circ}49'34'' \pm 6.9''$ ), and is located near a local minimum in the mass, suggesting that the subclusters have a small im-

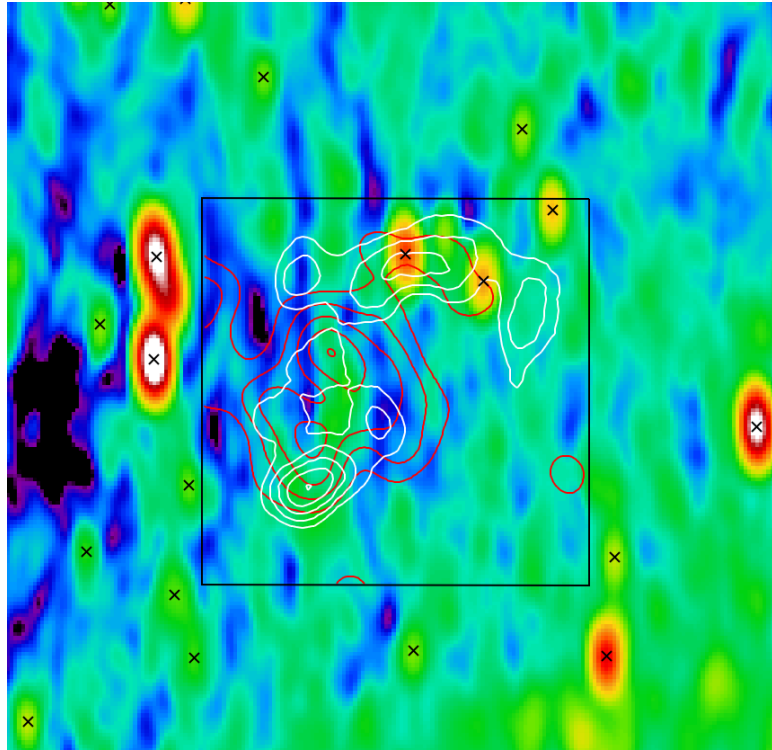


Figure 2.7 Westerbork Synthesis Radio Telescope 21cm L-band image of the Musket Ball Cluster and surrounding area. The color image has an arbitrary log-scale. Likely compact radio sources are denoted by the  $X$  points, and from these the north/south elongated PSF can be seen. The black box shows the area corresponding to Figures 2.1, 4.2, and 4.1. Similarly the white contours are the galaxy number density contours from Figure 4.2, and the red contours are the X-ray contours from Figure 4.1. We detect no significant diffuse radio emission associated with the Musket Ball Cluster (i.e. no radio halos or relics are detected).

pact parameter and have experienced at least their first pass-through along a north-northwest merger direction (see Figure 4.1). Additionally the Central X-ray concentration has a temperature (Table 2.1) in line with an  $M_{500} = 0.9_{-0.3}^{+1.1} \times 10^{14} M_\odot$  potential (Vikhlinin et al., 2009), but the WL data suggests that there is a local under-density of mass at this concentration incapable of supporting such a temperature. Further evidence for the merger scenario is provided by the morphology of the gas. Simulations (Schindler & Mueller, 1993; Poole et al., 2006) predict that the gas morphology elongates transverse to the merger direction after pass-through for mergers with small impact parameters. The Central gas concentration appears to be oblate and roughly perpendicular to the axis connecting the North and South mass peaks. This is consistent with the interpretation that these two subclusters have experienced their first pass-through and that the merger axis being roughly in the plane of the sky.

## 2.9 Discussion

While we use DLSCL J0916.2+2951 to provide further evidence for the canonical DM model and independently constrain  $\sigma_{\text{DM}} m_{\text{DM}}^{-1}$ , we believe that its greatest value is as a probe for a new and special phase of cluster formation. It provides a greatly improved temporal lever-arm with which to guide numerical simulations that explore the major merger phase. This is potentially important given that much of our knowledge of the cluster merger process comes from numerical hydrodynamic simulations (e.g. Poole et al., 2006), which are used to place the tightest constraints on  $\sigma_{\text{DM}} m_{\text{DM}}^{-1}$  ( $< 0.7 \text{ cm}^2 \text{ g}^{-1}$ ; Randall et al., 2008) and bring observed merger velocities (inferred from the observed shock velocity) more in line with the expectations of  $\Lambda$ CDM (Springel & Farrar, 2007; Lee & Komatsu, 2010). Secondly, the large projected separation relative to the virial radii of the subclusters ( $R_{200} \sim 1 \text{ Mpc}$ ) enables the deconvolution of the subclusters from the Central region and direct comparison of the physical properties of each. This will provide new insight into the behavior of the cluster

constituents (gas, galaxies, & DM) during a major merger. For example, it is well established that galaxy clusters play an important role in the evolution of their member galaxies, but it is still unclear whether cluster mergers trigger star formation (e.g. Miller & Owen, 2003; Owen et al., 2005; Ferrari et al., 2005; Hwang & Lee, 2009), quench it (Poggianti et al., 2004), or have no immediate effect (Chung et al., 2010).

Our identification of DLSCL J0916.2+2951 as a dissociative merging system using only optical, WL, and SZE observations shows that these systems can be found independent of X-ray observations. This has implications for finding more of these systems when the existing SZE surveys, e.g. ACT (Hincks et al., 2010) and SPT (Ruhl et al., 2004), are coupled with upcoming and overlapping deep optical/WL surveys, e.g. DES (The Dark Energy Survey Collaboration, 2005) and LSST (Tyson, 2002).

## 2.10 Conclusions

Conclusion text

### **acknowledgements:**

We thank Daniel P. Marrone, Stephen Mchovoj, John E. Carlstrom, and Tony Mroczkowski of the SZA collaboration for sharing the results of the SZA Survey, which helped motivate the detailed follow-up campaign of DLSCL J0916.2+2951. Support for this work was provided by NASA through Chandra Award Number GO1-12171X issued by CXO Center, which is operated by the SAO for and on behalf of NASA under contract NAS8-03060. Support for program number GO-12377 was provided by NASA through a grant from STScI, which is operated by the Association of Universities for Research in Astronomy, Inc., under NASA contract NAS5-26555.

This work made use of the following facilities: CXO (ACIS-I), HST (ACS), Keck:I (LRIS), Keck:2 (DEIMOS), Mayall (MOSAIC 1 & 1.1), Subaru (Suprime-Cam), SZA.

## Chapter 3

# The Dynamics of Merging Clusters: A Monte Carlo Solution Applied to the Bullet and Musket Ball

This chapter was originally published as an article with the same title in the August, 1, 2013 issue of the *Astrophysical Journal Letters* (Volume 772, pp. 131-150).

Merging galaxy clusters have become one of the most important probes of dark matter, providing evidence for dark matter over modified gravity and even constraints on the dark matter self-interaction cross-section. To properly constrain the dark matter cross-section it is necessary to understand the dynamics of the merger, as the inferred cross-section is a function of both the velocity of the collision and the observed time since collision. While the best understanding of merging system dynamics comes from N-body simulations, these are computationally intensive and often explore only a limited volume of the merger phase space allowed by observed parameter uncertainty. Simple analytic models exist but the assumptions of these methods invalidate their results near the collision time, plus error propagation of the highly correlated merger parameters is unfeasible. To address these weaknesses I de-

velop a Monte Carlo method to discern the properties of *dissociative mergers* and propagate the uncertainty of the measured cluster parameters in an accurate and Bayesian manner. I introduce this method, verify it against an existing hydrodynamic N-body simulation, and apply it to two known dissociative mergers: 1ES 0657-558 (Bullet Cluster) and DLSCL J0916.2+2951 (Musket Ball Cluster). I find that this method surpasses existing analytic models — providing accurate (10% level) dynamic parameter and uncertainty estimates throughout the merger history. This coupled with minimal required *a priori* information (subcluster mass, redshift, and projected separation) and relatively fast computation ( $\sim$ 6 CPU hours) makes this method ideal for large samples of dissociative merging clusters.

### 3.1 Introduction

Merging galaxy clusters have become important astrophysical probes providing constraints on the dark matter (DM) self-interaction cross-section ( $\sigma_{\text{DM}}$ ; Markevitch et al., 2004; Randall et al., 2008; Merten et al., 2011; Dawson et al., 2012), and the large-scale matter-antimatter ratio (Steigman, 2008). They are a suspected source of extremely energetic cosmic rays (van Weeren et al., 2010), and the merger event potentially affects the evolution of the cluster galaxies (e.g. Poggianti et al., 2004; Hwang & Lee, 2009; Chung et al., 2009). All of the respective astrophysical conclusions drawn from merging clusters depend on the specific dynamic properties of a given merger.

For example, the subclass of dissociative mergers, in which the collisional cluster gas has become dissociated from the near collisionless galaxies and dark matter, provides four ways of constraining the dark matter self-interaction cross-section (Markevitch et al., 2004; Randall et al., 2008). The best constraints come from studying the mass-to-light ratios ( $M/L$ ) of the subclusters<sup>1</sup>, and the offset between the collisionless galaxies and dark matter (Markevitch et al., 2004; Randall et al., 2008). Both constraints directly depend on the merger dynamics.

---

<sup>1</sup>I define *subcluster* as either one of the two colliding clusters, irrespective of mass, and I define *cluster* as the whole two-subcluster system.

First the relative collision velocity will affect the expected momentum transfer between each subcluster’s dark matter particles which will in turn affect the expected dark matter mass transfer from the smaller subcluster to the larger subcluster ultimately affecting the expected mass to light ratios of the clusters (Markevitch et al., 2004). Second the expected galaxy–dark matter offset will depend on the observed time-since-collision<sup>2</sup> ( $TSC$ ). Initially the offset between the galaxies and dark matter will increase with  $TSC$  (for  $\sigma_{\text{DM}} > 0$ ) as the collisionless galaxies outrun the dark matter that experienced a drag force during the collision, then at later  $TSC$  the offset will decrease due to the gravitational attraction between the galaxies and dark matter halo. Additionally it is important to know the velocity so that dark matter candidates with velocity dependent cross-sections (e.g. Colín et al., 2002; Vogelsberger et al., 2012) can be constrained.

However there is no way to directly observe the dynamic merger parameters of principal interest: the three-dimensional relative velocity ( $v_{3\text{D}}$ ) and separation ( $d_{3\text{D}}$ ) of the subclusters as a function of time, their maximum separation ( $d_{\text{max}}$ ), the period between collisions ( $T$ ), and the time-since-collision ( $TSC$ ). Observations are generally limited to: the subcluster projected separation ( $d_{\text{proj}}$ ), the line-of-sight (LOS) velocity of each subcluster ( $v_i$ ) as inferred from their redshifts, and their mass ( $M_i$ ) or projected surface mass density profile. In addition to the obvious inability to measure a change in the merger state, it is difficult to constrain the dynamic parameters of interest even in the observed state. This is due to the general inability to constrain the angle of the merger axis with respect to the plane of the sky ( $\alpha$ ), see Figure 3.1.

For the Bullet Cluster it was originally thought that estimates of the Mach number of the cluster merger through X-ray observations of the gas shock feature (e.g. Markevitch, 2006) could be used to estimate  $v_{3\text{D}}$ , and in conjunction with measurements of the relative LOS velocities then estimate  $\alpha$ . Similarly, the gas pressure differential across cold front features seen in some merging clusters have also been used to estimate the Mach number of

---

<sup>2</sup>I define the time of collision to be the time of the first pericentric passage.

the cluster merger (e.g. Vikhlinin & Markevitch, 2003). However, Springel & Farrar (2007) showed that the Mach number only translates to an upper limit on  $v_{3D}$ , and in the case of the Bullet Cluster they showed that the Mach inferred velocity could be a factor of  $\sim 2$  larger than the true  $v_{3D}$ . There is potential for constraining  $\alpha$  using polarization measurements of radio relics (Ensslin et al., 1998), which are associated with some cluster mergers (e.g. van Weeren et al., 2010) but not all (e.g. Russell et al., 2011). Even if for some mergers radio relics provide constraints on  $\alpha$ , dynamic models are still needed in order to ascertain the dynamic properties of the merger throughout time.

The two most prevalent methods for ascertaining the dynamics of observed merging systems are *the timing argument* and N-body simulations. The timing argument is based on the solution to the equations of motion of two gravitating point masses, with the cosmological constraint that as  $z \rightarrow \infty$  the separation of the two masses  $d_{3D} \rightarrow 0$  (for an exposition of this method see Peebles, 1993). The timing argument was first used by Kahn & Woltjer (1959) to study the system of the Milky Way and M31, and first applied to binary cluster systems by Beers et al. (1982). It has recently been applied to several dissociative mergers, including the Bullet Cluster (Barrena et al., 2002), Abell 520 (Girardi et al., 2008), Abell 2163 (Bourdin et al., 2011), and Abell 1758N (Boschin et al., 2012). N-body simulations of observed dissociative mergers have been limited to the Bullet Cluster (1ES 0657-558) and have come in two variants: hydrodynamic (Springel & Farrar, 2007; Milosavljević et al., 2007; Mastropietro & Burkert, 2008), and self interacting dark matter (SIDM) plus collisionless galaxy particles (Randall et al., 2008).

While the timing argument method is easy to use, its inherent assumptions result in non-negligible error for dissociative systems. Most importantly the timing argument method assumes two point mass particles; this assumption begins to break down as the two subclusters overlap and results in divergent solutions as the subclusters near collision. Since most dissociative mergers are observed with the two-subcluster halos overlapping and dark matter constraints depend on the merger dynamics near collision, application of the traditional

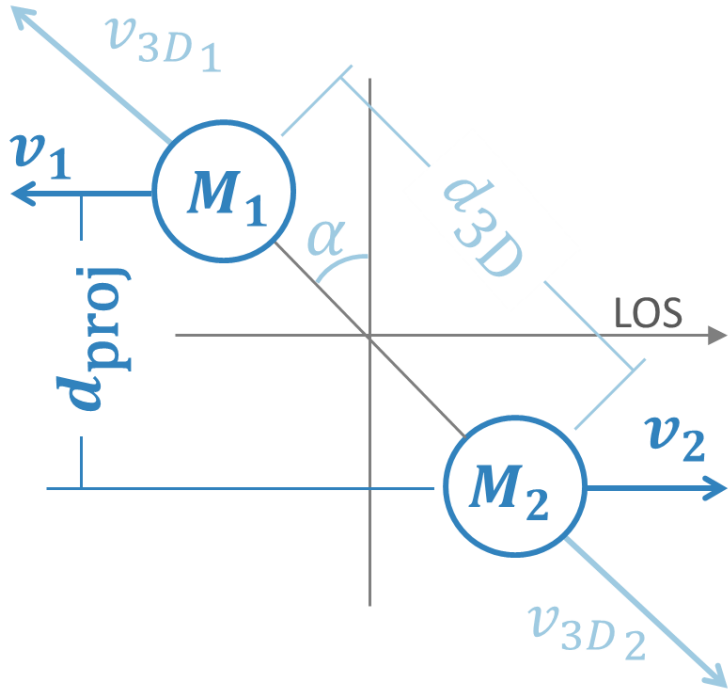


Figure 3.1 The generic two-halo merger configuration assumed in this work. Observable parameters are shown in dark blue, and include the mass of each halo ( $M_i$ ), the projected separation ( $d_{\text{proj}}$ ), and the line of sight (LOS) velocity components ( $v_i$ ) as determined from the halo redshifts. The generally unknown parameters of the mergers are shown in light blue, and include the angle of the merger axis with respect to the plane of the sky ( $\alpha$ ), and the three-dimensional separation ( $d_{3D}$ ) and velocity components ( $v_{3D_i}$ ). Note that while just the outgoing scenario is shown in this figure, the method also considers the incoming scenario.

timing argument to dissociative mergers is limited and should be done with caution. Nusser (2008) addressed this weakness of the traditional timing argument by substituting truncated Navarro, Frenk, & White (1996, hereafter NFW) halos and numerically solving the equations of motion. Another weakness of the timing argument is that its main constraint requires the assumption that the subcluster masses are constant since the beginning of the universe. While Angus & McGaugh (2008) have noted this problem with the initial conditions of N-body simulations and proposed a solution based on estimating the mass accretion histories of the clusters (e.g. Wechsler et al., 2002), their correction is incompatible with the timing argument method as this would add a second differential term to the equations of motion. Finally, the large covariance between the merger parameters plus the complexity of the equations of motion makes propagation of errors in the timing argument formalism untenable. This has resulted in a lack of certainty with timing argument results, leaving most users to run a few scenarios in an effort to roughly bound the range of possible solutions (e.g. Boschin et al., 2012).

N-body simulations provide the most accurate description of merger dynamics, however they are computationally expensive which results in their application being limited. Despite eleven currently confirmed dissociative mergers<sup>3</sup> only the Bullet Cluster has been modeled with N-body simulations, whereas most of these have been analyzed with the timing argument method. Existing N-body simulation strategies to ascertain the dynamic properties of mergers are incapable of keeping up with the current faster than exponential rate of discovery. Even for the case of the Bullet Cluster the N-body analyses have been limited as far as mapping out the merger dynamic phase space allowed by the uncertainty of the observations, with at most 15 different scenarios being run (Mastropietro & Burkert, 2008).

Gómez et al. (2012) have come the closest to addressing this issue in their investigation of

---

<sup>3</sup>(1) Bullet Cluster (Clowe et al., 2004); (2) A520 (Mahdavi et al., 2007); (3) MACS J0025.4-1222 (Bradač et al., 2008); (4) A1240 (Barrena et al., 2009); (5) ZwCL 0008.8+5215 (van Weeren et al., 2011b); (6) A2744 (Merten et al., 2011); (7) A2163 (Okabe et al., 2011); (8) A1758N (Ragozzine et al., 2012); (9) Musket Ball Cluster (Dawson et al., 2012); (10) ACT-CL J01024915 (Menanteau et al., 2012); (11) MACS J0717.5+3745 (Mroczkowski et al., 2012)

potential dissociative mergers (A665 and AS1063) through the use of simplified scale-free numerical simulations of the mergers (see Gómez et al., 2000, for details). However, they have still had to severely limit the phase space probed (fixing merger parameters such as the initial relative velocity and subcluster-subcluster mass ratio); thus admittedly this approach enables construction of plausible models, but not a thorough accounting of possible or likely models.

With these weaknesses in mind I present a new method<sup>4</sup> for analyzing the dynamics of observed dissociative mergers. My primary objectives are to 1) obtain a solution valid near the collision state, 2) fully estimate the covariance matrix for the merger parameters, 3) be able to analyze a dissociative merger on the order of a day using a typical desktop computer, and 4) obtain approximately 10% accuracy; all assuming that only the most general merger observables and their uncertainty are known: mass of each subcluster, redshift of each subcluster, and projected separation of the subclusters.

In §3.2 I define a method for analyzing the dynamics of observed dissociative mergers. In §3.2.3 I verify this method with existing results from a hydrodynamic N-body simulation. In §3.3 I apply this method to the Bullet Cluster and in §3.4 I apply this method to the Musket Ball Cluster (DLSCL J0916.2+2951) and contrast its dynamics with those of the Bullet Cluster. Finally in §3.5 I summarize my findings, discuss their implications for the constraints on dark matter and suggest other science that will benefit from the introduced method. Throughout this paper I assume  $\Omega_\Lambda = 0.7$ ,  $\Omega_m = 0.3$ , and  $H = 70 \text{ km s}^{-1} \text{ Mpc}^{-1}$ .

## 3.2 Method

In order to obtain a valid solution of the system dynamics near the collision state I use a model of two spherically symmetric NFW halos, rather than point masses. I incorporate this model in a standard Monte Carlo implementation: draw randomly from the observables'

---

<sup>4</sup>This method is similar to the one used by Dawson et al. (2012), although with several improvements (see §3.4).

probability density functions (PDF’s) to generate a possible realization of the merger, use the model to calculate merger properties of interest, apply multiple priors, store these likelihood weighted results as a representative random draw of their PDF, and repeat. The final result is a multidimensional PDF for the dynamic parameters of the merger. This method agrees well with hydrodynamic simulations, §3.2.3, and satisfies the speed and accuracy objectives outlined in the Introduction.

### 3.2.1 Model

The general basis of the model is a collisionless two body system with the mass of each body mutually conserved throughout the merger. The model requires minimal input: the mass of each subcluster, the redshift of each subcluster, and the projected separation of the subclusters (along with associated uncertainties). It assumes conservation of energy and zero angular momentum. The model also assumes that the maximum relative velocity of the two bodies is the free-fall velocity of the system assuming their observed mass. In the remainder of this subsection I will discuss in detail these general assumptions, their justification, and their implications.

I model the system using two spherically symmetric NFW halos truncated at  $r_{200}$ <sup>5</sup>. By default the concentration of each halo is determined by the halo’s mass via the mass-concentration scaling relation of Duffy et al. (2008). This is not a requirement of the model though, and measured concentrations can be used, as in the case of §3.3.1. The dynamic parameter results are relatively insensitive to the assumed concentration of the subclusters. Take for example the case of §3.2.3 with user specified concentrations of  $c_1 = 1.94$  and  $c_2 = 7.12$ : if instead Duffy et al. (2008) inferred concentrations  $c_1 = 3.44$  and  $c_2 = 2.75$  ( $\sim 200\%$  difference for both) are used, the difference in the estimated  $v_{3D}(t_{\text{col}})$  and  $TSC$  are both less than 6%.

The model assumes that the mass of each subcluster is constant and equal to the observed

---

<sup>5</sup> $r_{200}$  is defined as the radius of the spherical region within which the average density is 200 times the critical density at the respective redshift.

mass<sup>6</sup>. While this assumption is also used in the timing argument method, it is more reasonable for this method since the bulk of the results are calculated between the observed state and the collision state, typically lasting  $\lesssim 1$  Gyr. This is about an order of magnitude shorter than the typical timescales of the timing argument method thus the new method is less susceptible to error due to neglecting growth of structure.

The model assumes that the energy of the two-halo system is conserved, and consists only of their mutual kinetic and potential energies. The kinetic energy of the system is  $K(t) = 0.5\mu v_{3D}(t)^2$ , where  $\mu$  is the reduced mass of the system and  $v_{3D}(t)$  is the relative physical velocity of the two subclusters at time  $t$ . The potential energy of the system is assumed to be purely gravitational and is derived in Appendix A.1. Since the model assumes zero impact parameter there is no rotational kinetic energy term. Mastropietro & Burkert (2008) find that a moderate impact parameter of  $\sim 0.1r_{200}$  has less than a 1% effect on the merger velocity, thus this assumption should have negligible effect for the case of dissociative mergers which must have had relatively small impact parameters in order to dissociate the bulk of their gas.

For the relative velocity of the two subclusters I apply a flat prior from zero to the free-fall velocity of the subclusters, assuming their observed mass. This will result in an overestimate of the maximum possible relative velocity, due to the neglect of mass accretion. It is conceivable that this prior could be tightened using the maximum relative velocities observed in cosmological N-body simulations as a function of subcluster masses and redshift. Another possibility for tightening the prior would be to analytically estimate the free-fall velocity accounting for mass accretion (e.g. Angus & McGaugh, 2008). An advantage of the Monte Carlo approach taken with this method is that additional priors can be applied as more knowledge becomes available without the need to rerun the analysis, so I opt for a conservative default approach.

The model ignores the effects of surrounding large scale structure and simply treats the

---

<sup>6</sup>For subcluster mass I refer to  $M_{200}$ , which is the mass of the individual subcluster enclosed within a radius of  $r_{200}$ .

two-body system. As Nusser (2008) shows, a global overdense region (10 times denser than the background) engulfing the system only affects the dynamics substantially for extreme collision velocities ( $\sim 4500 \text{ km s}^{-1}$ ). While global overdensities may be disregarded it is not clear that the effects of nearby structures can be disregarded, e.g. as in the case three body systems. Thus this method should be applied with caution to complex cluster mergers.

The model also ignores dynamical friction. Farrar & Rosen (2007) found that including dynamical friction accounted for an  $\sim 10\%$  reduction in the inferred collision velocity of the Bullet Cluster in their analytic treatment. This is potentially concerning since dynamical friction is inversely proportional to the relative velocity of the merger, thus it may become even more important for mergers slower than the Bullet Cluster. However in §3.2.3 I compare the results of my method with those from a hydrodynamic N-body simulation and show that the net effect of all simplifications (including ignoring dynamical friction, tidal stripping of mass and gas mass lost during the collision) are negligible, suggesting that dynamic friction is less important than the analytic estimates of Farrar & Rosen (2007) suggest.

### 3.2.2 Monte Carlo Analysis

In this section I discuss the details of the Monte Carlo analysis workflow. I chose to implement a Monte Carlo analysis because the high degree of correlation among the many merger dynamic parameters made traditional propagation of errors unfeasible. A Monte Carlo analysis has the added advantage of easily enabling application of different combinations of priors *ex post facto*, see e.g. §3.3.2.2.

The analysis begins by randomly drawing from the PDF's of the merger observables: mass of each subcluster ( $M_{200_i}$ ), redshift of each subcluster ( $z_i$ ), and projected separation of the subclusters ( $d_{\text{proj}}$ ). The potential energy,  $V$  (see Appendix A.1), at the time of the collision is used to calculate the maximum relative velocity,

$$v_{3D_{\max}} = \sqrt{-\frac{2}{\mu}V(r=0)}.$$

The velocity of each subcluster relative to us is estimated from its redshift,

$$v_i = \left[ \frac{(1+z_i)^2 - 1}{(1+z_i)^2 + 1} \right] c,$$

where  $c$  is the speed of light. The relative radial velocity of the subclusters is calculated from their redshifts,

$$v_{\text{rad}}(t_{\text{obs}}) = \frac{|v_2 - v_1|}{1 - \frac{v_1 v_2}{c^2}}.$$

Since the angle of the merger axis with respect to the plane of the sky,  $\alpha$ , is unconstrained without prior knowledge of the three-dimensional relative velocity, I assume that all merger directions are equally probable. However, projection effects result in  $PDF(\alpha) = \cos(\alpha)$ . Due to symmetry it is only necessary to analyze the range  $0 \leq \alpha \leq 90$  degrees. I draw randomly from this PDF for each realization. This enables the calculation of the three-dimensional relative velocity in the observed state,

$$v_{3D}(t_{\text{obs}}) = v_{\text{rad}}(t_{\text{obs}})/\sin(\alpha), \quad (3.1)$$

as well as the observed three-dimensional separation of the subclusters,

$$d_{3D}(t_{\text{obs}}) = d_{\text{proj}}/\cos(\alpha). \quad (3.2)$$

If  $v_{3D}(t_{\text{obs}}) > v_{3D_{\text{max}}}$ , then this realization of the merger is discarded; otherwise the relative collision velocity is calculated,

$$v_{3D}(t_{\text{col}}) = \sqrt{v_{3D}(t_{\text{obs}})^2 + \frac{2}{\mu} [V(t_{\text{obs}}) - V(t_{\text{col}})]}. \quad (3.3)$$

Similarly if  $v_{3D}(t_{\text{col}}) > v_{3D_{\text{max}}}$ , then this realization is discarded.

The change in time,  $\Delta t$ , between two separations is given by

$$\Delta t = \int_{r_1}^{r_2} \frac{dr}{\sqrt{\frac{2}{\mu}(E - V(r))}}. \quad (3.4)$$

I define the time-since-collision ( $TSC$ ) as the time it takes the subclusters to traverse from zero separation to their physical separation in the observed state,  $d_{3D}$ . Because there is a potential degeneracy in whether the subclusters are “outgoing” (approaching the apoapsis after collision) or “incoming” (on a return trajectory after colliding and reaching the apoapsis); I solve for both of these cases,  $TSC_0$  and  $TSC_1$  respectively. In determining  $TSC_1$  it is useful to define the period,  $T$ , of the system. I define  $T$  to be the time between collisions,

$$T = 2 \int_0^{d_{\max}} \frac{dr}{\sqrt{\frac{2}{\mu}(E - V(r))}},$$

where  $d_{\max}$  is the distance from zero separation to the apoapsis, when  $E = V$ . Thus,

$$TSC_1 = T - TSC_0.$$

During the Monte Carlo analysis any realizations with  $TSC_0$  greater than the age of the Universe at the cluster redshift are discarded. A similar flat prior is applied when calculating the statistics of  $TSC_1$ . To this regard some insight into the likelihood of the system being in an “outgoing” or “incoming” state can be gained by calculating the fraction of realizations with  $TSC_1$  less than the age of the Universe at the cluster redshift. Conceivably these temporal priors could be strengthened, requiring that the time to first collision ( $T$ ) plus the respective  $TSC$  be less than the age of the Universe at the cluster redshift, in a fashion similar to the timing argument. However, as with the timing argument model, the model of §3.2.1 becomes less valid over time-scales approaching the age of the Universe. Thus I use the more conservative prior by default.

Since the majority of the merger time is spent at large separations, due to lower relative

velocities, observations of the system are more likely near apoapsis than near the collision. Thus the probability of each realization is convolved with the prior

$$\text{PDF}(TSC_0) = 2 \frac{TSC_0}{T}. \quad (3.5)$$

There are likely selection effects which complicate this PDF, since it can be imagined that the X-ray luminosity is greatest near the time of the collision (see e.g. Randall et al., 2002). However this information is rarely if ever known, thus it is not included by default. In §3.3.2.2 I show how additional temporal priors, based on similar effects, may be effectively applied to the results of the analysis ex post facto.

The end result of this method is a 13 dimensional posterior PDF of an array of cluster merger parameters, see for example Appendix A.3. Finally to compact the results I use the biweight-statistic (generally more robust and less sensitive to abnormally tailed distributions than the median or mean) and bias-corrected percent confidence limits (Beers et al., 1990) applied to the marginalized parameter distributions of the valid realizations, see for example Table 3.2.

### 3.2.3 Comparison with Hydrodynamic Simulations

For the purposes of checking the physical assumptions of the model I reanalyze the Springel & Farrar (2007) model of the Bullet Cluster, comparing my dynamic parameter estimates with their hydrodynamic N-body simulation based estimates. For this analysis I run just their single case through the model (i.e. I do not perform a Monte Carlo analysis). They represent the “main” and “bullet” subclusters as NFW halos with  $M_{200_1} = 1.5 \times 10^{15} M_\odot$ ,  $c_1 = 1.94$ ,  $M_{200_2} = 1.5 \times 10^{14} M_\odot$ , and  $c_2 = 7.12$ , respectively. They note that the gas properties of their simulation most closely match the observed Bullet Cluster gas properties for the time step corresponding to a subcluster separation of  $d_{3D} = 625$  kpc and relative velocity of  $v_{3D}(t_{\text{obs}}) = 2630 \text{ km s}^{-1}$ . I define this as the “observed” state (dashed line in Figure 3.2) and

use the model discussed in §3.2.1 to extrapolate values of the relative subcluster velocities ( $v_{3D}$ ) and time-since-observed state (TSO) before and after the observed state (left and right of the dashed line in Figure 3.2, respectively). The Springel & Farrar (2007) simulation results (black circles) for these parameters are read directly from their Figure 4.

I compare the model results (blue boxes) with the Springel & Farrar (2007) simulation results, and assume their results as truth when calculating the percent error, see Figure 3.2. There is better than 4% agreement between  $v_{3D}$  and 14% agreement between the TSO. While the model results are biased, the bias appears stable and is roughly an order of magnitude smaller than the typical random error in the parameter estimates (see for example Table 3.2). Given the stability of the bias it is conceivable that it could be corrected in the model results. However, to have any confidence in this bias correction the model results should be compared with a range of merger scenarios, which is beyond the scope of this current work. Note that the better agreement between the velocity estimates than between the TSO estimates is to be expected since the velocity calculation (essentially Equation 3.3) comes from simply comparing the observed and another state of the merger whereas the TSO calculation (Equation 3.4) requires integration between these two states. The results of this comparative study essentially validate many of the simplifying assumptions of the model (conservation of energy, and ignoring the affects of dynamical friction, tidal stripping of dark matter and gas during the collision).

As an aside it should be noted that for this comparison I use the Springel & Farrar (2007) NFW halo parameters that represent the state of the halos prior to collision. Ideally I should use the NFW parameters representative of the state of the halos at  $t_{\text{obs}}$ , however these properties were not reported in their paper. From Figure 5 of Springel & Farrar (2007) some insight into the time variability of the halo parameters can be gained. Since the depth each halo's gravitational potential at  $\sim r_{200}$  does not change appreciably throughout the merger, it can be inferred that  $M_{200}$  of each halo does not change. However, the gravitational potential near the center of each halo deepens by  $\sim 25\%$  during and after the collision. This can be

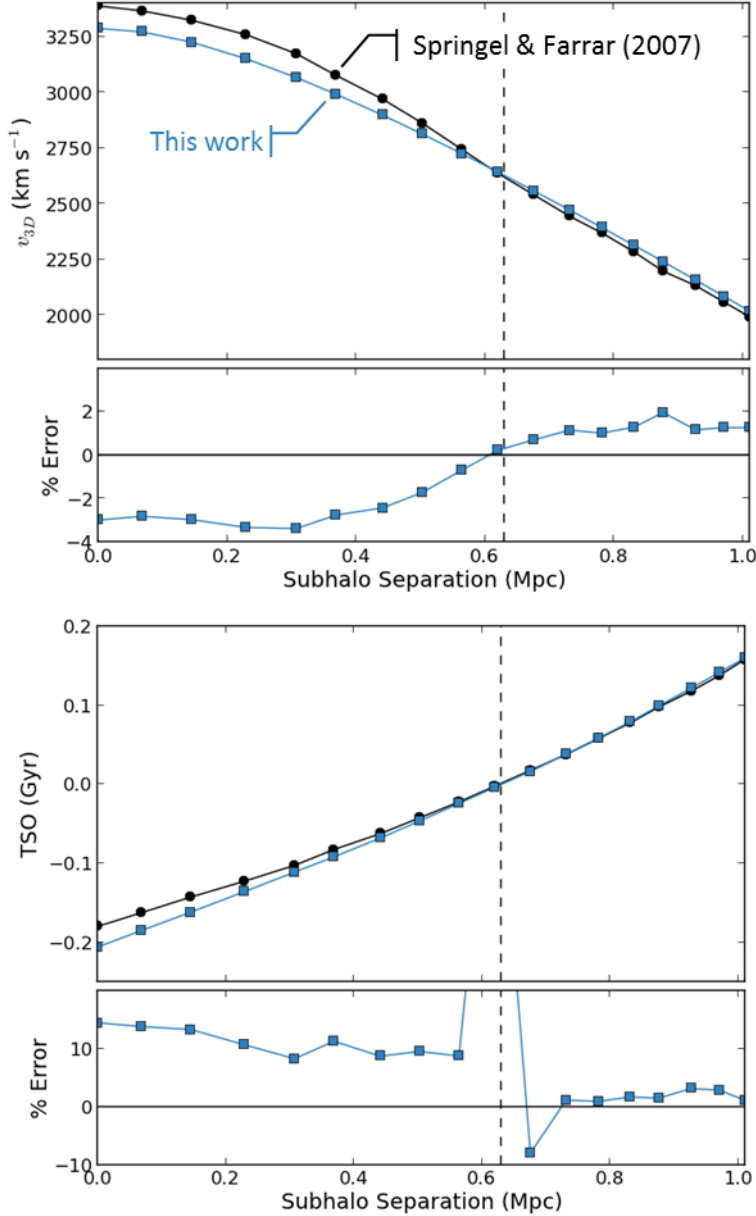


Figure 3.2 Comparison of the model results (blue boxes) with the hydrodynamic simulation results of Springel & Farrar (2007) for the Bullet Cluster. The top figure is a comparison of the velocity of the “bullet” relative to the “main” subcluster, with the subhalo separation (i.e. the three-dimensional separation of the “main” and “bullet” subclusters) as the independent variable. The bottom figure is a comparison of the time-since-observed state (TSO), where the “observed” state (dashed line) is defined by Springel & Farrar (2007) as the time step in their simulation when the gas properties most closely match the observed Bullet Cluster gas properties. Times prior(post) to the observed state have negative(positive) values. The percent error in each case is calculated assuming the Springel & Farrar (2007) results as truth. While the model results are biased, the bias appears stable and is roughly an order of magnitude smaller than the typical random error in the parameter estimates (see for example Table 3.2). Note that the TSO percent error calculation understandably diverges near the arbitrary choice of time equal zero. The Springel & Farrar (2007) results are read directly from their Figure 4.

interpreted as the concentration of each halo increasing. Thus for the comparison of my model with the Springel & Farrar (2007) hydrodynamic simulation to be more appropriate I should have used halos with larger concentrations. Doing so actually brings my model results more in-line with the simulation results. If for example I increase the concentration of the “bullet” halo from 1.94 to 3 and the concentration of the “main” halo from 7.12 to 8, then the percent error for the relative velocity of the halos reduces to  $\lesssim 1\%$  and the percent error for the TSO reduces to  $\sim 10\%$ . Thus the comparative results of Figure 3.2 should be considered conservative with respect to the variability of the halo properties throughout the merger.

### 3.3 Bullet Cluster Dynamics

The Bullet Cluster is the prime candidate for first application of the method as it is one of the best studied dissociative mergers. It has a wealth of observational data necessary for input to the model, as discussed in §3.3.1, plus supplementary data which enables additional posterior priors, as discussed in §3.3.2.2.

#### 3.3.1 Bullet Cluster Observed System Properties

I summarize the observed Bullet Cluster parameters used as input to my analysis in Table 3.1. The full PDF’s of these input parameters have not been published so I simply assume Gaussian distributions. I refer to the main subcluster as halo 1 and the “bullet” subcluster as halo 2. For the mass and concentration of each subcluster I use the most recently reported estimates from Springel & Farrar (2007), based upon strong and weak lensing estimates (Bradač et al., 2006). However, they do not present errors for these quantities so for the mass I estimate the  $1-\sigma$  errors to be 10% of the mass, since this is approximately the magnitude of the error reported by Bradač et al. (2006) for  $M(< 250 \text{ kpc})$ . There is no published estimate for the uncertainty of the concentrations of the NFW model fits,  $c_i$ , so I

Table 3.1. Bullet Cluster parameter input

Parameter	Units	$\mu$	$\sigma$	Ref.
$M_{200_1}$	$10^{14} M_\odot$	15	1.5 <sup>a</sup>	1
$c_1$		7.2	... <sup>b</sup>	1
$M_{200_2}$	$10^{14} M_\odot$	1.5	0.15 <sup>a</sup>	1
$c_2$		2.0	... <sup>b</sup>	1
$z_1$		0.29560	0.00023	2
$z_2$		0.29826	0.00014	2
$d_{\text{proj}}$	kpc	720	25	3

Note. — A Gaussian distribution with mean,  $\mu$ , and standard deviation,  $\sigma$ , is assumed for all parameters with quoted respective values. The mass,  $M_{200}$ , and concentration,  $c$ , are the defining properties of assumed spherically symmetric NFW halos.

<sup>a</sup>Estimated to be 10%, based one the error magnitude of  $M(< 250 \text{ kpc})$  reported in Bradač et al. (2006).

<sup>b</sup>No errors were presented in the reference. A single concentration value was used for all Monte Carlo realizations.

References. — (1) Springel & Farrar 2007; (2) Barrena et al. 2002; (3) Bradač et al. 2006.

simply assume the concentrations to be known quantities (as noted in §3.2.1 the results are relatively insensitive to the assumed concentrations). The redshifts of the main and “bullet” subclusters are estimated from 71 and 7 spectroscopic members, respectively (Barrena et al., 2002). The projected separation of the mass peaks is determined from strong and weak lensing measurements (Bradač et al., 2006), and is essentially the same as the separation of the subclusters’ galaxy centroids. For each Monte Carlo realization individual values are drawn randomly from each of these assumed Gaussian distributions.

### 3.3.2 Bullet Cluster System Dynamics Results

I first analyze the Bullet Cluster with the Monte Carlo analysis method and default priors discussed in §3.2, highlighting the complexity of merger dynamics and the inappropriateness of analyzing a small sample of select merger scenarios. In §3.3.2.2 I incorporate additional constraints provided by the observed strong X-ray shock front plus boosted temperature and luminosity. I discuss this prior information and apply it ex post facto to the default prior results of §3.3.2.1.

I perform the analysis with 2,000,000 Monte Carlo realizations. Parameter estimates converge to better than a fraction of a percent with only 20,000 realizations ( $\sim 6$  CPU hours). I run a factor of a hundred more since it was computationally inexpensive and it provides a data sample to which I can apply any number of conceivable posterior PDF's and still maintain sub-percent statistical accuracy.

#### 3.3.2.1 Default Priors

The main results of this analysis are that: 1) there is a great degree of covariance between the geometry, velocity, and time parameters of the merger, and 2) models of the system which disregard the uncertainty of  $\alpha$  will catastrophically fail to capture the true uncertainty in the dynamic parameters.

The two-dimensional PDF of Figure 3.3 exemplifies the complexity of the covariance between the various merger parameters<sup>7</sup>. The shape of the PDF is most easily understood in terms of the parameters' dependence on  $\alpha$ . This dependence is illustrated by the green-scale triangles that represent a subsample of the Monte Carlo population, which jointly satisfies the requirement of being drawn from  $\pm 0.13\sigma$  of the mean of each of the input parameters, i.e. the “most likely” values for the input parameters. The saturation of the triangles increases with increasing  $\alpha$ , from 10–86 degrees, clearly showing a monotonically increasing

---

<sup>7</sup>Similar degrees of complex covariance exist for the other geometry, velocity and time parameters, see e.g. the results array in Appendix A.3.

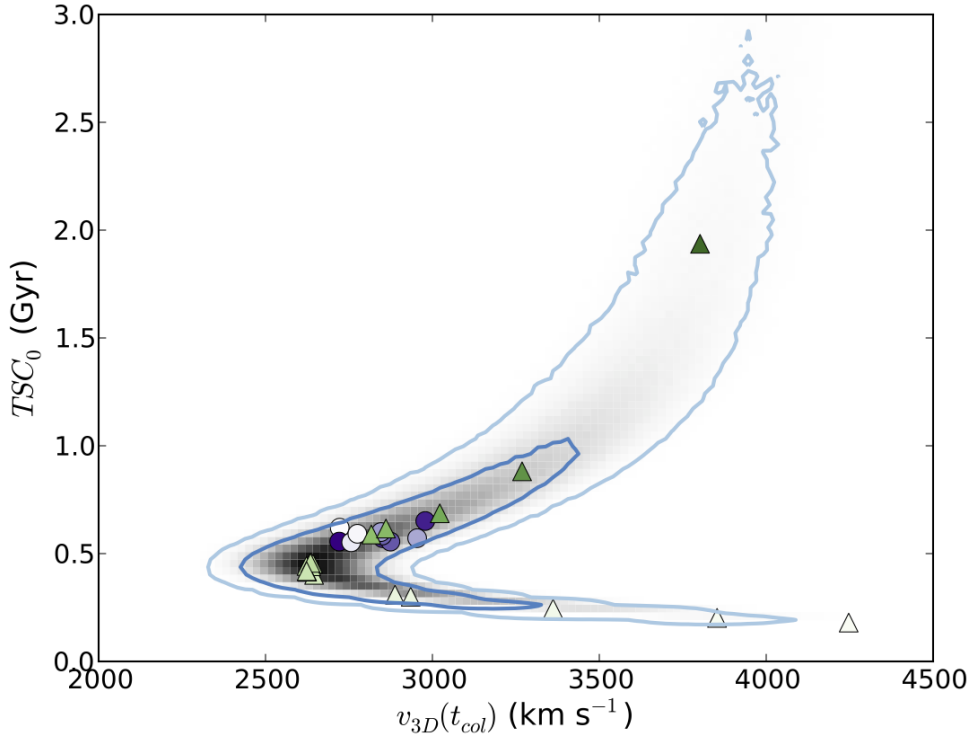


Figure 3.3 The posterior of the Bullet Cluster’s time-since-collision  $TSC_0$  and  $v_{3D}(t_{col})$  parameters is shown in grayscale with dark and light blue contours representing 68% and 95% confidence, respectively. The green-scale triangles are from a subsample of the Monte Carlo population, which jointly satisfies the requirement of being drawn from  $\pm 0.01\sigma$  of the mean of each of the input parameters, i.e. the “most likely” values for the input parameters. Despite representing the most probable input parameter values there is considerable spread in the inferred output parameters, with the subsample clearly tracing the ridge of the distribution. The saturation of the triangles increases with increasing  $\alpha$ , from 10–86 degrees. The purple-scale circles are from a subsample near the bi-weight location of  $\alpha = 50 \pm 0.0002$  degrees, with the saturation of the circles increasing with increasing  $M_{200_1}$ . While the length of the distribution is predominantly caused by uncertainty in  $\alpha$  the width is predominantly caused by uncertainty in the input parameters. Despite the Bullet Cluster being one of the best measured dissociative mergers there is still considerable and complex uncertainty in its merger parameters, predominantly due to uncertainty in  $\alpha$ .

relationship with  $TSC_0$  (see also Figure A.6). For small  $\alpha$  (light green triangles), Equation 3.1 states that  $v_{3D}(t_{obs})$  must be large thus  $v_{3D}(t_{col})$  must also be large, and since Equation 3.2 states that  $d_{3D}(t_{obs})$  approaches the minimum possible observed separation,  $d_{proj}$ , the  $TSC_0$  must approach a minimum. Conversely for large  $\alpha$  (dark green triangles),  $d_{3D}(t_{obs})$  becomes large increasing the time required to reach the observed state, and despite  $v_{3D}(t_{obs})$  approaching the minimum  $v_{rad}(t_{obs})$  the collision velocity must increase for the subclusters to have been able to reach the larger  $d_{3D}(t_{obs})$ .

The bulk of the uncertainty in the geometry, velocity and time parameters is due to the uncertainty of  $\alpha$ . This is exemplified by the fact that the green-scale triangles in Figure 3.3 closely trace the extent of the ridge line of the two-dimensional distribution (i.e. span the bulk of the uncertainty). Conversely the “width” of the distribution is predominantly due to uncertainty in the input parameters. This is exemplified by the purple circles of Figure 3.3, which are for a near constant  $\alpha$  yet randomly sample the  $M_{200_1}$  distribution. The saturation of the circles increase with increasing mass.

The inability to directly measure  $\alpha$ , coupled with its strong degree of correlation with the other dynamic parameters, makes it the dominant source of uncertainty. While it was originally believed that the three-dimensional merger velocity as inferred from the X-ray shock feature could be coupled with the redshift determined radial velocity to measure  $\alpha$ , Springel & Farrar (2007) showed that the X-ray shock inferred velocity significantly overestimates the true three-dimensional merger velocity. So at best this information can weakly constrain  $\alpha$ , and in the case of the Bullet Cluster the X-ray shock inferred velocity is significantly greater than the free-fall velocity,  $v_{3D_{max}}$ , thus it provides no additional constraining power. In §3.5.1 I discuss how the results of this method can be used in conjunction with N-body simulations to limit the computational impact of accounting for the uncertainty in  $\alpha$ .

Table 3.2. Bullet Cluster parameter estimates

Parameter	Units	Location <sup>a</sup>	Default Priors			Default + Added Temporal Priors		
			68% LCL-UCL <sup>b</sup>	95% LCL-UCL <sup>b</sup>	Location <sup>a</sup>	68% LCL-UCL <sup>b</sup>	95% LCL-UCL <sup>b</sup>	Location <sup>a</sup>
$M_{200_1}$	$10^{14} M_\odot$	15.0	13.5 – 16.6	12.1 – 18.1	15.2	13.6 – 16.6	12.2 – 18.1	
$M_{200_2}$	$10^{14} M_\odot$	1.5	1.4 – 1.6	1.2 – 1.8	1.5	1.4 – 1.7	1.2 – 1.8	
$z_1$		0.2956	0.2954 – 0.2958	0.2951 – 0.2961	0.2956	0.2954 – 0.2958	0.2951 – 0.2961	
$z_2$		0.2983	0.2981 – 0.2984	0.2980 – 0.2985	0.2983	0.2981 – 0.2984	0.2980 – 0.2985	
$d_{\text{proj}}$	Mpc	0.72	0.69 – 0.76	0.65 – 0.80	0.72	0.68 – 0.75	0.64 – 0.79	
$\alpha$	degree	50	27 – 73	15 – 84	24	16 – 38	11 – 53	
$d_{3D}$	Mpc	1.1	0.8 – 2.6	0.7 – 7.1	0.8	0.7 – 0.9	0.7 – 1.2	
$d_{\max}$	Mpc	1.3	1.1 – 2.5	1.0 – 6.4	1.2	1.0 – 1.7	1.0 – 3.1	
$v_{3D}(t_{\text{obs}})$	$\text{km s}^{-1}$	820	640 – 1500	550 – 2500	1600	1100 – 2500	790 – 3200	
$v_{3D}(t_{\text{col}})$	$\text{km s}^{-1}$	3000	2700 – 3800	2500 – 4200	2800	2600 – 3300	2500 – 3800	
$TSC_0$	Gyr	0.6	0.3 – 1.1	0.2 – 3.9	0.4	0.3 – 0.5	0.2 – 0.6	
$TSC_1^c$	Gyr	1.2	1.0 – 2.4	0.9 – 8.2	1.3	1.0 – 2.0	0.9 – 4.6	
$T$	Gyr	1.8	1.5 – 3.2	1.4 – 8.1	1.6	1.4 – 2.3	1.3 – 4.8	

<sup>a</sup>Biweight-statistic location (see e.g. Beers et al., 1990).

<sup>b</sup>Bias-corrected lower and upper confidence limits, LCL and UCL respectively (see e.g. Beers et al., 1990).

<sup>c</sup>For the case of the Default + Added Temporal Prior, none of the realizations have a valid  $TSC_1$ , meaning that the Bullet Cluster is being observed in the “outgoing” state, as discussed in §3.3.2.2.

### 3.3.2.2 Added Temporal Prior

One of the advantages of this Monte Carlo method is that additional constraints are easily incorporated ex post facto. An example of such constraints in the case of the Bullet Cluster is the observed X-ray shock front and factor of 2.4 greater X-ray estimated mass to lensing estimated mass (Markevitch, 2006), due to merger related X-ray temperature and luminosity boost. Hydrodynamic simulations of merging clusters (e.g. Ricker & Sarazin, 2001; Randall et al., 2002) suggest that such transient effects last of order the X-ray sound crossing time. Since simulations show negligible difference between the time scales of the two I chose to construct a prior based on the observed temperature boost. Randall et al. (2002) find that the full-width-half-max (FWHM) duration of the temperature boost is  $\sim 0.4t_{\text{sc}}$  with the entire boost duration being  $\sim 1.4t_{\text{sc}}$ , where  $t_{\text{sc}}$  is the sound crossing time of the more massive of the two subclusters. The peak of this boost roughly coincides with the time of the *collision*, as defined in §3.1. Given the  $M_{200_1} = 15 \times 10^{14} M_\odot$  and temperature  $T_X = 14 \text{ keV}$  of the “main” subcluster (Markevitch, 2006), the  $t_{\text{sc}} = 1 \text{ Gyr}$ . I construct a sigmoid function for the  $TSC$  prior PDF based on the observed temperature boost,

$$\text{PDF}(TSC) = \frac{1}{2} \left[ 1 - \tanh \left( \frac{TSC - 0.5a}{0.25b} \right) \right],$$

where  $a$  is the FWHM of the duration of the temperature boost and  $b$  is the entire boost duration. I chose a sigmoid function over a simple step function since the temperature boost predicted by Randall et al. (2002) does not end abruptly. This prior is coupled with the previously discussed  $TSC$  prior (Equation 3.5).

Application of this prior significantly improves the uncertainty in  $TSC_0$  (180% to 67%) and  $v_{3D}(t_{\text{col}})$  (28% to 19%), compare Figure 3.3 with Figure 3.4. It essentially removes the possibility of a  $TSC > 0.6 \text{ Gyr}$ . As expected from the  $\alpha$  dependence shown by the green triangles in Figure 3.3 this prior also reduces the likelihood of  $\alpha \gtrsim 50$  degrees, which in turn affects both the location and uncertainty of  $d_{3D}$  and  $v_{3D}(t_{\text{obs}})$ , see Table 3.2. The remaining

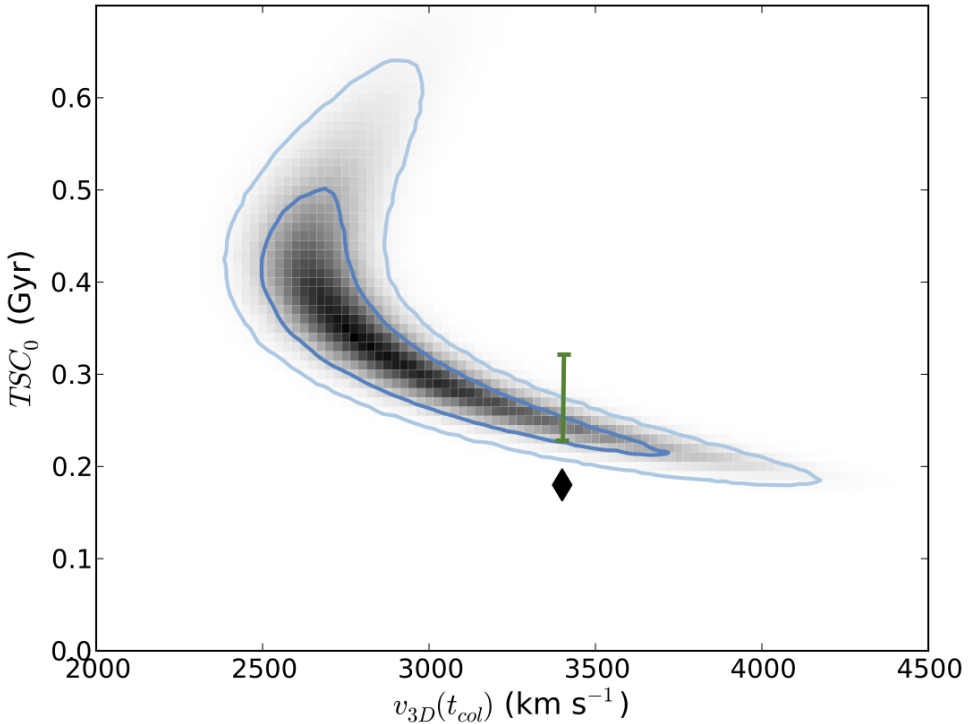


Figure 3.4 The posterior of the Bullet Cluster’s  $TSC_0$  and  $v_{3D}(t_{\text{col}})$  parameters after application of an additional temporal prior based on X-ray observations of the Bullet Cluster (grayscale). Dark and light blue contours representing 68% and 95% confidence, respectively. The added temporal prior significantly improves the constraint on the merger parameters (compare with Figure 3.3). The black diamond represents the Springel & Farrar (2007) hydrodynamic simulation result for their defined “observed state”, whose X-ray properties best match the observed X-ray properties;  $d_{3D}=625$  kpc for this state. The green bar shows their result for  $d_{3D}$  between 700 to 900 kpc, which is more in line with the observed  $d_{\text{proj}} = 720 \pm 25$  kpc (assuming  $0 < \alpha < 35$  degrees).

parameter estimates are predominantly unaffected by the prior, with only a few having their confidence limits affected as the result of their high end low probability tails being down weighted. Additionally there is now essentially zero probability that the bullet subcluster has reached the apoapsis and is on a return trajectory, since the 95% lower confidence limit of  $TSC_1$  is 0.9 Gyr (see Table 3.2) and the prior essentially removes the possibility of a  $TSC > 0.6$  Gyr. I present the full results array, which includes the default analysis prior combined with this temperature boost prior, in Appendix A.3 and the compact parameter estimates in Table 3.2.

According to this analysis the Springel & Farrar (2007) results stated in §3.2.3 seem unlikely (see the black diamond of Figure 3.4), however this is simply due to their definition of the “observed state”. They define the observed state to be when their simulated X-ray properties most closely match the observed X-ray properties, yet the separation of the halos in this state is only  $d_{3D} = 625$  kpc; this is less than the observed  $d_{\text{proj}} = 720 \pm 25$  kpc (Bradač et al., 2006). If we instead consider their estimate of  $TSC_0$  for  $d_{3D}$  between 700 to 900 kpc (corresponding to  $d_{\text{proj}} = 700$  and  $0 < \alpha < 35$  degrees), then  $0.24 < TSC_0 < 0.33$  Gyr (see green bar of Figure 3.4). This brings their result in line with the results of this method, as expected by the agreement presented in §3.2.3. Note that the general conclusion of Springel & Farrar (2007), that the shock speed greatly overestimates the actual relative speed of the subclusters, remains valid regardless of which “observed state” is used.

## 3.4 Musket Ball Cluster Dynamics

I also apply the method to the Musket Ball Cluster, with the objective of updating an existing analysis and comparing this system with the Bullet Cluster. A preliminary analysis of the system dynamics using a similar method (Dawson et al., 2012) suggested that the Musket Ball Cluster merger is  $\sim 3\text{--}5$  times further progressed than other confirmed dissociative mergers. However, that analysis treated the two merging subclusters as uniform density spheres and

also failed to account for the temporal phase-space PDF (Equation 3.5). Additionally the claim that the Musket Ball Cluster is both slower and further progressed than the Bullet Cluster was based on comparing the Musket Ball’s  $TSC_0 - v_{3D}(t_{\text{col}})$  PDF with that of the single point Springel & Farrar (2007) estimate. As noted in §3.3.2.1 there is a large area of parameter space that the Springel & Farrar (2007) result fails to represent.

Similar to my analysis of the Bullet Cluster I perform the analysis with 2,000,000 Monte Carlo realizations. Parameter estimates converge to better than a fraction of a percent with only 20,000 realizations.

### 3.4.1 Musket Ball Observed System Properties

I show the observed Musket Ball Cluster parameter PDF’s in Figures 3.5–3.7, each the result of analyses presented by Dawson et al. (2012). I refer to their “south” subcluster as halo 1 and “north” subcluster as halo 2. The mass PDF’s, Figure 3.5, are the result of an MCMC analysis where NFW halos were simultaneously fit to the weak lensing signal. The relative velocity distributions, Figure 3.6, are the result of a bootstrap error analysis (Beers et al., 1990) of the 38 and 35 spectroscopic members of the north and south subclusters, respectively. These redshifts as well as the full Musket Ball Cluster spectroscopic catalog are presented in Table A.1 of Appendix A.2. The projected subcluster separation distribution, Figure 3.7, is the result of a bootstrap error analysis of the recursively estimated subclusters’ galaxy number density centroids (see e.g. Randall et al., 2008, for a description of this method). For each Monte Carlo realization individual values are drawn randomly from each of these distributions.

### 3.4.2 Musket Ball System Dynamics Results

This more complete analysis confirms that the Musket Ball Cluster merger is both significantly slower and further progressed compared to the Bullet Cluster, see Figure 3.8. To estimate a lower limit on how much further progressed I perform an additional Monte Carlo

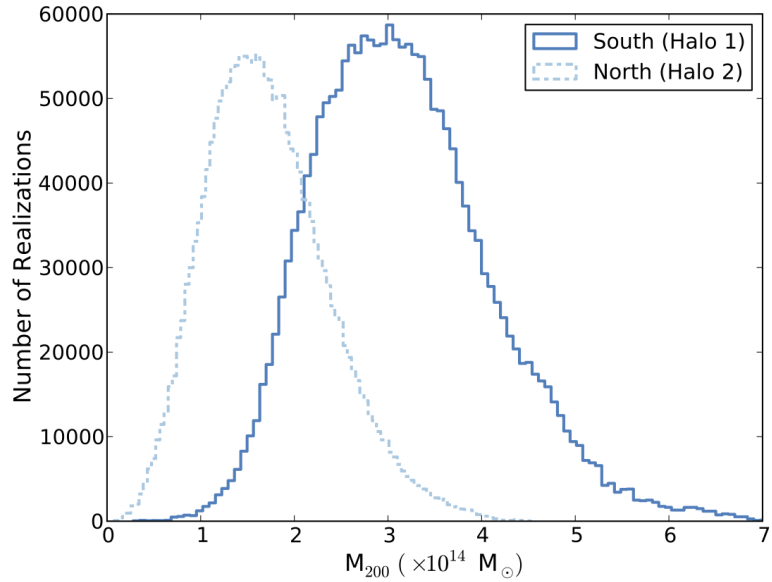


Figure 3.5 Weak lensing mass PDF's of the Musket Ball subclusters (Dawson et al., 2012).

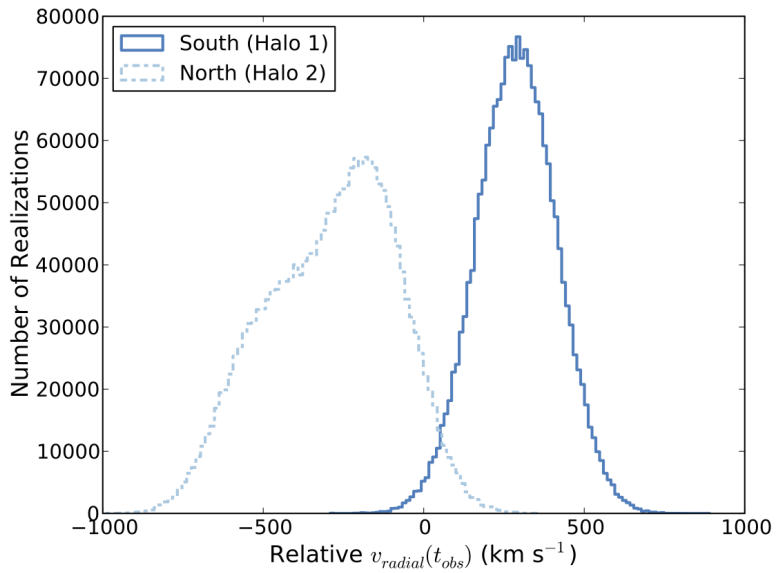


Figure 3.6 Relative radial subcluster velocity PDF's inferred from spectroscopic redshifts the Musket Ball Cluster galaxies (Dawson et al., 2012).

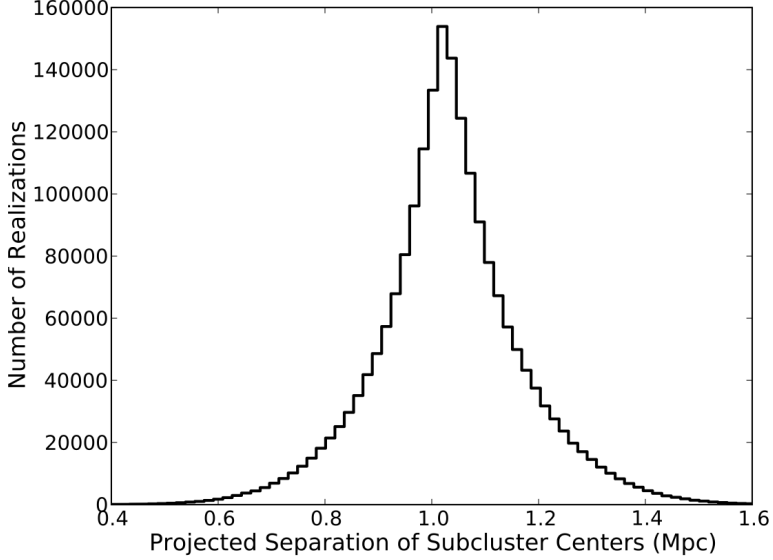


Figure 3.7 Projected separation PDF of the Musket Ball subcluster galaxy density centroids (Dawson et al., 2012).

analysis for  $TSC_{0_{\text{Musket}}} - TSC_{0_{\text{Bullet}}}$  assuming the marginalized  $TSC_0$  distributions (see Appendices A.3 and A.4). This is a lower limit since the Musket Ball observations, unlike the Bullet Cluster observations, cannot rule out the case that its subclusters have reached the apoapsis and are on a return trajectory (61% of the realizations have  $TSC_1$  less than the age of the Universe at  $z = 0.53$ ). I find that the Musket Ball is at least  $0.8^{+1.2}_{-0.4}$  Gyr ( $3.4^{+3.8}_{-1.4}$  times) further progressed than the Bullet Cluster, see Figure 3.9. This is in line with the more approximate 3–5 times estimate of Dawson et al. (2012). The Musket Ball’s relatively large  $TSC_0$  means that it has potential for providing tighter constraints on  $\sigma_{\text{DM}}$ , since the expected offset between the galaxies and dark matter will initially increase with increasing  $TSC_0$ . However as noted in §3.1, given enough time the expected offset will decrease due the gravitational attraction between the galaxies and dark matter. Also important in determining which cluster can provide the tightest  $\sigma_{\text{DM}}$  constraints is the fact the expected offset increases as a function of the cluster surface mass density and collision velocity, both of which are larger in the the case of the Bullet Cluster (compare Tables 3.2 & 3.3). Without running SIDM simulations it is difficult to know at what  $TSC_0$  the offset reaches its maximum, or which merger parameters are most important for maximizing the offset. The

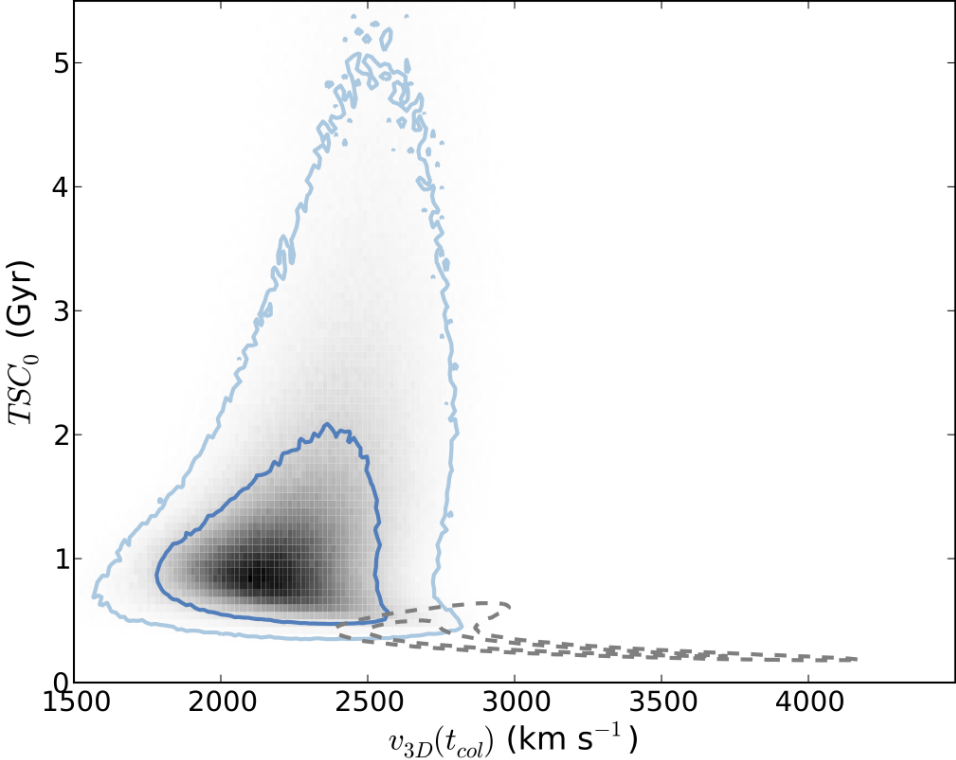


Figure 3.8 The posterior of the Musket Ball Cluster’s  $TSC_0$  and  $v_{3D}(t_{col})$  parameters is shown in grayscale with dark and light blue contours representing 68% and 95% confidence, respectively. For comparison the gray dashed contours are the Bullet Cluster’s 68% and 95% confidence intervals copied from Figure 3.4. The Musket Ball Cluster occupies a much different region of merger phase than the Bullet Cluster, having both a slower relative collision velocity and being observed in a much later stage of merger.

complete Musket Ball Cluster parameter estimates are summarized in Table 3.3 and plotted in Appendix A.4.

Note that just as a temporal prior was justified for the Bullet Cluster based on the observed shock front and increased temperature/mass estimate, I could apply a similar yet opposite prior to the Musket Ball since the temperature/mass estimate is consistent with the weak lensing inferred mass (additionally no shock front is observed). According to Randall et al. (2002) if the cluster mass and inferred X-ray temperature or luminosity cluster mass are approximately the same then  $TSC_0 \gtrsim 2t_{sc}$ , which in the case of the Musket Ball means  $TSC_0 \gtrsim 1.75$  Gyr. While this is consistent with my  $TSC_0$  estimate for the Musket Ball, it is not entirely appropriate to apply this prior since the X-ray observations are relatively

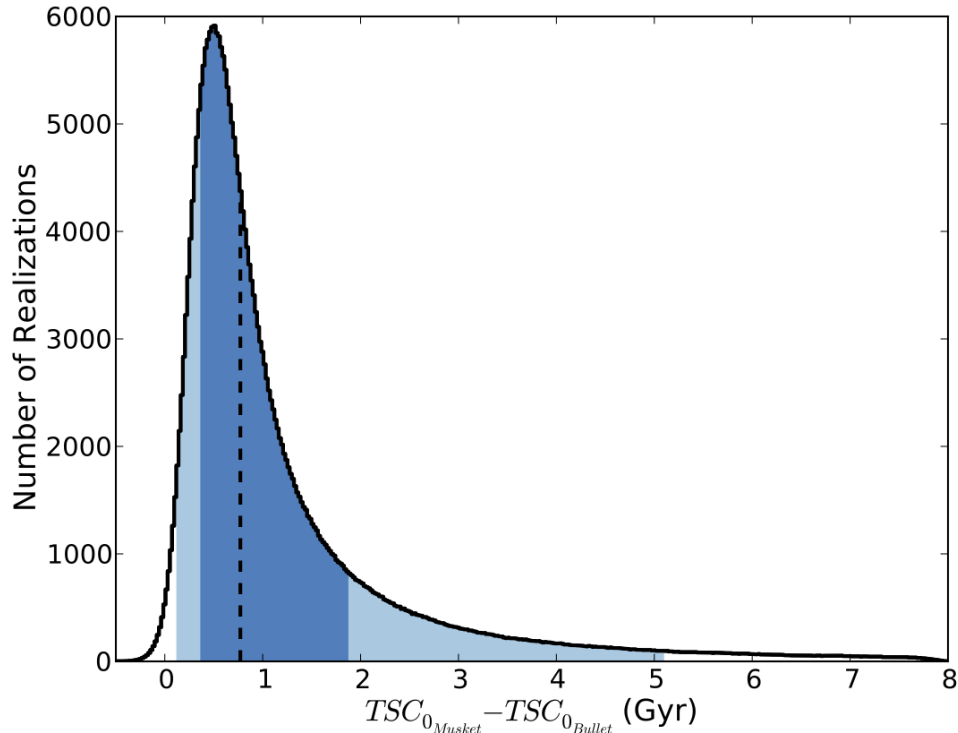


Figure 3.9 The histogram presents the  $TSC_{0_{\text{Musket}}} - TSC_{0_{\text{Bullet}}}$  distribution from random draws of the respective marginalized  $TSC_0$  distributions; showing that the Musket Ball Cluster merger is at least  $0.8^{+1.2}_{-0.4}$  Gyr ( $3.4^{+3.8}_{-1.4}$  times) further progressed than the Bullet Cluster merger. The black dashed line is the biweight-statistic location (Beers et al., 1982), the dark and light blue regions denote the bias-corrected 68% and 95% lower and upper confidence limits, respectively.

Table 3.3. Musket Ball Cluster parameter estimates

Parameter	Units	Location <sup>a</sup>	68% LCL–UCL <sup>b</sup>	95% LCL–UCL <sup>b</sup>
$M_{200_1}$	$10^{14} M_\odot$	3.2	2.3 – 4.3	1.6 – 5.5
$M_{200_2}$	$10^{14} M_\odot$	1.7	1.1 – 2.4	0.6 – 3.3
$z_1$		0.5339	0.5333 – 0.5345	0.5326 – 0.5352
$z_2$		0.5316	0.5305 – 0.5324	0.5294 – 0.5331
$d_{\text{proj}}$	Mpc	1.0	0.9 – 1.1	0.7 – 1.3
$\alpha$	degree	48	28 – 67	13 – 78
$d_{\text{3D}}$	Mpc	1.6	1.2 – 2.9	0.9 – 5.5
$d_{\text{max}}$	Mpc	2.1	1.5 – 3.8	1.1 – 7.3
$v_{\text{3D}}(t_{\text{obs}})$	$\text{km s}^{-1}$	670	390 – 1100	140 – 1500
$v_{\text{3D}}(t_{\text{col}})$	$\text{km s}^{-1}$	2300	2000 – 2500	1800 – 2800
$TSC_0$	Gyr	1.1	0.7 – 2.4	0.5 – 5.8
$TSC_1^{\text{c}}$	Gyr	3.5	2.0 – 7.2	1.4 – 12.0
$T$	Gyr	4.8	2.9 – 10.4	2.2 – 22.7

<sup>a</sup>Biweight-statistic location (see e.g. Beers et al., 1990).

<sup>b</sup>Bias-corrected lower and upper confidence limits, LCL and UCL respectively (see e.g. Beers et al., 1990).

<sup>c</sup>61% of the realizations with a valid  $TSC_0$  (i.e. less than the age of the Universe at the cluster redshift) have a valid  $TSC_1$ , meaning that it is possible that the Musket Ball Cluster is being observed in the “incoming” state.

shallow and cannot confidently rule out a temperature and luminosity boost (Dawson et al., 2012). However it is conceivable that this line of reasoning would be applicable with deeper X-ray observations, either for the Musket Ball or similar dissociative mergers.

## 3.5 Summary and Discussion

I have introduced a new method for determining the dynamic properties and associated uncertainty of dissociative cluster mergers given only the most general merger observables: mass of each subcluster, redshift of each subcluster, and projected separation the subclusters. I find that this method addresses the primary weaknesses of existing methods, namely enabling accurate parameter estimation and propagation of uncertainty near the collision state with a convergent solution achieved in  $\sim$ 6 CPU hours. I have confirmed that the two NFW halo model is capable of achieving the required 10% level accuracy by direct comparison with an N-body hydrodynamic simulation.

In applying this method to the Bullet Cluster I not only determined its merger dynamic parameters but found that the bulk of uncertainty in these parameters is due to uncertainty in  $\alpha$ , the angle of the merger with respect to the plane of the sky. Analyses that fail to account for the uncertainty in  $\alpha$  (all existing N-body simulations of the Bullet Cluster) will significantly underestimate the uncertainty in their results. This highlights the need to carefully select and model many possible realizations of the merger when trying to infer results from N-body simulations of a real merger (I discuss this further in §3.5.1). I have also shown how ex post facto priors can easily be applied to the results of the default priors to further constrain the inferred dynamic properties. In particular accurate measurement of the cluster gas properties can enable approximately a factor of two better constraint on the dynamic properties of the merger, principally through added constraint on the time scale of the merger.

I have also applied this method to the Musket Ball Cluster, validating the approximate

results of Dawson et al. (2012). Comparing the dynamic properties of the Musket Ball with those of the Bullet I have shown that the Musket Ball represents a significantly different volume of merger phase space. The Musket Ball Cluster, being  $3.4^{+3.8}_{-1.4}$  times further progressed than the Bullet Cluster, could potentially provide tighter constraints on  $\sigma_{\text{DM}}$  since the offset between galaxies and dark matter should initially increase with time post-merger for  $\sigma_{\text{DM}} > 0$ . And the larger the expected offset, the better the dark matter constraint when applying a method similar to Randall et al. (2008).

### 3.5.1 Suggested Uses of Method

While a general method for determining the dynamics properties of merging clusters has numerous applications, several are worth noting. As noted N-body simulations of specific merging clusters are computationally expensive; in particular one SIDM simulation of a single dissociative merger requires  $\sim$ 1–10 million CPU hours (private communication, James Bullock). Thus it is currently unfeasible to simulate all confirmed dissociative mergers. This method can be used to quickly determine which mergers provide the best  $\sigma_{\text{DM}}$  constraining power, enabling an efficient use of limited computational resources.

Additionally it is inappropriate to simply simulate one realization of a dissociative merger due to the broad range of merger phase space allowed by uncertainty in observed parameters, as discussed in detail in §3.3.2.1. Thus multiple simulations of each merger are required to properly represent the allowed phase space. One could conceivably reduce the number of required simulations by using the results of this method to select representative merger realizations that uniformly sample the merger phase space of interest (e.g. cluster mass,  $v_{\text{3D}}(t_{\text{col}})$ , and  $TSC_0$ ); then weight the results of each simulated realization by the integral of the corresponding local phase space PDF, as determined by this method. For example, one could estimate the uncertainty distribution of the  $\sigma_{\text{DM}}$  constraint inferred from SIDM simulations of the Bullet Cluster by weighting the constraint from each realization, where a realization with  $v_{\text{3D}}(t_{\text{col}})=2800 \text{ km s}^{-1}$  and  $TSC_0=0.4 \text{ Gyr}$  would receive greater weight than

one with  $v_{3D}(t_{\text{col}})=4000 \text{ km s}^{-1}$  and  $TSC_0=0.2 \text{ Gyr}$ , see Figure 3.4. Thus the results of this method will not only inform efficient selection of realizations to model but will reduce the number of simulations required to properly sample the posterior PDF's. Nevertheless SIDM simulations of mock clusters need to be performed to determine how much acceptable values of  $\sigma_{\text{DM}}$  affect the inferred merger dynamics properties.

General merger dynamic properties are also important for understanding how cluster mergers relate to other physical phenomena, such as galaxy evolution and radio relics. It is well established that galaxy clusters play an important role in the evolution of their member galaxies, but it is still unclear whether cluster mergers trigger star formation (e.g. Miller & Owen, 2003; Owen et al., 2005; Ferrari et al., 2005; Hwang & Lee, 2009), quench it (Poggianti et al., 2004), or have no immediate effect (Chung et al., 2010). Studying mergers at different  $TSC$  may resolve these seemingly conflicting results by discriminating between slow-working processes (e.g. galaxy harassment or strangulation) and fast-acting process (e.g. ram pressure stripping). Similarly, studying global merger dynamic properties may resolve the mystery of why many mergers have associated radio relics (e.g. Barrena et al., 2009; van Weeren et al., 2011b) yet others don't (e.g. Russell et al., 2011).

### 3.5.2 Extensions to the Method

While this method has advantages over existing methods there is room for considerable improvement. For example the method could be improved through the elimination of some of the simplifying assumptions of the model (see §3.2.1). One could attempt to incorporate sub-cluster mass accretion physics in a manner similar to the work of Angus & McGaugh (2008) or attempt to account for the possibility of a non-zero impact parameter. To incorporate the latter one must: 1) add angular momentum terms to the equations of motion, which is entirely feasible, and 2) prescribe a reasonable impact parameter prior. Randall et al. (2002) nicely outline how to determine an impact parameter PDF for halo mergers of variable mass by utilizing the PDF of the dimensionless *spin parameter*, determined from linear theory of

the growth of structure (Peebles, 1993) and simulations (Bullock et al., 2001). However, this prior should be adjusted to account for the amount of gas dissociated during the observed merger, since this amount will decrease as the impact parameter increases. Without a systematic study of various mergers in hydrodynamic simulations it is unclear exactly what adjustment an observed large dissociation of gas should infer.

Another significant extension to the model could be the inclusion of SIDM physics. As mentioned in the previous section, one of the promising uses of this method is to suggest which mergers might provide the best  $\sigma_{\text{DM}}$  constraining power. However one could take this a step further by including an analytic treatment of SIDM physics (e.g. Markevitch et al., 2004), thereby enabling analytic estimates of  $\sigma_{\text{DM}}$  relevant effects for a given merger. Then this method could be used in conjunction with observed dissociative mergers to place direct constraints on  $\sigma_{\text{DM}}$ . Due to the increased complexity of the physics involved it would be necessary to verify this extension with SIDM N-body simulations.

*Note:* W. Dawson has made Python code implementing the discussed Monte Carlo method openly available at [git://github.com/MCTwo/MCMAC.git](https://github.com/MCTwo/MCMAC.git). He has also made all supporting work to this paper openly available at [git://github.com/wadawson/merging-cluster-dynamics-paper.git](https://github.com/wadawson/merging-cluster-dynamics-paper.git).

I thank my adviser David Wittman who has always encouraged my research-freewill, while at the same time providing invaluable input and correcting guidance. Our many fruitful discussions have touched every aspect of this work. I also thank the Deep Lens Survey — in particular Perry Gee — for access to the 2007 Keck LRIS spectra, as well as Perry Gee and Brian Lemaux for assistance in reduction of the 2011 Keck DEIMOS spectra. I am grateful to Jack P. Hughes for discussions on constraining the Bullet Cluster’s TSC by the observed X-ray shock feature and boosted temperature/luminosity, and Reinout J. van Weeren for discussions on the possibilities of constraining the dynamics and geometry of mergers using radio relics. Finally I would like to thank Maruša Bradač, Ami Choi, James Jee, Phil Marshall, Annika Peter, Michael Schneider, Reinout van Weeren, and David

Wittman for their substantial reviews of earlier drafts.

Support for this work was provided by NASA through Chandra Award Number GO1-12171X issued by CXO Center, which is operated by the SAO for and on behalf of NASA under contract NAS8-03060. Support for program number GO-12377 was provided by NASA through a grant from STScI, which is operated by the Association of Universities for Research in Astronomy, Inc., under NASA contract NAS5-26555. Support for this work was also provided by Graduate Research Fellowships through the University of California, Davis. I would also like to acknowledge the sultry universe who hides her secrets well.

This work made use of the following facilities: CXO (ACIS-I), HST (ACS), Keck:I (LRIS), Keck:2 (DEIMOS), Mayall (MOSAIC 1 & 1.1), Subaru (Suprime-Cam), SZA.

# Chapter 4

## Musket Ball Cluster: Dark Matter Implications

Portions of this chapter were originally published in the article titled *Discovery of a Dissociative Galaxy Cluster Merger with Large Physics Separation* which was published in the March 2012 issue of the Astrophysical Journal Letters (Volume 747, pp. L42).

Chapter abstract text

### 4.1 Introduction

Intro text (Dawson et al., 2012)

### 4.2 Location Estimation

For the original work of Dawson et al. (2012) (see Chapter 2) I estimated the weak lensing subcluster positions and errors on their positions by using the location of the peak signal in a region and estimated the variance on the peak by measuring the peak location of each bootstrap iteration within the selected region. For this chapter, rather than using the location

of the peak and variance of the peak, I have adopted an iterative centroid estimation scheme, similar to Randall et al. (2008). I begin by calculating the centroid of a large aperture that encompasses one subcluster, but excludes the other. I then decrease the aperture, recenter on the previously calculated centroid, and estimate the centroid of the new aperture. This process is repeated until the aperture is decreased to a radius of XXX kpc. To estimate the uncertainty on the location I perform this process on each iteration of a random bootstrap sample map, resulting in a array of centroid values. The uncertainty on the location is then inferred from the variance of this array of centroid values.

### 4.2.1 Galaxies

#### 4.2.1.1 Noise and Systematic Effects

### 4.2.2 Gas

### 4.2.3 Weak Lensing

## 4.3 Gas–Weak Lensing Offset

Given the evident merger scenario we are able to use the first method of Markevitch et al. (2004) and place a rough limit on the DM self-interaction cross-section,  $\sigma_{\text{DM}}$ . This method compares the scattering depth of the dark matter,  $\tau_{\text{DM}} = \sigma_{\text{DM}} m_{\text{DM}}^{-1} \Sigma_{\text{DM}}$ , with that of the ICM gas,  $\tau_{\text{ICM}} \approx 1$ , where  $m_{\text{DM}}$  is the DM particle mass and  $\Sigma_{\text{DM}}$  is the surface mass density of the DM particles.  $\Sigma_{\text{DM}}$  is approximately the WL measured surface mass density,  $\Sigma$ , since  $\sim 80\%$  of a typical cluster’s mass is DM (Diaferio et al., 2008). For ease of comparison with the results of Markevitch et al. (2004) and Merten et al. (2011) we examine the surface density averaged over the face of the subcluster within  $r=125$  kpc, which is  $\Sigma \approx 0.15 \text{ g cm}^{-2}$ ; thus we find  $\sigma_{\text{DM}} m_{\text{DM}}^{-1} \lesssim 7 \text{ cm}^2 \text{ g}^{-1}$ . Note that we cannot apply the velocity-dependent  $\sigma_{\text{DM}}$  constraint methods outlined by Markevitch et al. (2004) since our analytic model assumes

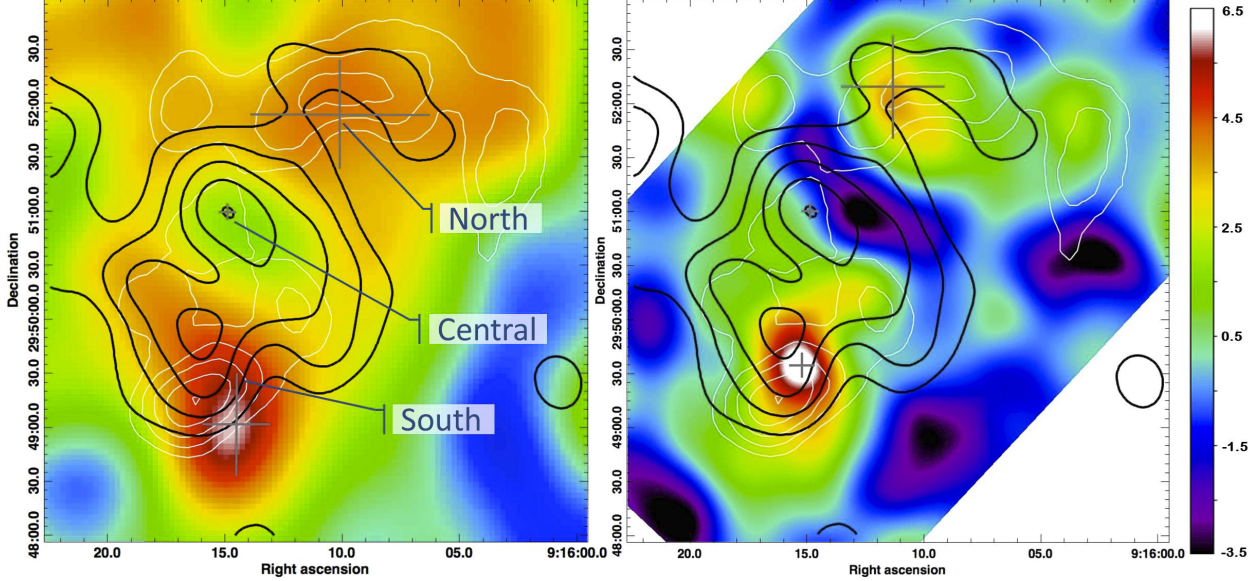


Figure 4.1 Comparison of the Subaru  $i'$ -band ground-based (left) and HST space-based (right) WL mass signal-to-noise maps (color) of DLSCL J0916.2+2951 with the X-ray distribution (bold black contours) and galaxy number density (white contours, same as Figure 4.2). The peak centers and corresponding one sigma errors are denoted by the gray cross-hairs. In both analyses there is agreement between the location and relative magnitude of galaxies and WL yet the majority of the cluster gas is centered  $\sim 1.4'$  between the North and South subclusters in a local mass underdensity, providing evidence that the North and South subclusters have undergone the first pass-through of a major merger. The scale of each map is equivalent and the image field-of-view is the same as Figures 2.1 & 4.2. The map created from the joint Subaru/HST catalog looks nearly identical to the HST map, with only slight variations in the scale (see Table 2.1).

$\sigma_{\text{DM}} = 0$  (Dawson et al., 2012; Dawson, 2013).

## 4.4 Galaxy–Weak Lensing Offset

Section text

### 4.4.0.1 Noise and Systematic effects

*Copied from Chandra/HST proposal. Need to edit.*

Several sources of noise and systematic effect could cause such an offset: (1) the mass of the northern subcluster pulling off the overall mass centroid; (2) the gas mass just to the

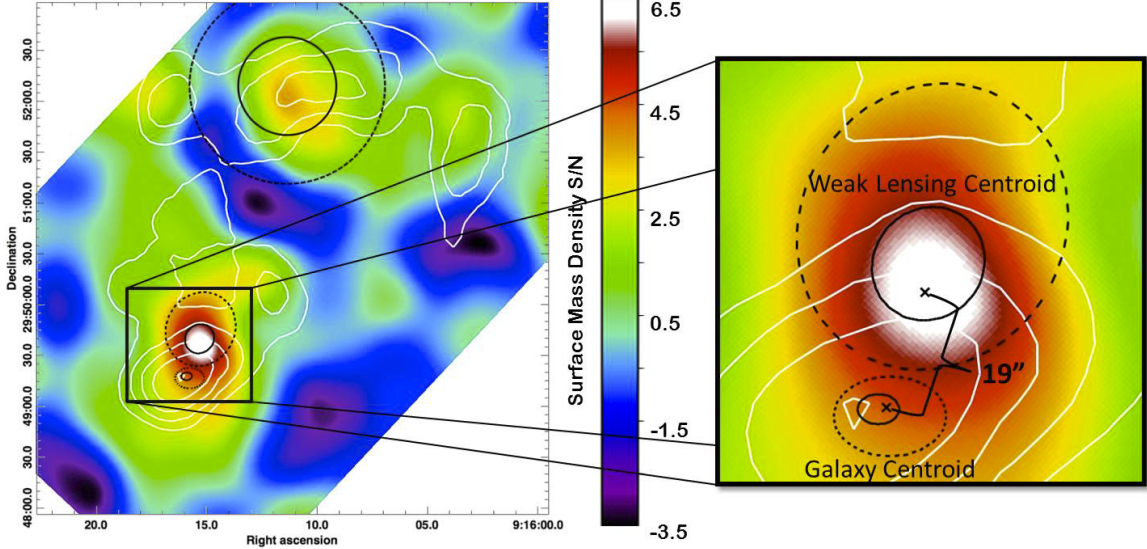


Figure 4.2 The WL mass signal-to-noise map based on HST measured shapes is shown in color with the galaxy number density isopleths in white. The inset shows the 68% (solid black) and 95% (dashed black) confidence intervals on the South subcluster’s WL and galaxy density centroids. We have detected a 19'' offset between the galaxies and the WL mass in the South subcluster that is consistent with the offset expected if DM has a non-zero cross-section just below the current published upper limits. This is the best astrophysical evidence to date of a non-zero DM cross-section. While a consistent offset is observed for the North subcluster, the large WL centroid error prohibits measurement of a significant offset for that subcluster.

north doing the same; and (3) unrelated structures along the line of sight. We show below that (2) is the primary concern and can be solved with Chandra data, and that (4) HST data are required to tighten up the statistical uncertainty on the size of offset. Together, these data will enable measurement of  $\sigma_{\text{DM}} m_{\text{DM}}^{-1}$ .

(1) We model the surface mass density of the north and south subclusters with three NFW halos using masses determined by Dawson et al. (2012). We recursively estimate the centroid of this model and find an offset 3.4'' from the true centroid towards the northern subcluster. (2) We then combine estimated surface mass densities of the Central and South gas concentrations with the previous DM surface densities from step (1) which results in a 7.6'' centroid offset (dashed red curve of Figure 4.1). For perspective, if we double the gas mass the total offset increases to 10'', or if we account for the uncertainty in our distribution of the gas mass the modeled centroid offset ranges from 3.4'' to 9.4'' (light red region of

Figure 4.1). With the proposed Chandra observations we can better constrain the gas mass by approximately a factor of 10 and constrain the distribution of the gas mass so that the resulting uncertainty in the modeled centroid offset is reduced by at least a factor of 2 (dark red region of Figure 4.1). (3) As discussed in Dawson et al. (2012) we find no evidence of significant line of sight structures using our full sample of 654 spectroscopic redshifts (with uniform selection over  $0 < z < 1.0$ ) as well as photometric redshifts. Based our findings we confidently rule out any line of sight structures with  $M_{200} \gtrsim 1 \times 10^{12} M_\odot$ ; any undetected structure will have negligible impact on the offset. (4) We estimate the noise of the galaxy density and weak lensing centroids by performing the recursive centroid analysis on bootstrap samples of each. For the galaxy density centroid errors we take 1000 bootstrap samples of the spectroscopically confirmed cluster galaxies and remaining galaxies with  $0.43 < z_{\text{phot}} < 0.63$  (roughly the cluster redshift  $\pm \sigma_{z_{\text{phot}}}$ ). Similarly we estimate the weak lensing centroid errors by analyzing 1000 bootstrap samples of the lensed background galaxies.

## 4.5 Discussion

Discussion text

### 4.5.1 Subsection title

## 4.6 Conclusions

Conclusion text

**acknowledgements:** Acknowledgment text

# Chapter 5

## Perspective: Summary & Discussion

Chapter abstract text

### 5.1 Dissertation Summary

Intro text

### 5.2 Discussion on the Path Forward

#### 5.2.1 Bridging the Gap Between Observations and Simulations

*Should look at some proposal text*

The SIDM simulations of observed mergers are one of the most important aspects of the MC2 plan. Not only are they necessary to place the tightest constraints on  $\sigma$ DM (e.g. Randall et al. 2008), but by applying the same measurement techniques to the simulations as the observed mergers they will enable us to marginalize over systematic errors.

Beyond the computational challenges of simulating SIDM (which our group has recently mastered, Rocha et al. 2012 & Peter et al. 2012), it is highly non-trivial to simulate an actual observed merger. This is due to the fundamentally limited information observations

provide for a given merger (Dawson 2012b). Thus a single observed merger can conceivably be represented by a wide range of simulated merger scenarios. To address this issue I will implement an importance sampling method to identify likely realizations of the observed merger in cosmological N-body simulations (Figure 3), extract a representative sample of these mergers, and in collaboration with MC2 members resimulate these with SIDM physics (Dawson et al. in prep). Because each simulated realization of the observed merger will have an associated likelihood, I will be able to use the resulting  $\sigma$ DM constraints of each realization to create a posterior probability density function. This work will result in the first quantitative estimate of the  $\sigma$ DM constraint uncertainty.

### 5.2.2 Theoretical model of the behavior of SIDM during mergers

Develop a theoretical model of the behavior of SIDM during the merger process and implement this into my existing analytic merger code.

While Project 1 will enable us to extract the tightest possible  $\sigma$ DM constraints from a given merger, it is computationally intensive and marginalizes over interesting physical phenomena. I am working with Manoj Kaplinghat to develop a theoretical model of the merger process involving SIDM. I will then incorporate this model into my existing method for determining the dynamic properties of observed mergers (Dawson 2012b), enabling quantitative measurement or constraint of  $\sigma$ DM for a given merger and associated galaxy-DM offset. This project is highly complementary to Project 1: firstly, comparing the predictions of this analytic method with the more detailed simulations will provide needed confirmation and secondly, since simulations are expensive this quick analytic method can be used to determine the mergers with the greatest constraining power and prioritize their position in the simulation queue.

### **5.2.3 Simulating mergers with SIDM**

Use results of the SIDM simulations of multiple observed dissociative mergers to place the best measurement or tightest constraint possible on  $\sigma_{\text{DM}}$ .

Because I will have taken care to properly quantify the uncertainty of dark matter constraints from each of the dissociative mergers (see Project 1), I will be able to properly combine the weighted expectations of each mergers  $\sigma_{\text{DM}}$  constraint to effectively beat down the Poisson noise of the centroid offset measurement. It is only through a consistent and systematic approach (such as the proposed) that one can properly combine the constraints of individual mergers.

### **5.2.4 Find and study more dissociative mergers**

#### **5.2.4.1 Ongoing efforts**

Radio relic sample and existing mergers.

#### **5.2.4.2 Near-term**

More radio relics and SZ+DES mergers

#### **5.2.4.3 Next ten years**

LSST + all sky X-ray surveys (e.g. eROSITA)

Identify and follow-up more dissociative mergers to increase the sample size and further reduce the random noise of the centroid measurement in order to constrain more complex SIDM models (e.g. velocity dependent cross-section).

I will refine the optical-SZ identification method with plans of applying it to the overlapping DES and ACT/SPT surveys. Based on the simulated and observed SZ cluster counts in the SPT survey (Vanderlinde et al. 2010 & Song et al. 2012) and the fraction of all clusters that are dissociative mergers (Forero-Romero et al. 2010) I calculate that  $\sim 50$  detectable

dissociative mergers will be observed in the 4000 deg<sup>2</sup> SPT-DES survey. Selection bias will result in mergers with large mass (i.e. better signal-to-noise) and large projected separations (i.e. later stage mergers where the expected DM-galaxy offset is maximized). These will be some of the best dissociative mergers with which to constrain  $\sigma_{\text{DM}}$ .

Together with Reinout van Weeren (Einstein Fellow at CfA and member of MC2), we are pioneering a method of dissociative merger identification using radio observations. Radio selection is a potentially efficient way to select merging systems because the shock produced by a merger results in a “radio relic” (diffuse emission in an arc around part of the cluster, e.g. van Weeren et al. 2010) and wide-area radio surveys will provide many candidates. NVSS has already found a few dozen, and LOFAR is projected to find about 1000 (Nuza et al. 2012).

Overall this project will provide large samples from which to cull the very best mergers (complement of Project 2) and follow-up with detailed observations and simulations. Additionally, the sheer numbers involved will make it feasible to perform the galaxy-DM offset measurement using ground based data alone (e.g. Magellan).

### 5.3 Current Progress along this Path

Section text

**acknowledgements:** Acknowledgment text

# Appendix A

## Dynamics of Merging Clusters

### Appendix

#### A.1 Potential Energy of Two Truncated NFW Halos

Generically the potential energy of a two-halo system with center to center separation  $r$  is

$$V(r) = \int \Phi_1(r') dm_2, \quad (\text{A.1})$$

where  $\Phi_1(r')$  is the gravitational potential of halo 1 as a function of radial distance  $r'$  from the center of the halo 1 to the mass element of halo 2,  $dm_2$ . I derive  $\Phi_1(r)$  for the case of a truncated NFW halo in §A.1.1. The integral of equation A.1 can be approximated as a summation over  $N \times N$  mass elements,  $m_{2_{ij}}$ , each with area  $dr \times d\theta$ , where  $i$  and  $j$  range from  $0 \rightarrow N - 1$ ,

$$V(r) \approx \sum_{i=0}^{N-1} \sum_{j=0}^{N-1} \Phi_1(r'_{ij} + \epsilon) m_{2_{ij}},$$

where  $r'_{ij}$  is the distance from the center of halo 1 to the 2<sup>nd</sup> halo's mass element  $m_{2_{ij}}$ , as derived in §A.1.2, and  $\epsilon$  is the softening length which reduces the effects of artificial singularities.

### A.1.1 Truncated NFW Gravitational Potential

For an axially symmetric mass distribution the potential can be expressed as a series of Legendre Polynomials

$$\Phi_n(r) = -\frac{2\pi G}{(n + 1/2)r^{n+1}} \int_0^r r'^{n+2} \rho_n(r') dr' - \frac{2\pi G r^n}{n + 1/2} \int_r^\infty r'^{1-n} \rho_n(r') dr' \quad (\text{A.2})$$

where

$$\rho_n(r) = (n + 1/2) \int_0^\pi \rho(r, \theta) P_n(\cos \theta) \sin \theta d\theta. \quad (\text{A.3})$$

Assuming a spherical NFW halo

$$\rho_{\text{NFW}}(r) = \frac{\rho_s}{r/r_s(1 + r/r_s)^2}$$

only the zero<sup>th</sup> order term of Equation A.3 remains

$$\rho_{\text{NFW}}(r) = \rho_0(r)$$

and Equation A.2 reduces to

$$\begin{aligned} \Phi_{\text{NFW}}(r) &= -\frac{4\pi G}{r} \int_0^r r'^2 \rho_{\text{NFW}}(r') dr' - 4\pi G \int_r^\infty r' \rho_{\text{NFW}}(r') dr' \\ \Phi_{\text{NFW}}(r) &= -\frac{4\pi G \rho_s}{r} \left[ \int_0^r \frac{r'^2}{r'/r_s(1 + r'/r_s)^2} dr' + r \int_r^\infty \frac{r'}{r'/r_s(1 + r'/r_s)^2} dr' \right]. \end{aligned}$$

Since I truncate the NFW halo at  $r_{200}$  the  $\infty$  in the second integral becomes  $r_{200}$  and

$$\Phi_{\text{NFW}_T}(r) = \begin{cases} -\frac{4\pi G}{r} \rho_s r_s^3 \left[ \ln(1 + r/r_s) - \frac{r}{r_s + r_{200}} \right], & \text{if } r \leq r_{200}; \\ -\frac{GM_{200}}{r}, & \text{if } r > r_{200}. \end{cases} \quad (\text{A.4})$$

### A.1.2 Mass Elements of a Truncated NFW Halo

Given the differential mass elements for a spherically symmetric halo

$$dm = 2\pi\rho(r, \theta)r^2 \sin(\theta)d\theta dr,$$

and discretizing the mass into elements with lengths  $\delta r = r_{200_2}/N$  and  $\delta\theta = \pi/N$  the halo 2 mass elements are given by

$$m_{ij} = 2\pi \int_{i\delta r}^{(i+1)\delta r} \int_{j\delta\theta}^{(j+1)\delta\theta} \rho(r')r'^2 \sin(\theta')d\theta' dr'.$$

For an NFW halo this becomes

$$m_{ij} = 2\pi\rho_s r_s^3 [\cos(j\delta\theta) - \cos((j+1)\delta\theta)] \left[ \left(1 + \frac{(i+1)\delta r}{r_s}\right)^{-1} - \left(1 + \frac{i\delta r}{r_s}\right)^{-1} + \ln \left[ \frac{(i+1)\delta r + r_s}{i\delta r + r_s} \right] \right].$$

## A.2 Musket Ball Cluster Redshift Catalog

The Musket Ball Cluster redshift catalog (Table A.1) contains 738 spectroscopically confirmed galaxy redshifts. The galaxies are within an  $\sim 18' \times 18'$  area centered on the Musket Ball Cluster (139.05 deg, +29.85 deg). The source of the redshifts are from three separate spectroscopic surveys: 1) *LRIS 2007* was carried out on 2007 January 15 using the Keck:I LRIS instrument, 2) *DEIMOS 2011A* was carried out on 2011 March 1 & 2 using the Keck:II DEIMOS instrument, and 3) *DEIMOS 2012B* was carried out on 2013 January 16 using the Keck:II DEIMOS instrument.

The *DEIMOS 2011A* observations consisted of 6 slit masks with 1''slits and using the 1200 line mm $^{-1}$  grating, tilted to a central wavelength of 6700 Å, resulting in a pixel scale of 0.33 Å pixel $^{-1}$ , a resolution of  $\sim 1.1$  Å(50 km s $^{-1}$ ), and typical wavelength coverage of 5400Å to 8000Å. The *DEIMOS 2013B* observations consisted of 1 slit mask with 1''slits and using the 1200 line mm $^{-1}$  grating, tilted to a central wavelength of 6200 Å, resulting in a pixel scale of 0.33 Å pixel $^{-1}$ , a resolution of  $\sim 1$  Å(50 km s $^{-1}$ ), and typical wavelength coverage of 4900Å to 7500Å. The exposures for each DEIMOS mask ( $\sim 3 \times 20$  minutes) were combined using the DEEP2 version of the spec2d package (Newman et al., 2012). This package combines the individual exposures of the slit mosaic and performs wavelength calibration, cosmic ray removal and sky subtraction on slit-by-slit basis, generating a processed two-dimensional spectrum for each slit. The spec2d pipeline also generates a processed one-dimensional spectrum for each slit. This extraction creates a one-dimensional spectrum of the target, containing the summed flux at each wavelength in an optimized window. Table A.1 only includes high quality ( $Q \geq 3$ , see Newman et al. (2012) for an explanation on the quality codes) galaxy spectra. Details of the *LRIS 2007* observations and reduction are discussed in the Deep Lens Survey data release paper (Wittman et al. in prep).

Table A.1. Musket Ball Cluster Redshift Catalog

RA (hh:mm:ss.sss)	Dec (dd:mm:ss.ss)	PosErr (arcsec)	z	$\sigma z$	Source	R (mag)	$\sigma R$ (mag)
09:15:40.142	+29:55:06.71	0.5	0.234777	0.000020	DEIMOS 2011A	20.983	0.007
09:15:41.501	+29:47:07.64	0.5	0.530381	0.000024	DEIMOS 2011A	23.398	0.048
09:15:41.682	+29:55:13.05	0.5	0.704062	0.000033	DEIMOS 2011A	22.586	0.024
09:15:41.726	+29:56:12.79	0.5	0.498200	0.000015	DEIMOS 2011A	22.664	0.016
09:15:42.418	+29:46:55.71	0.5	0.899342	0.000101	DEIMOS 2011A	22.246	0.017

Note. — Table A.1 is published in its entirety in the electronic edition of the *Astrophysical Journal*. A portion is shown here for guidance regarding its form and content.

### A.3 Bullet Cluster Result Plots

This section contains the parameter results array plots for the Bullet Cluster case including the added temporal prior of §3.3.2.2. For ease of display the parameters are grouped in three categories (*Input*, *Geometry*, and *Velocity & Time*) resulting in a six subplot results array, see Figure A.1. The *Input* parameters consist of:  $M_{200_1}$ ,  $M_{200_2}$ ,  $z_1$ ,  $z_2$ , and  $d_{\text{proj}}$ , where halo 1 refers to the “main” subcluster and halo 2 refers to the “bullet” subcluster. The *Geometry* parameters consist of the randomly drawn  $\alpha$ , and calculated  $d_{3D}$ , and  $d_{\text{max}}$ . The calculated *Velocity & Time* parameters consist of:  $TSC_0$ ,  $TSC_1$ , and  $T$ .

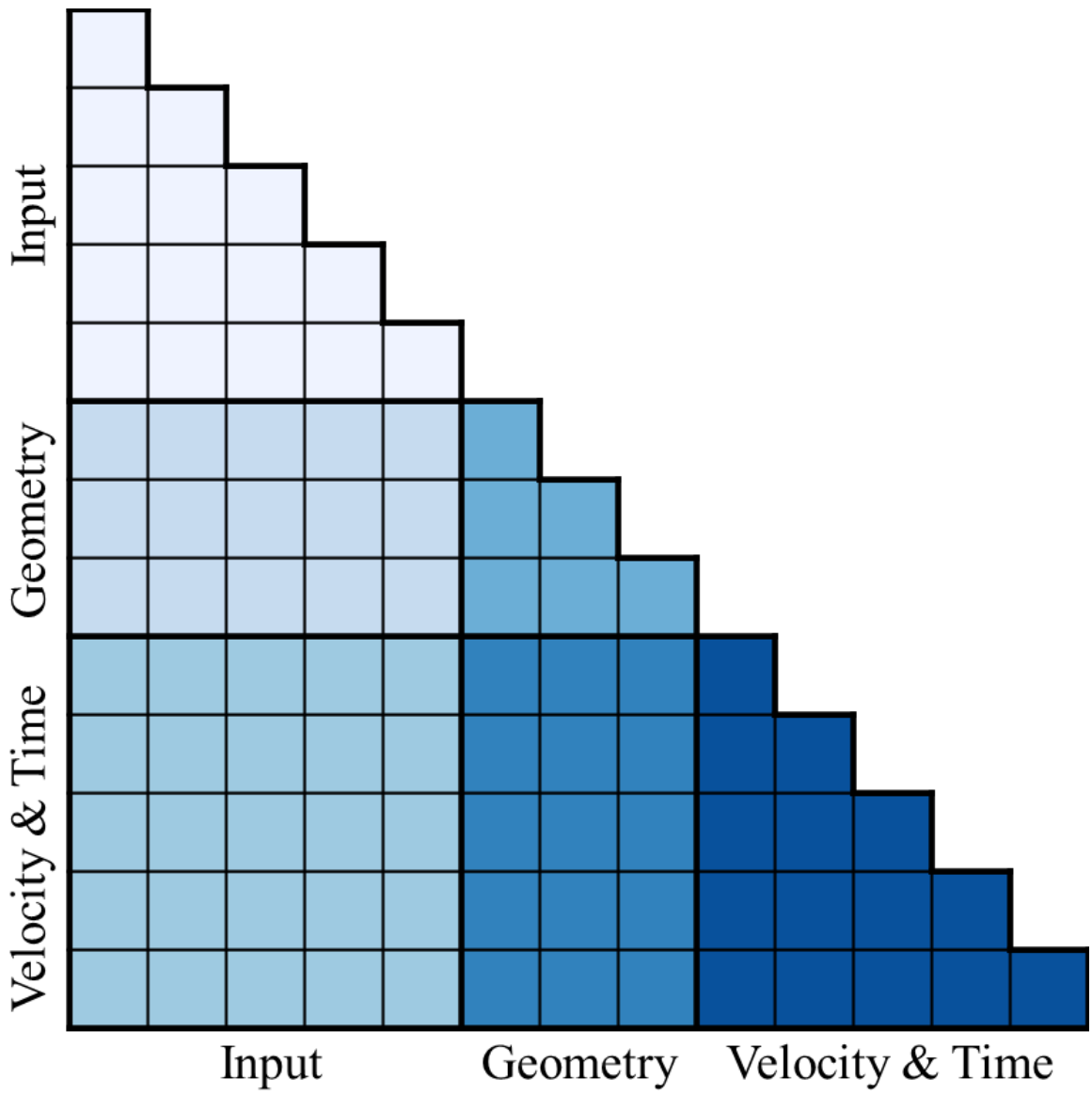


Figure A.1 For ease of display the results array is divided into six subplots, Figures A.2–A.6. The Input parameters consist of:  $M_{200_1}$ ,  $M_{200_2}$ ,  $z_1$ ,  $z_2$ , and  $d_{\text{proj}}$ . The calculated Geometry parameters consist of:  $\alpha$ ,  $d_{3\text{D}}$ , and  $d_{\text{max}}$ . The calculated Velocity & Time parameters consist of:  $v_{3\text{D}}(t_{\text{obs}})$ ,  $v_{3\text{D}}(t_{\text{col}})$ ,  $TSC_0$ ,  $TSC_1$ , and  $T$ .

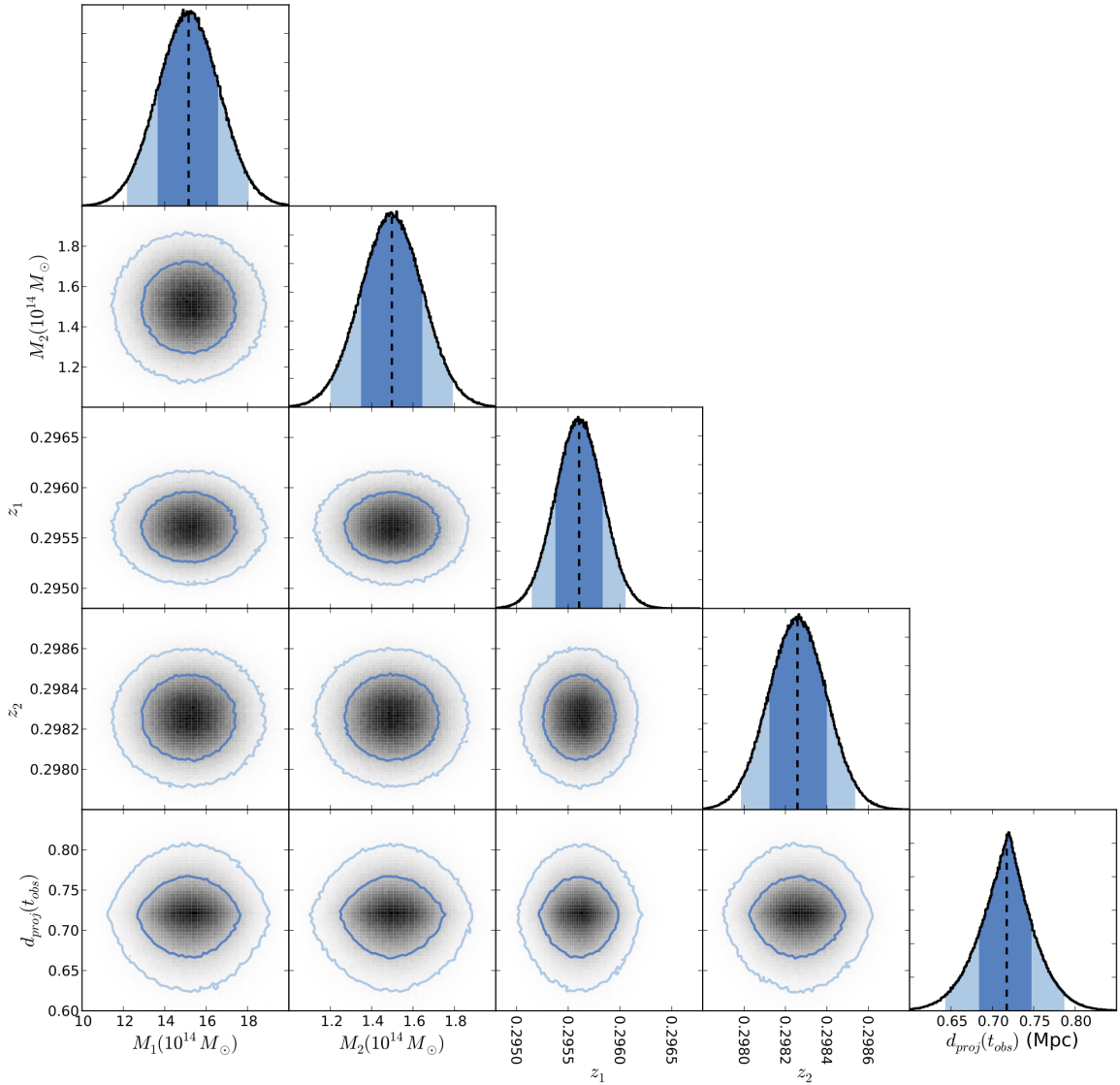


Figure A.2 Bullet Cluster marginalized *Input vs. Input* parameters result plots, for the case including the added temporal prior of §3.3.2.2. Dark and light blue colors correspond to 68% and 95% confidence intervals, respectively. The black dashed line is the biweight-statistic location (Beers et al., 1982).

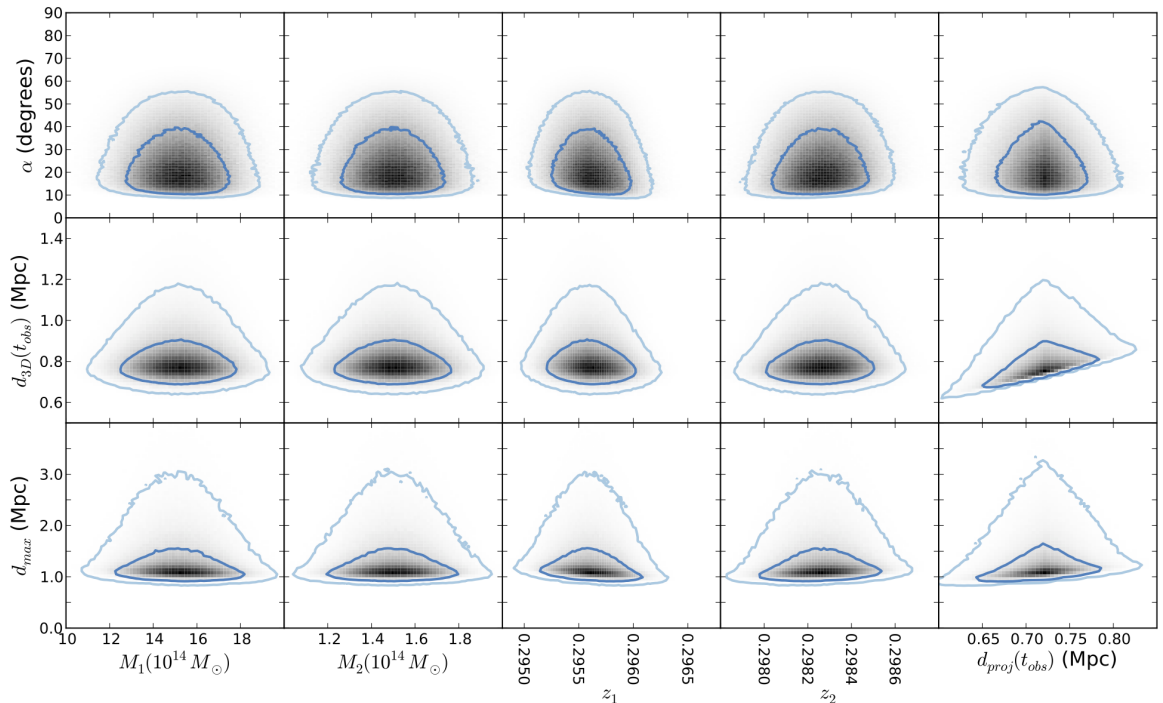


Figure A.3 Bullet Cluster marginalized *Input vs. Geometry* parameters result plots, for the case including the added temporal prior of §3.3.2.2. Dark and light blue colors correspond to 68% and 95% confidence intervals, respectively.

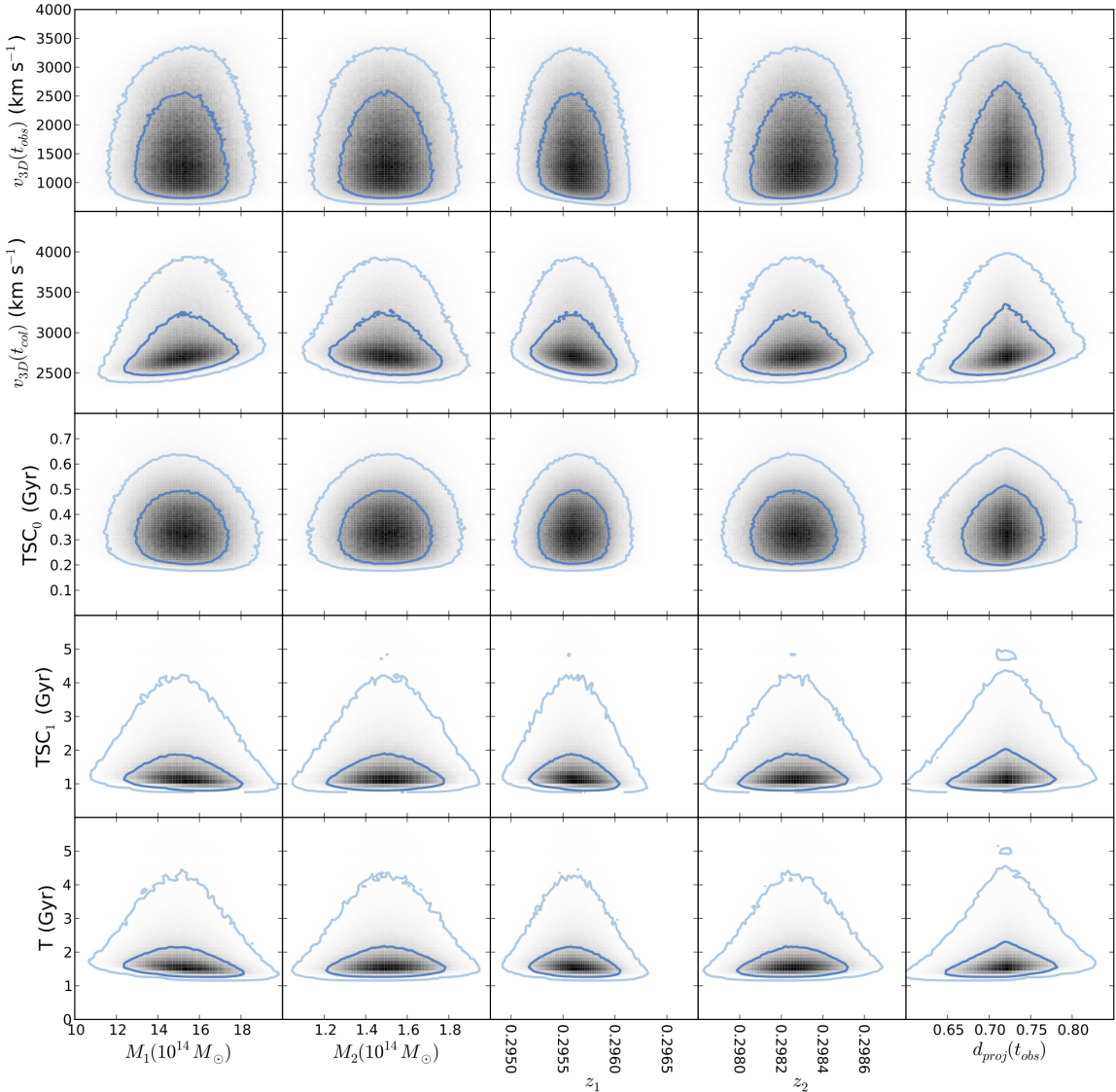


Figure A.4 Bullet Cluster marginalized *Input vs. Velocity & Time* parameters result plots, for the case including the added temporal prior of §3.3.2.2. Dark and light blue colors correspond to 68% and 95% confidence intervals, respectively.

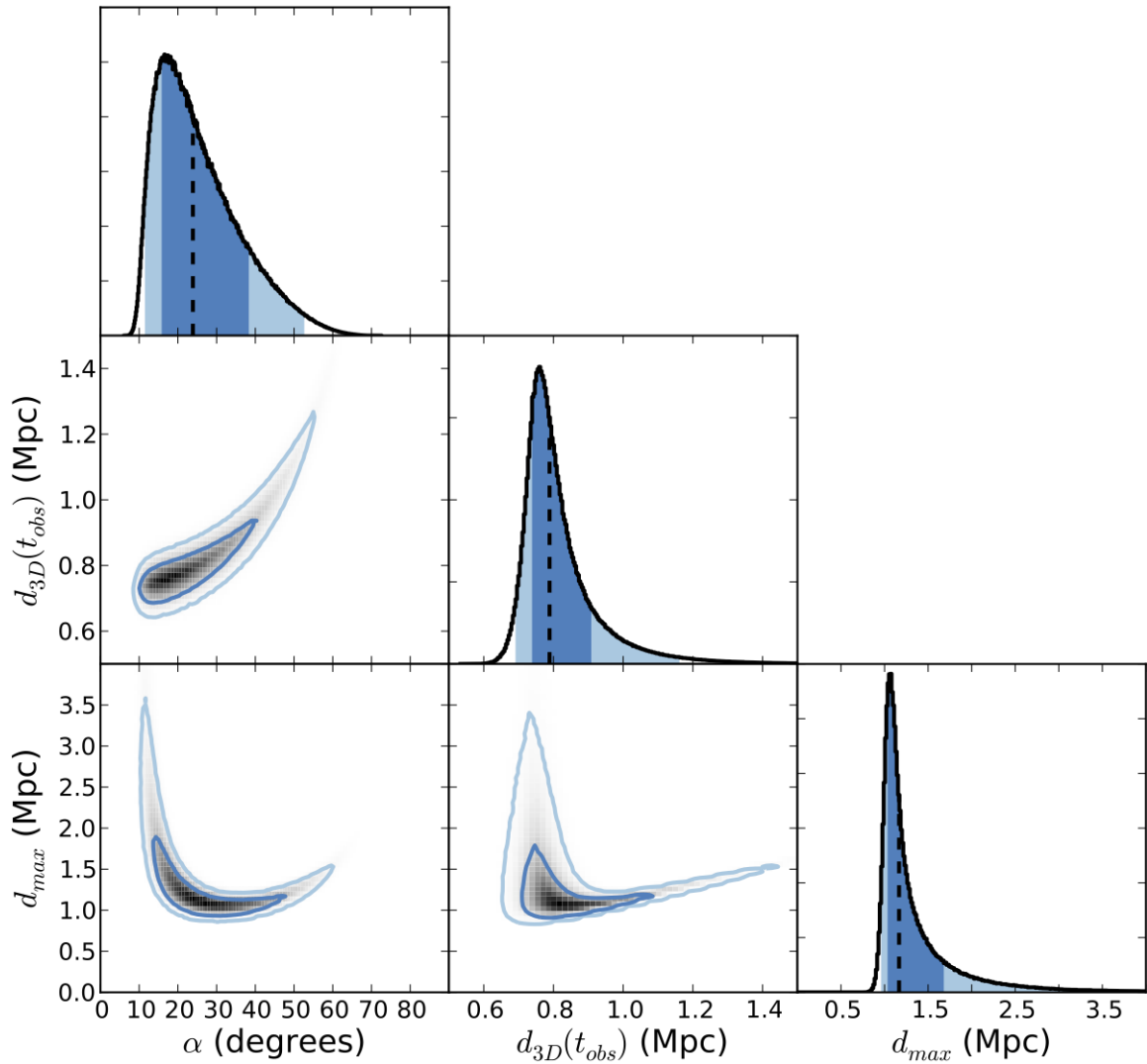


Figure A.5 Bullet Cluster marginalized *Geometry vs. Geometry* parameters result plots, for the case including the added temporal prior of §3.3.2.2. Dark and light blue colors correspond to 68% and 95% confidence intervals, respectively. The black dashed line is the biweight-statistic location (Beers et al., 1982).

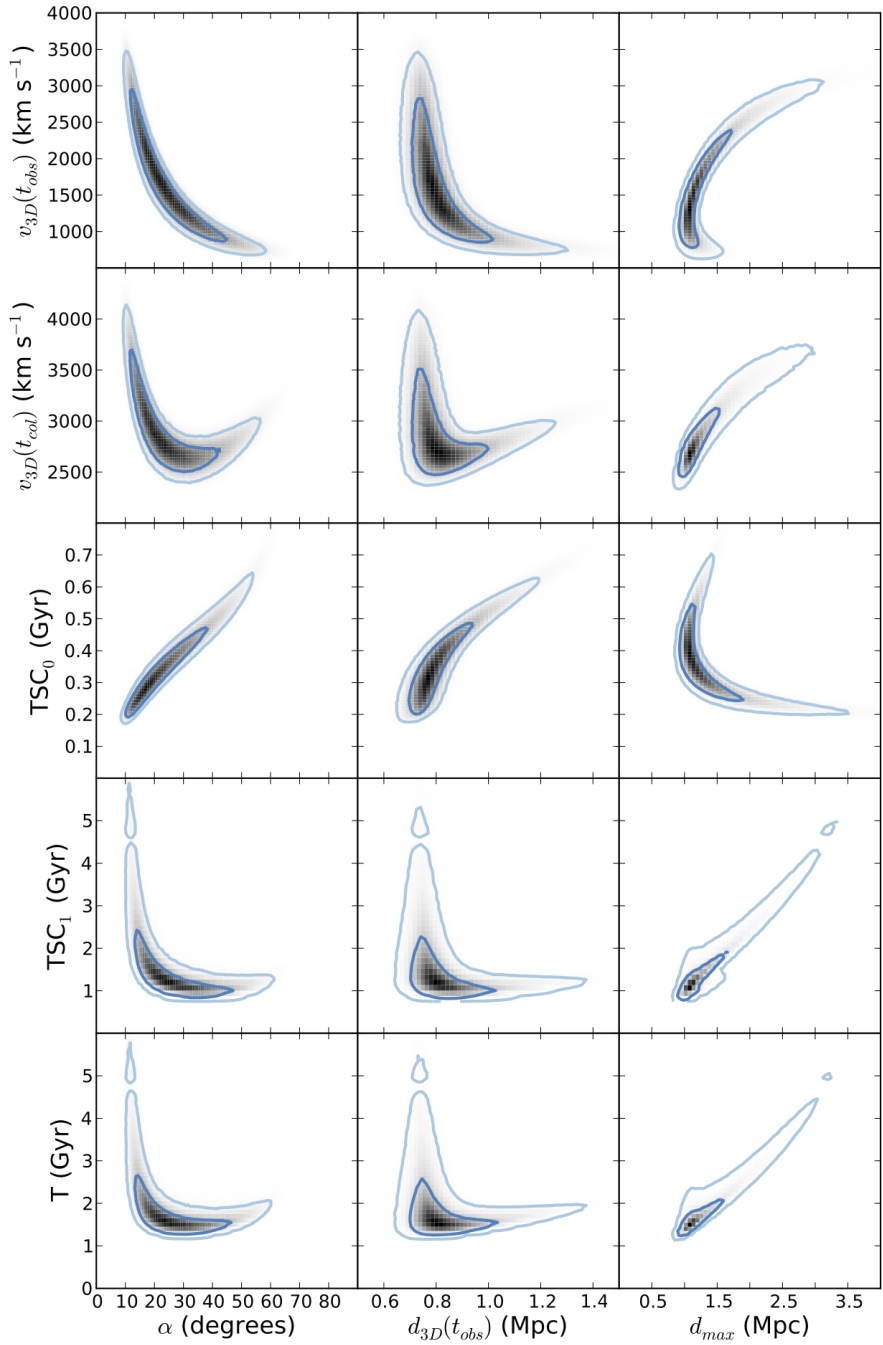


Figure A.6 Bullet Cluster marginalized *Geometry vs. Velocity & Time* parameters result plots, for the case including the added temporal prior of §3.3.2.2. Dark and light blue colors correspond to 68% and 95% confidence intervals, respectively.

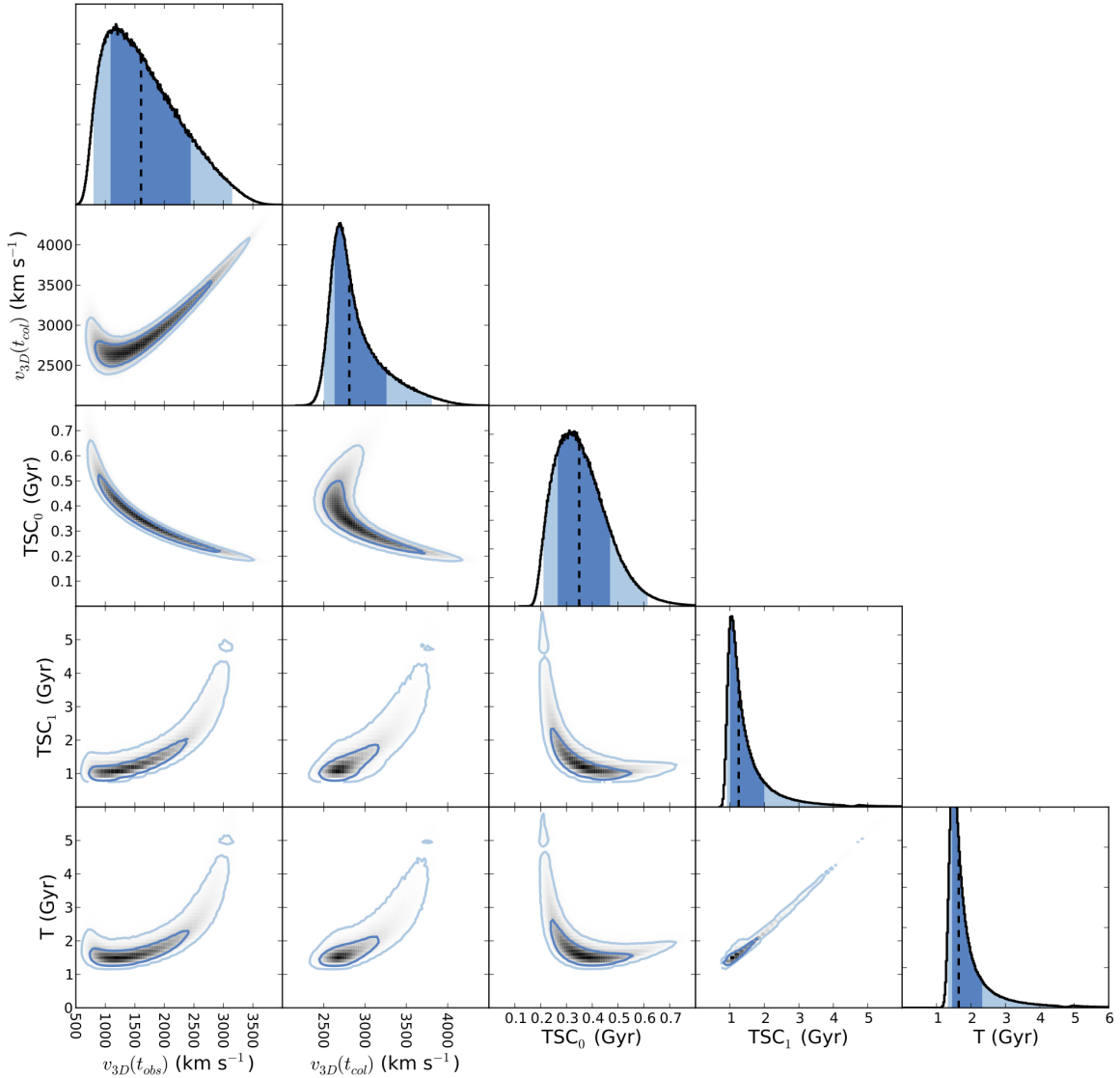


Figure A.7 Bullet Cluster marginalized *Velocity & Time vs. Velocity & Time* parameters result plots, for the case including the added temporal prior of §3.3.2.2. Dark and light blue colors correspond to 68% and 95% confidence intervals, respectively. The black dashed line is the biweight-statistic location (Beers et al., 1982).

## A.4 Musket Ball Cluster Result Plots

This section contains the parameter results array plots for the Musket Ball Cluster. Similar to §A.3 the parameters are grouped in three categories (*Input*, *Geometry*, and *Velocity & Time*) resulting in a six subplot results array, see Figure A.1. The *Input* parameters consist of:  $M_{200_1}$ ,  $M_{200_2}$ ,  $z_1$ ,  $z_2$ , and  $d_{\text{proj}}$ , where halo 1 refers to the “south” subcluster and halo 2 refers to the “north” subcluster. The calculated *Geometry* parameters consist of:  $\alpha$ ,  $d_{\text{3D}}$ , and  $d_{\text{max}}$ . The calculated Velocity & Time parameters consist of:  $v_{\text{3D}}(t_{\text{obs}})$ ,  $v_{\text{3D}}(t_{\text{col}})$ ,  $TSC_0$ ,  $TSC_1$ , and  $T$ .

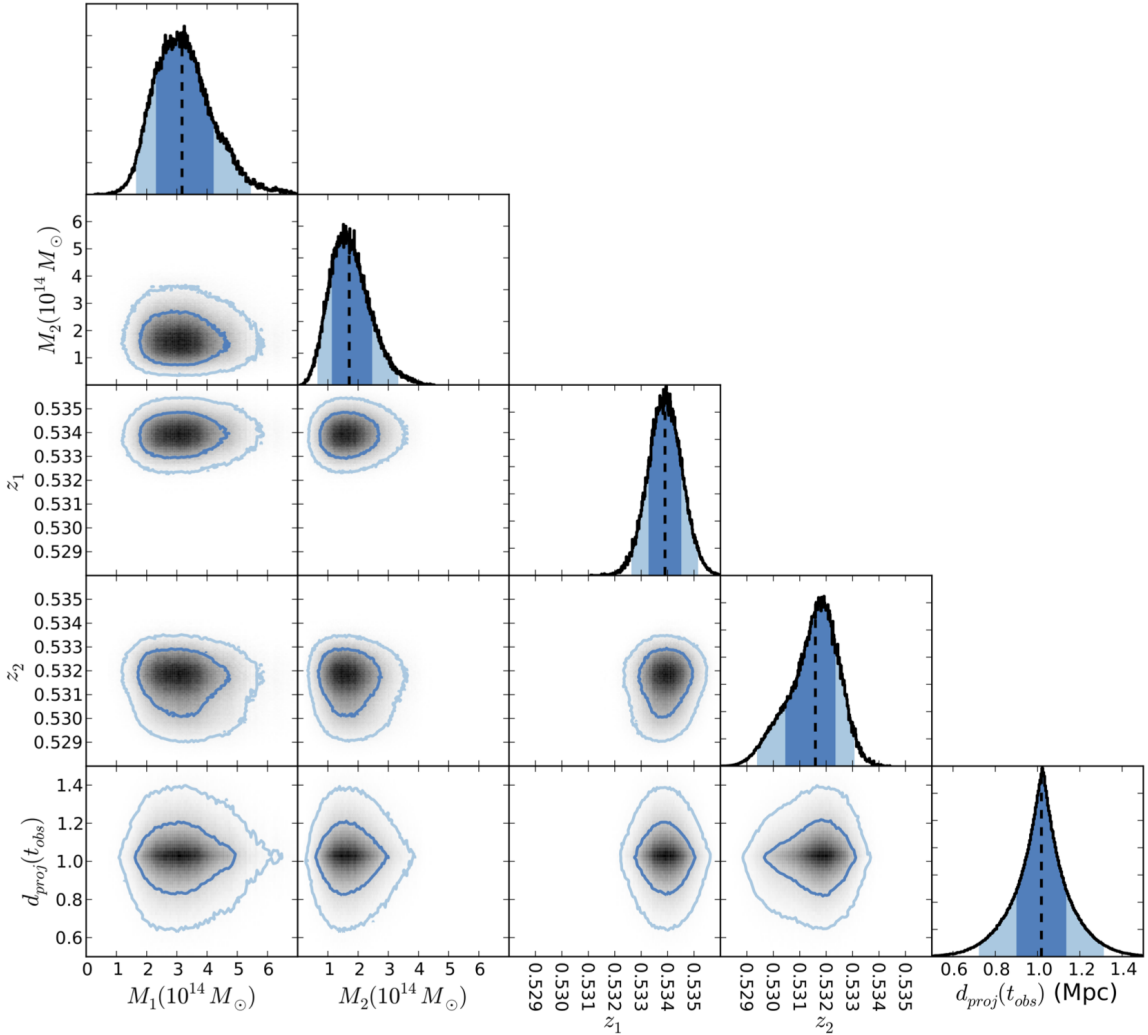


Figure A.8 Musket Ball Cluster marginalized *Input vs. Input* parameters result plots. Dark and light blue colors correspond to 68% and 95% confidence intervals, respectively. The black dashed line is the biweight-statistic location (Beers et al., 1982).

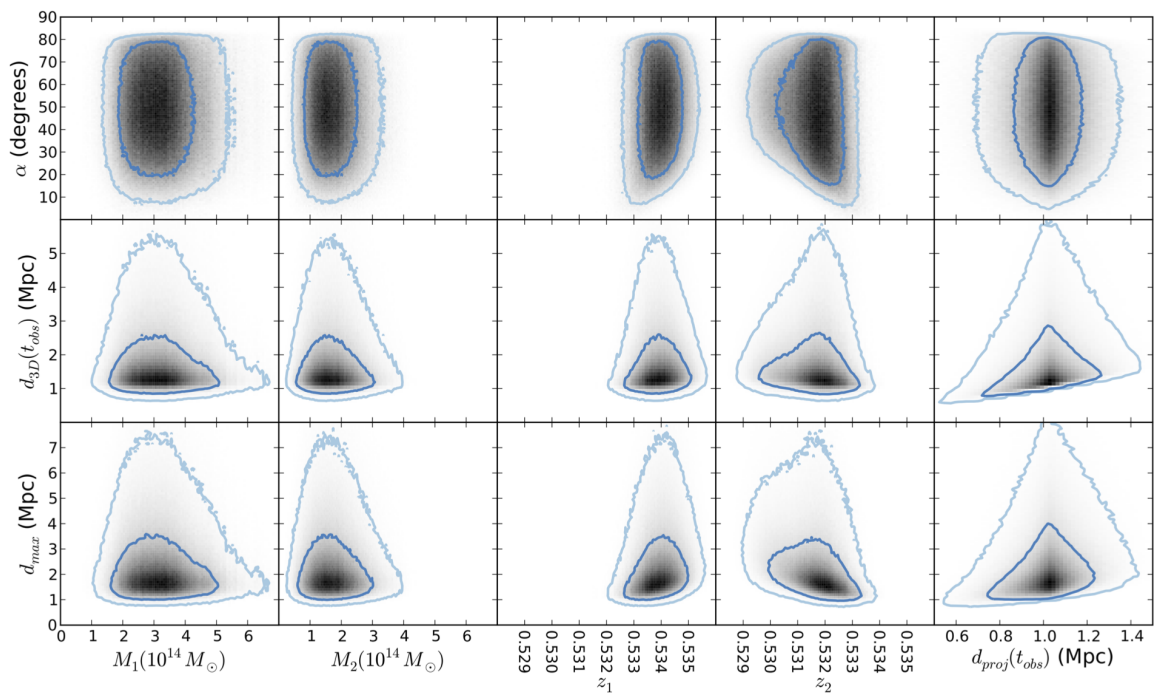


Figure A.9 Musket Ball Cluster marginalized *Input vs. Geometry* parameters result plots. Dark and light blue colors correspond to 68% and 95% confidence intervals, respectively.

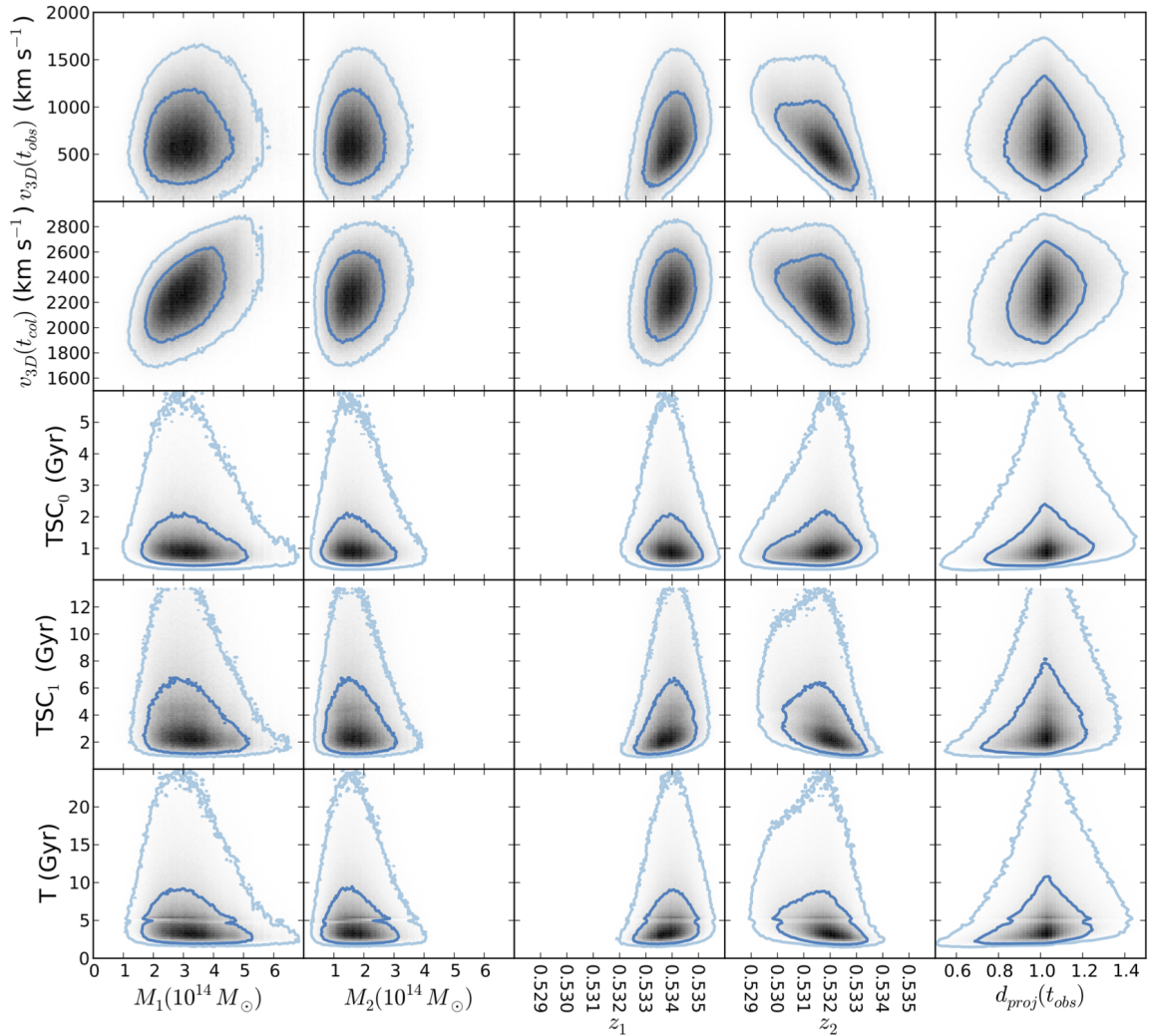


Figure A.10 Musket Ball Cluster marginalized *Input vs. Velocity & Time* parameters result plots. Dark and light blue colors correspond to 68% and 95% confidence intervals, respectively.

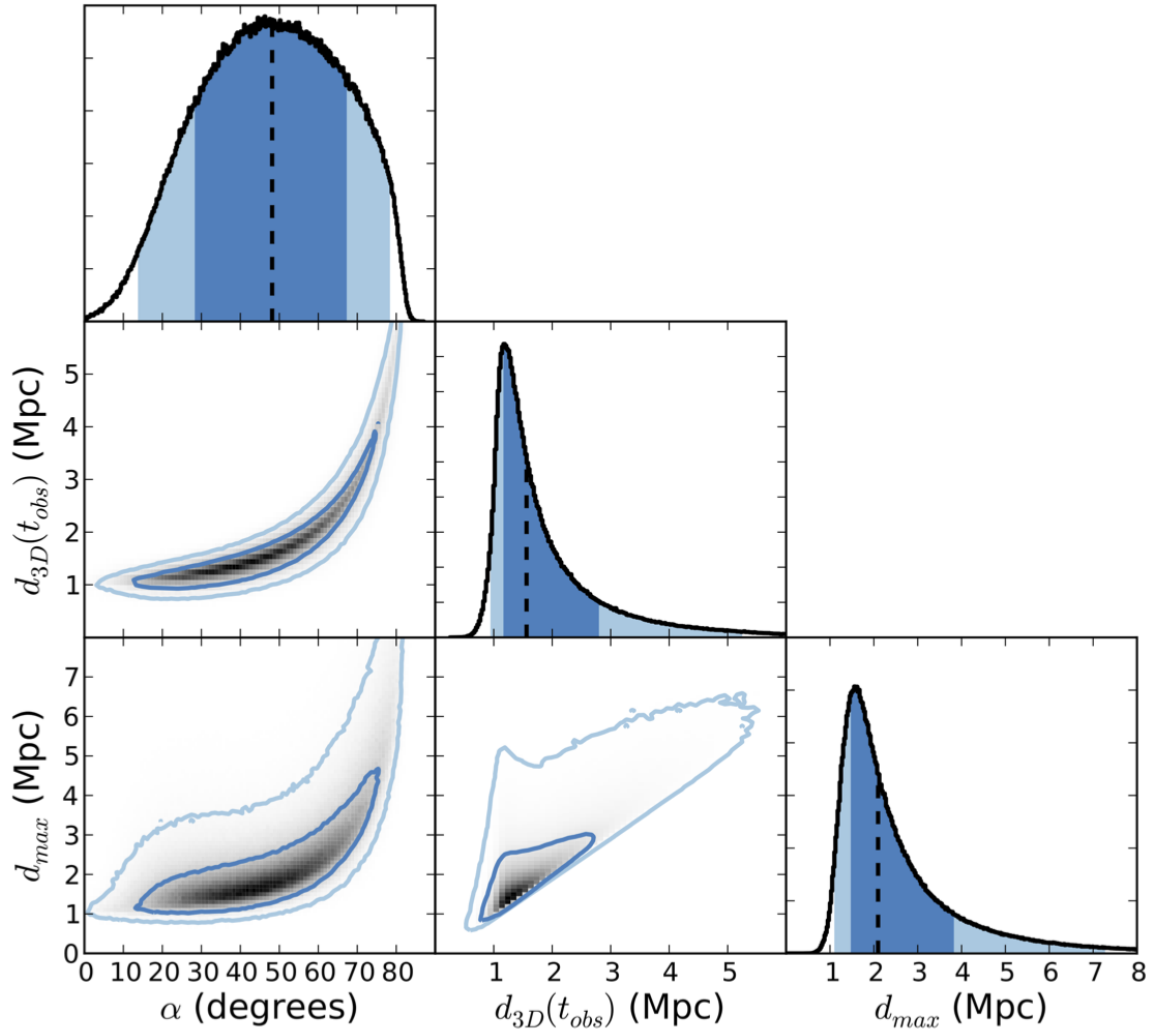


Figure A.11 Musket Ball Cluster marginalized *Geometry vs. Geometry* parameters result plots. Dark and light blue colors correspond to 68% and 95% confidence intervals, respectively. The black dashed line is the biweight-statistic location (Beers et al., 1982).

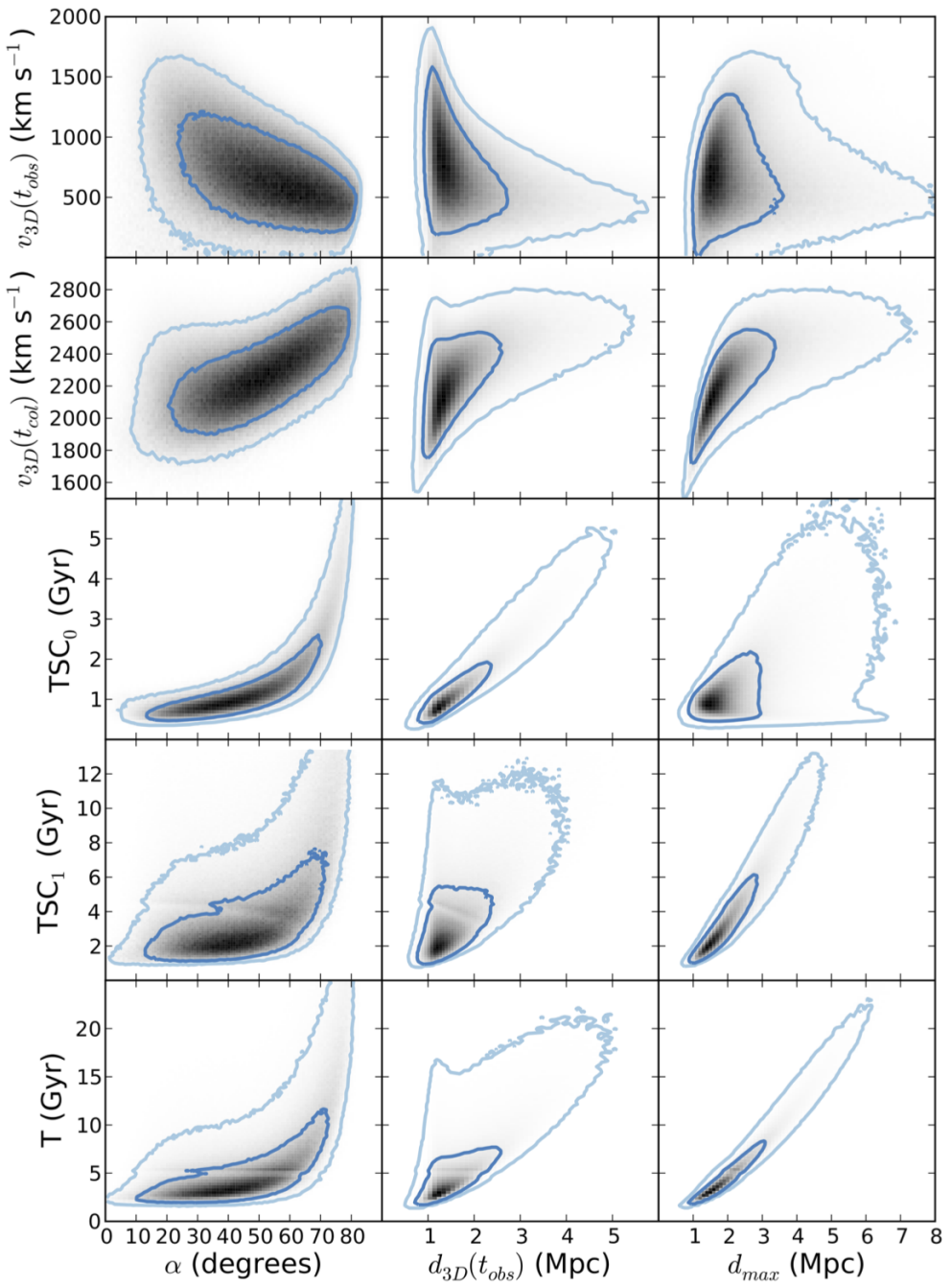


Figure A.12 Musket Ball Cluster marginalized *Geometry vs. Velocity & Time* parameters result plots. Dark and light blue colors correspond to 68% and 95% confidence intervals, respectively.

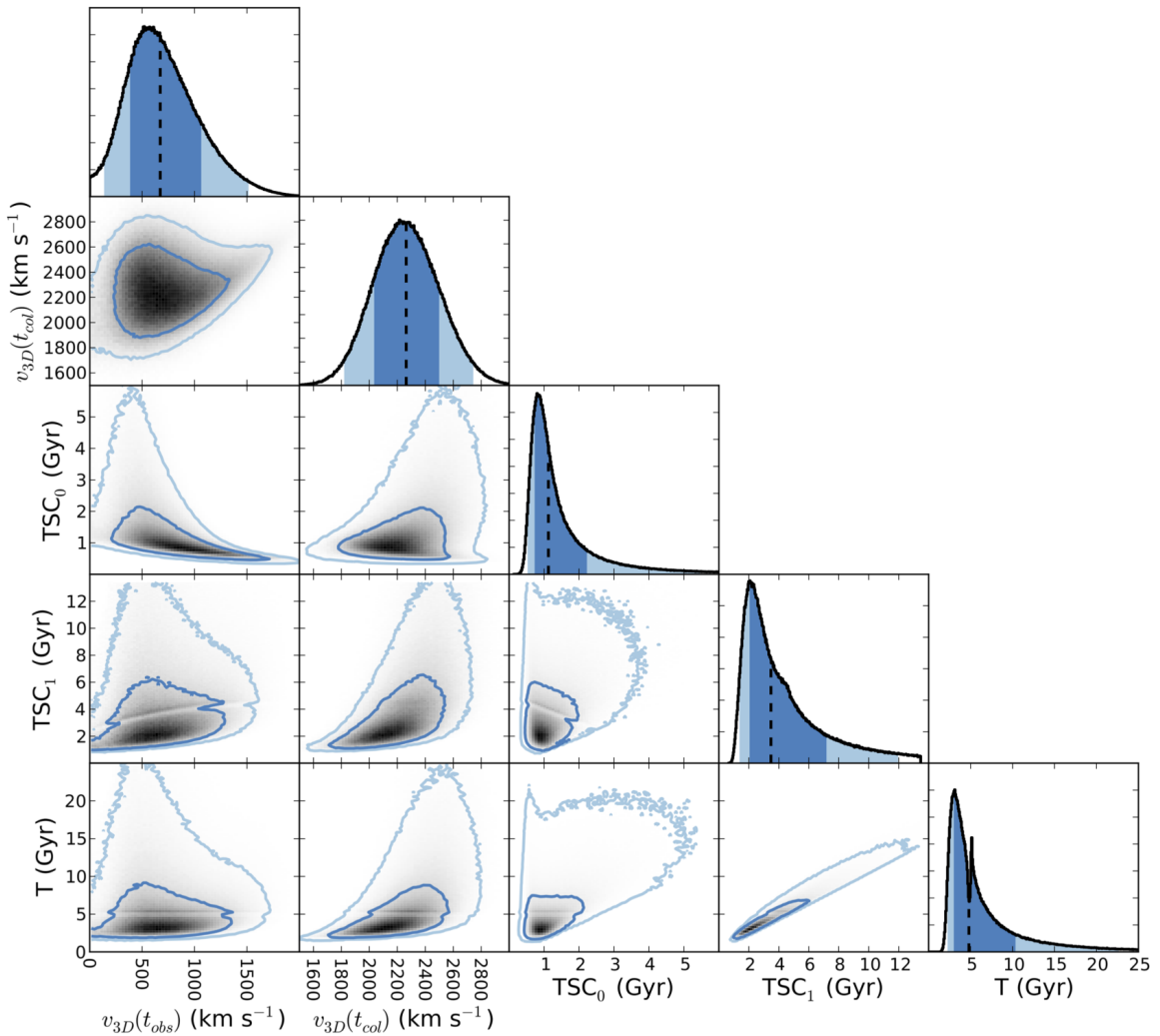


Figure A.13 Musket Ball Cluster marginalized *Velocity & Time vs. Velocity & Time* parameters result plots. Dark and light blue colors correspond to 68% and 95% confidence intervals, respectively. The black dashed line is the biweight-statistic location (Beers et al., 1982).

# References

- Ackerman, L., Buckley, M. R., Carroll, S. M., & Kamionkowski, M. 2009, Phys. Rev. D, 79, 023519
- Angus, G. W., & McGaugh, S. S. 2008, MNRAS, 383, 417
- Arkani-Hamed, N., Finkbeiner, D. P., Slatyer, T. R., & Weiner, N. 2009, Phys. Rev. D, 79, 015014
- Arnaud, K. A. 1996, in Astronomical Society of the Pacific Conference Series, Vol. 101, Astronomical Data Analysis Software and Systems V, ed. G. H. Jacoby & J. Barnes, 17
- Barrena, R., Biviano, A., Ramella, M., Falco, E. E., & Seitz, S. 2002, A&A, 386, 816
- Barrena, R., Girardi, M., Boschin, W., & Dasí, M. 2009, A&A, 503, 357
- Beers, T. C., Flynn, K., & Gebhardt, K. 1990, AJ, 100, 32
- Beers, T. C., Geller, M. J., & Huchra, J. P. 1982, ApJ, 257, 23
- Benítez, N. 2000, ApJ, 536, 571
- Bertin, E. 2006, in Astronomical Society of the Pacific Conference Series, Vol. 351, Astronomical Data Analysis Software and Systems XV, ed. C. Gabriel, C. Arviset, D. Ponz, & S. Enrique, 112

- Bertin, E., Mellier, Y., Radovich, M., Missonnier, G., Didelon, P., & Morin, B. 2002, in Astronomical Society of the Pacific Conference Series, Vol. 281, Astronomical Data Analysis Software and Systems XI, ed. D. A. Bohlender, D. Durand, & T. H. Handley, 228
- Bonafede, A., et al. 2012, MNRAS, 426, 40
- Boschin, W., Girardi, M., Barrena, R., & Nonino, M. 2012, A&A, 540, A43
- Bourdin, H., et al. 2011, A&A, 527, A21
- Boylan-Kolchin, M., Bullock, J. S., & Kaplinghat, M. 2012, MNRAS, 422, 1203
- Bradač, M., Allen, S. W., Treu, T., Ebeling, H., Massey, R., Morris, R. G., von der Linden, A., & Applegate, D. 2008, ApJ, 687, 959
- Bradač, M., et al. 2006, ApJ, 652, 937
- Bullock, J. S. 2010, ArXiv e-prints
- Bullock, J. S., Dekel, A., Kolatt, T. S., Kravtsov, A. V., Klypin, A. A., Porciani, C., & Primack, J. R. 2001, ApJ, 555, 240
- Carlson, E. D., Machacek, M. E., & Hall, L. J. 1992, ApJ, 398, 43
- Chung, S. M., Gonzalez, A. H., Clowe, D., Markevitch, M., & Zaritsky, D. 2010, ApJ, 725, 1536
- Chung, S. M., Gonzalez, A. H., Clowe, D., Zaritsky, D., Markevitch, M., & Jones, C. 2009, ApJ, 691, 963
- Clowe, D., Gonzalez, A., & Markevitch, M. 2004, ApJ, 604, 596
- Coe, D., Benítez, N., Sánchez, S. F., Jee, M., Bouwens, R., & Ford, H. 2006, AJ, 132, 926
- Coil, A. L., et al. 2011, ApJ, 741, 8

- Colín, P., Avila-Reese, V., Valenzuela, O., & Firmani, C. 2002, ApJ, 581, 777
- Courbin, F., & Minniti, D., eds. 2002, Lecture Notes in Physics, Berlin Springer Verlag, Vol. 608, Gravitational Lensing: An Astrophysical Tool
- Dahle, H. 2000, in The NOT in the 2000's, ed. N. Bergvall, L. O. Takalo, & V. Pirola, 45
- Dalcanton, J. J., & Hogan, C. J. 2001, ApJ, 561, 35
- Davé, R., Spergel, D. N., Steinhardt, P. J., & Wandelt, B. D. 2001, ApJ, 547, 574
- Davis, M., et al. 2003, in Society of Photo-Optical Instrumentation Engineers (SPIE) Conference Series, Vol. 4834, Society of Photo-Optical Instrumentation Engineers (SPIE) Conference Series, ed. P. Guhathakurta, 161–172
- Dawson, W. A. 2013, ApJ, 772, 131
- Dawson, W. A., et al. 2012, ApJ, 747, L42
- de Laix, A. A., Scherrer, R. J., & Schaefer, R. K. 1995, ApJ, 452, 495
- Diaferio, A., Schindler, S., & Dolag, K. 2008, Space Sci. Rev., 134, 7
- Dietrich, J. P., Böhnert, A., Lombardi, M., Hilbert, S., & Hartlap, J. 2012, MNRAS, 419, 3547
- Duffy, A. R., Schaye, J., Kay, S. T., & Dalla Vecchia, C. 2008, MNRAS, 390, L64
- Ensslin, T. A., Biermann, P. L., Klein, U., & Kohle, S. 1998, A&A, 332, 395
- Evrard, A. E., et al. 2008, ApJ, 672, 122
- Fahlman, G., Kaiser, N., Squires, G., & Woods, D. 1994, ApJ, 437, 56
- Farrar, G. R., & Rosen, R. A. 2007, Physical Review Letters, 98, 171302
- Feng, J. L., Kaplinghat, M., & Yu, H.-B. 2010, Physical Review Letters, 104, 151301

- Ferrari, C., Benoist, C., Maurogordato, S., Cappi, A., & Slezak, E. 2005, A&A, 430, 19
- Fischer, P., & Tyson, J. A. 1997, AJ, 114, 14
- Gal, R. R., Lemaux, B. C., Lubin, L. M., Kocevski, D., & Squires, G. K. 2008, ApJ, 684, 933
- Geller, M. J., Dell'Antonio, I. P., Kurtz, M. J., Ramella, M., Fabricant, D. G., Caldwell, N., Tyson, J. A., & Wittman, D. 2005, ApJ, 635, L125
- Gelman, A., & Rubin, D. B. 1992, Statistical Science, 7, 457
- Giavalisco, M., et al. 2004, ApJ, 600, L93
- Girardi, M., Barrena, R., Boschin, W., & Ellingson, E. 2008, A&A, 491, 379
- Gnedin, O. Y., & Ostriker, J. P. 2001, ApJ, 561, 61
- Gómez, P. L., Hughes, J. P., & Birkinshaw, M. 2000, ApJ, 540, 726
- Gómez, P. L., et al. 2012, AJ, 144, 79
- Halverson, N. W., et al. 2009, ApJ, 701, 42
- Hennawi, J. F., & Ostriker, J. P. 2002, ApJ, 572, 41
- Hennawi, J. F., & Spergel, D. N. 2005, ApJ, 624, 59
- Hincks, A. D., et al. 2010, ApJS, 191, 423
- Hogan, C. J., & Dalcanton, J. J. 2000, Phys. Rev. D, 62, 063511
- Hwang, H. S., & Lee, M. G. 2009, MNRAS, 397, 2111
- Ilbert, O., et al. 2006, A&A, 457, 841
- Jee, M. J., Blakeslee, J. P., Sirianni, M., Martel, A. R., White, R. L., & Ford, H. C. 2007, PASP, 119, 1403

- Jee, M. J., & Tyson, J. A. 2009, ApJ, 691, 1337
- Kahn, F. D., & Woltjer, L. 1959, ApJ, 130, 705
- Kalberla, P. M. W., Burton, W. B., Hartmann, D., Arnal, E. M., Bajaja, E., Morras, R., & Pöppel, W. G. L. 2005, A&A, 440, 775
- Klypin, A., Kravtsov, A. V., Valenzuela, O., & Prada, F. 1999, ApJ, 522, 82
- Kochanek, C. S., & White, M. 2000, ApJ, 543, 514
- Kuzio de Naray, R., McGaugh, S. S., & de Blok, W. J. G. 2008, ApJ, 676, 920
- Lee, J., & Komatsu, E. 2010, ApJ, 718, 60
- Lemaux, B. C., et al. 2009, ApJ, 700, 20
- Machacek, M. E. 1994, ApJ, 431, 41
- Mahdavi, A., Hoekstra, H., Babul, A., Balam, D. D., & Capak, P. L. 2007, ApJ, 668, 806
- Markevitch, M. 2006, in ESA Special Publication, Vol. 604, The X-ray Universe 2005, ed. A. Wilson, 723
- Markevitch, M., Gonzalez, A. H., Clowe, D., Vikhlinin, A., Forman, W., Jones, C., Murray, S., & Tucker, W. 2004, ApJ, 606, 819
- Markevitch, M., Gonzalez, A. H., David, L., Vikhlinin, A., Murray, S., Forman, W., Jones, C., & Tucker, W. 2002, ApJ, 567, L27
- Mastropietro, C., & Burkert, A. 2008, MNRAS, 389, 967
- Mellier, Y. 1999, ARA&A, 37, 127
- Menanteau, F., et al. 2012, ApJ, 748, 7

- Meneghetti, M., Yoshida, N., Bartelmann, M., Moscardini, L., Springel, V., Tormen, G., & White, S. D. M. 2001, MNRAS, 325, 435
- Merten, J., et al. 2011, MNRAS, 417, 333
- Miller, N. A., & Owen, F. N. 2003, AJ, 125, 2427
- Milosavljević, M., Koda, J., Nagai, D., Nakar, E., & Shapiro, P. R. 2007, ApJ, 661, L131
- Miralda-Escudé, J. 2002, ApJ, 564, 60
- Moore, B., Ghigna, S., Governato, F., Lake, G., Quinn, T., Stadel, J., & Tozzi, P. 1999, ApJ, 524, L19
- Mroczkowski, T., et al. 2012, ArXiv e-prints
- Muchovej, S., et al. 2011, ApJ, 732, 28
- Navarro, J. F., Frenk, C. S., & White, S. D. M. 1996, ApJ, 462, 563
- Newman, A. B., Treu, T., Ellis, R. S., & Sand, D. J. 2013a, ApJ, 765, 25
- Newman, A. B., Treu, T., Ellis, R. S., Sand, D. J., Nipoti, C., Richard, J., & Jullo, E. 2013b, ApJ, 765, 24
- Newman, J. A., et al. 2012, ArXiv e-prints
- Noh, Y., & Cohn, J. D. 2011, MNRAS, 413, 301
- Nusser, A. 2008, MNRAS, 384, 343
- Nuza, S. E., Hoeft, M., van Weeren, R. J., Gottlöber, S., & Yepes, G. 2012, MNRAS, 420, 2006
- Oh, S.-H., Brook, C., Governato, F., Brinks, E., Mayer, L., de Blok, W. J. G., Brooks, A., & Walter, F. 2011, AJ, 142, 24

- Okabe, N., Bourdin, H., Mazzotta, P., & Maurogordato, S. 2011, ApJ, 741, 116
- Ouchi, M., et al. 2004, ApJ, 611, 660
- Owen, F. N., Ledlow, M. J., Keel, W. C., Wang, Q. D., & Morrison, G. E. 2005, AJ, 129, 31
- Peebles, P. J. E. 1993, Principles of Physical Cosmology (Princeton University Press)
- Peter, A. H. G. 2012, ArXiv e-prints
- Peter, A. H. G., Rocha, M., Bullock, J. S., & Kaplinghat, M. 2013, MNRAS, 430, 105
- Planck Collaboration et al. 2013, ArXiv e-prints
- Poggianti, B. M., Bridges, T. J., Komiyama, Y., Yagi, M., Carter, D., Mobasher, B., Okamura, S., & Kashikawa, N. 2004, ApJ, 601, 197
- Poole, G. B., Fardal, M. A., Babul, A., McCarthy, I. G., Quinn, T., & Wadsley, J. 2006, MNRAS, 373, 881
- Pospelov, M., Ritz, A., & Voloshin, M. 2008, Physics Letters B, 662, 53
- Ragozzine, B., Clowe, D., Markevitch, M., Gonzalez, A. H., & Bradač, M. 2012, ApJ, 744, 94
- Randall, S. W., Markevitch, M., Clowe, D., Gonzalez, A. H., & Bradač, M. 2008, ApJ, 679, 1173
- Randall, S. W., Sarazin, C. L., & Ricker, P. M. 2002, ApJ, 577, 579
- Ricker, P. M., & Sarazin, C. L. 2001, ApJ, 561, 621
- Rocha, M., Peter, A. H. G., Bullock, J. S., Kaplinghat, M., Garrison-Kimmel, S., Oñorbe, J., & Moustakas, L. A. 2013, MNRAS, 430, 81
- Rubin, V. C., & Ford, Jr., W. K. 1970, ApJ, 159, 379

Ruhl, J., et al. 2004, in Society of Photo-Optical Instrumentation Engineers (SPIE) Conference Series, Vol. 5498, Society of Photo-Optical Instrumentation Engineers (SPIE) Conference Series, ed. C. M. Bradford, P. A. R. Ade, J. E. Aguirre, J. J. Bock, M. Dragovan, L. Duband, L. Earle, J. Glenn, H. Matsuhara, B. J. Naylor, H. T. Nguyen, M. Yun, & J. Zmuidzinas, 11–29

Russell, H. R., et al. 2011, MNRAS, 417, L1

Sanders, R. H., & McGaugh, S. S. 2002, ARA&A, 40, 263

Schindler, S., & Mueller, E. 1993, A&A, 272, 137

Simon, J. D., Bolatto, A. D., Leroy, A., Blitz, L., & Gates, E. L. 2005, ApJ, 621, 757

Spergel, D. N., & Steinhardt, P. J. 2000, Physical Review Letters, 84, 3760

Springel, V., & Farrar, G. R. 2007, MNRAS, 380, 911

Steigman, G. 2008, JCAP, 10, 1

The Dark Energy Survey Collaboration. 2005, ArXiv Astrophysics e-prints

Tulin, S., Yu, H.-B., & Zurek, K. M. 2012, JCAP, 5, 13

—. 2013, Physical Review Letters, 110, 111301

Tyson, J. A. 2002, in Society of Photo-Optical Instrumentation Engineers (SPIE) Conference Series, Vol. 4836, Society of Photo-Optical Instrumentation Engineers (SPIE) Conference Series, ed. J. A. Tyson & S. Wolff, 10–20

Tyson, J. A., Wenk, R. A., & Valdes, F. 1990, ApJ, 349, L1

van den Bergh, S. 1999, PASP, 111, 657

van Weeren, R. J., Brüggen, M., Röttgering, H. J. A., & Hoeft, M. 2011a, MNRAS, 418, 230

van Weeren, R. J., Hoeft, M., Röttgering, H. J. A., Brüggen, M., Intema, H. T., & van Velzen, S. 2011b, *A&A*, 528, A38

van Weeren, R. J., Röttgering, H. J. A., Brüggen, M., & Hoeft, M. 2010, *Science*, 330, 347

Vikhlinin, A., & Markevitch, M. 2003, in *Astronomical Society of the Pacific Conference Series*, Vol. 301, Matter and Energy in Clusters of Galaxies, ed. S. Bowyer & C.-Y. Hwang, 63

Vikhlinin, A., et al. 2009, *ApJ*, 692, 1033

Vogelsberger, M., & Zavala, J. 2013, *MNRAS*, 430, 1722

Vogelsberger, M., Zavala, J., & Loeb, A. 2012, *MNRAS*, 423, 3740

Wechsler, R. H., Bullock, J. S., Primack, J. R., Kravtsov, A. V., & Dekel, A. 2002, *ApJ*, 568, 52

Willman, B. 2010, *Advances in Astronomy*, 2010

Wittman, D. M., et al. 2002, in *Society of Photo-Optical Instrumentation Engineers (SPIE) Conference Series*, Vol. 4836, *Society of Photo-Optical Instrumentation Engineers (SPIE) Conference Series*, ed. J. A. Tyson & S. Wolff, 73–82

Yagi, M., Kashikawa, N., Sekiguchi, M., Doi, M., Yasuda, N., Shimasaku, K., & Okamura, S. 2002, *AJ*, 123, 66

Yoshida, N., Springel, V., White, S. D. M., & Tormen, G. 2000a, *ApJ*, 535, L103

—. 2000b, *ApJ*, 544, L87

Zavala, J., Vogelsberger, M., & Walker, M. G. 2013, *MNRAS*, 431, L20

Zwicky, F. 1933, *Helvetica Physica Acta*, 6, 110

—. 1937, *ApJ*, 86, 217